THE UNIVERSITY OF CALGARY

Space-Time Processing For Multiple Access Applied to Indoor Environments

by

Jean-François Bousquet

A THESIS

SUBMITTED TO THE FACULTY OF GRADUATE STUDIES

IN PARTIAL FULFILLMENT OF THE REQUIREMENTS FOR THE

DEGREE OF MASTER OF SCIENCE

DEPARTMENT OF ELECTRICAL AND COMPUTER

ENGINEERING

CALGARY, ALBERTA

March, 2007

THE UNIVERSITY OF CALGARY

FACULTY OF GRADUATE STUDIES

The undersigned certify that they have read, and recommend to the Faculty of Graduate Studies for acceptance, a thesis entitled "SPACE-TIME PROCESSING FOR MULTIPLE ACCESS APPLIED TO INDOOR CHANNEL ENVIRONMENTS" submitted by Jean-François Bousquet in partial fulfillment of the requirements for the degree of MASTER OF SCIENCE.

Supervisor, Dr. Sebastian Magierowski,
Department of Electrical and Computer Engineering.

Dr. Arief Budiman,
Department of Mechanical & Manufacturing Engineering.

Dr. Michel Fattouche,
Department of Electrical and Computer Engineering.

Dr. Geoffrey Messier,
Department of Electrical and Computer Engineering.

15/3/07

Date

Abstract

This thesis presents the design and verification of the physical layer for a practical 128-Mbps, 20-MHz, indoor wireless network intended to simultaneously communicate with 32 users over a 5.6-GHz carrier.

The system is implemented using a bi-directional space-time filter distributed among the access point (AP) and user terminals (UT). This design allows the AP to significantly correct for a variety of channel quality variations thus preventing the BER from exceeding 10^{-3}.

An extensive set of experimental wireless channel measurements emulating a multi-user network while using a compact, custom-designed circular array are compared with current spatial channel models and the results are applied to the space-time algorithm showing a doubling in spectral efficiency.

Finally, intending the system to be implemented in a 0.18-μm CMOS technology, the digital requirements of key functional communication blocks is considered. This analysis shows that the UT decorrelator can be implemented with only a 2-mW power consumption.

Acknowledgements

I wish to express my gratitude to important individuals who helped me accomplish my thesis successfully.

Firstly, I wish to thank my supervisor Dr. Sebastian Magierowski for encouraging me in the development of innovative ideas and in the elaboration of concepts using a creative approach. The numerous discussions we have had in his office have guided me in defining a complete and thorough understanding of the system built in this project and his work ethic is a model of meticulousness for me to follow.

I also want to acknowledge the collaboration I have had with Dr. Geoffrey Messier who provided support in the definition of the communication systems and initiated the analysis on the benefit of antenna arrays in the 801.11b standard. He served as a very useful reference particularly in the comparison of channel models with real channel measurements. Also, Dr. Messier and Dr. Bob Davies, at TrLabs, supplied the equipment allowing spatial channel measurements.

Finally Dr. Joshua L. Leon has been a mentor since my very first year of undergraduate and, after I had been working as a professional for three years, encouraged me to further pursue my graduate studies. Without him and his family I would not have returned as a student and might not have discovered the beauties of Alberta.

To my love, Stéphanie.

Table of Contents

List of Tables

List of Figures

Chapter 1

Introduction

Today's demand for wireless devices is changing. A better understanding of the broadband wireless channel physical properties is helping push the limitations of the current technology. A need for more densely populated networks is the reason for research in more efficient multiple access communications. In this project special attention is focused toward the development of a space division multiple access scheme for an indoor wireless channel suffering from multipath interference. Currently the combination of multiple-input multiple-output (MIMO), which consists of multiple antenna arrays at both the transmitter and receiver, with orthogonal frequency division multiplexing (OFDM) is being marketing as a solution to increase the effective data rate for real time applications. Code division multiple access (CDMA) is known as an effective multiple access scheme but requires the spreading of the data over a greater bandwidth. Hardware limitations as well as the cost of spectrum constrain the CDMA within a limited bandwidth and in effect limit the amount of users sharing the frequency allocation. Here, space division multiple access (SDMA) is being proposed as a secondary multiple access scheme combined with CDMA technology. The possibility of integration of the functionality of the complete wireless transceiver physical layer on a single chip is being evaluated and results tend to show that a chipset with small dimensions seems to be a reasonable goal to implement an access point (AP) communicating in a 32-user network sharing a single channel allocation of 20 MHz. The transceiver's responsibility is to communicate using a 2-slot time division duplex (TDD) to receive in a first instance from up to 32 users, and to transmit in a second instance to the same users dedicated information. The antenna branches are spatially coded to further separate the users with different CDMA codes.

The major contributions brought forward by this project include the development of a physical layer architecture, particularly for the forward link where the combination of a spatial precoder at the access point and a novel low-power multipath decorrelator allow a constant data rate of 4 Mbps for each user. A maximum throughput of 128 Mbps is obtained for all users in the single frequency allocation during the forward link. The development of the digital hardware is validated on 0.18-μm using Cadence simulators, and a description of the necessary hardware requirements show the feasibility of implementing the system on chip with a high level of confidence: the next step in the design of the digital chip consists in extracting the layout for the access point precoder digital electronics as well as for the user terminal receiver. In addition, the performance of the system connected to a circularly sectorized antenna array is validated using real channel measurements. The data extracted from the channel measurements show low spatial correlation results and are used to validate the use of space division multiple access in typical WLAN configurations. It is shown that the multiple access performance can be doubled using four antennas. An even greater performance increase is expected with the use of an antenna array equipped with a greater amount of elements at the access point. Finally the user terminal hardware is shown to perform well for extreme channel variations.

In Chapter 2 we shall present the necessary hardware components in the development of a wireless transceiver. We present current state-of-the-art hardware components as well as their system level architecture for integration on chip. Particularly, a system level description for the digital processor, as well as the data converters and analog hardware electronics are detailed. A description of the digital design at different levels of the design flow is detailed, including the gate level characteristics using 0.18-μm CMOS, as well as the multiply and accumulate important properties and finally the description of different algorithms to be implemented in the development of the transceiver. Much attention is paid in the development of the digital processor architecture because CMOS technology is very promising in integrating low-power digital hardware. Therefore to optimize the benefit of silicon in the development of wireless transceivers the proportion of digital electronics should supplant its analog counterpart which is now being limited to the radio-frequency front-ends connecting the antenna to the baseband processor. Nonetheless the requirements for the analog component can be determined from the necessary communication performance and a good analog design allows greater flexibility in the design of the transceiver system. In particular we show that to obtain an equal relationship between the received signal and transmit signal during the forward link and and reverse link, not only must the gain in each branch of the AP transmitter be made equal to its receiver branch counterpart, also does each user terminal. Finally a 4-element circular sectorized antenna array is designed and its proper behaviour is validated using simple impedance matching theory.

In Chapter 3 the spatial channel represents a limiting component in the development of a high speed multiple access wireless system and its key properties are analyzed. Over the 20-MHz bandwidth of interest the channel can no longer be represented as noise limited, and channel multipath generates inter symbol interference (ISI). Additionally, for an indoor application the channel is slowly time varying and may be subject to fading, which is a source of detection error at the receiver. The dispersive properties, as well as the fading and spatial correlation between individual channels as modeled with the current statistical methodology are studied and compared to the characteristics representing the results of channel measurements taken in University of Calgary laboraties for LOS and NLOS situations.

In Chapter 4 the evaluation of different space-time algorithms for optimal detection at the receiver are analyzed. A bi-directional TDD scheme re-uses the same frequency allocation for both the reverse and forward link. Therefore, assuming the fading is slowly varying relative to the TDD period, the channel characterisitics found at the access point (AP) during the reverse link can be reused on the forward link. Obviously the study is pursued with goal to minimize the hardware complexity at the user terminal (UT), while keeping in mind that the access point (AP) chipset is still to be implemented using a minimum amount of discrete components. Particular attention is put on the development of a forward link precoding SDMA strategy to maximimize the multiple access performance in fading channels, and we show that whether the constraint is placed on the UT receiver or AP transmitter, different algorithms are possible. We show that the optimum solution using a constant transmit power is to reuse the minimum mean square error (MMSE) spatial codes found during the reverse link. Additionnally we present the benefit of CDMA for multiuser channels particularly for low-spread systems. Finally we present the issues in implementing a complete SDMA/CDMA transceiver in order to benefit from the space-time fading conditions.

Finally in Chapter 5 an evaluation of the feasibility of a space-time algorithm applied to a physical layer is elaborated. In order to offer practicality to the system, a rudimentary medium access control (MAC) protocol is described to allow resources for synchronization and to provide an algorithm allowing users to enter the network. The DSP hardware requirements are analyzed for both the AP and UT physical layer and the communication performance of the sub-optimal method retained are shown for different fading conditions. With 12 antennas and 8 codes, it is possible to communicate with up to 32 users depending on channel dispersive conditions and although the hardware at the AP is relatively complex due to the multiple users to be accounted for, the user terminal receiver remains a simple CDMA receiver, adaptable to the dispersive properties of the channel: for low dispersive conditions, a conventional RAKE receiver is applied and for higher channel dispersion a decorrelator architecture developed to minimize hardware complexity represents an elegant solution. In this Chapter the benefit of adding multiple antennas at the 802.11b AP is also analyzed, and the system is applied to different measured channel conditions, to bring a greater level of confidence to the results obtained with statistical channel models. Because the limitation of the front-end circuitry restrained us to a 4-element antenna array, the results show that SDMA can provide a doubling in multiple access performance. We can easily assume that a greater amount of antennas at the access point will increase the multiple access performance to a greater extent.

Chapter 2

Physical Layer Architecture For Transceiver Design

The deployment of a fully functional physical layer requires the implementation of many hardware components whose specifications are defined to fulfill the communication requirements. In this Chapter we describe the electronics necessary to build the multiple antenna equipped access point shown in Figure 2.1 as well as user terminals for eventual integration on chip. We describe in Section 2.1 the digital electronics, followed by a discussion on data converters (ADC and DAC) in Section 2.2, the analog electronics for the front-end in Section 2.3 and the antenna array in Section 2.4. Because CMOS technology represents an accessible and cheap solution the hardware architecture shown in this Chapter is directed toward implementation using this technology.

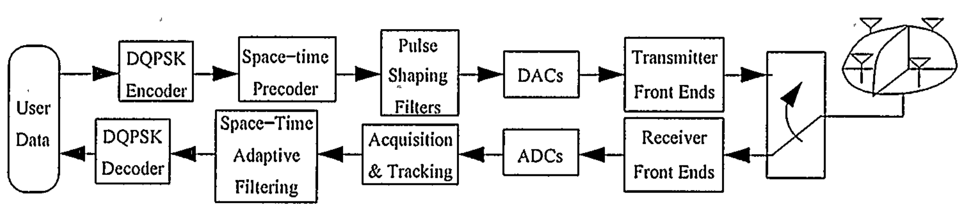

Figure 2.1: Bi-Directional Space-Time Access Point Block Diagram.

2.1 Digital Processing using 0.18-μm CMOS Technology

Complementary metal oxide semiconductor (CMOS) technology is the de-facto physical platform in the design of application specific integrated chips (ASICs). It has been shown to meet high speed requirements at a very low cost and with a relatively low power consumption particularly as transistor dimensions are reduced. In this Section we present the different levels of abstraction in the development of a digital chip. The described methodology can be related to the steps defined in a typical digital design flow. In Section 2.1.1 we present the gate level hardware characteristics and show the possibilities offered by CMOS technology in very large scale integration (VLSI). In Section 2.1.2 we explain the general structure of a central intelligence component in a digital system, i.e. the multiply and accumulate unit (MAC). A Booth multiplier is also developed in VHDL and its characteristics are evaluated on 0.18-μm CMOS for different specified numbers of operand bits. Finally in Section 2.1.3 we show the digital architecture for important communication algorithms particularly for multiple user detection, pulse shaping and synchronization.

2.1.1 Gate Level Hardware Characterization

Whether implementing a system on field programmable gate array (FPGA), digital signal processor (DSP) or application specific integrated chip (ASIC), the hardware designer is confronted with the limitations of the technology. The advantage of using an ASIC in comparison to DSP can be identified mainly as the freedom of the designer to define the low level architecture particularly the MAC architecture. Additionally, although FPGAs offer an attractive prototyping solution, ASICs provide a greater transistor density when compared to FPGAs. In this section we present the gate level hardware characteristics when integrating the application on chip. The examples are developed using 0.18-μm CMOS technology and the methodology may be translated to other technologies.

CMOS transistors are shown in Figure 2.2. They consist of three pins: the gate, drain and source. As explained in classical references on MOS technology such as [1], the voltage between the gate and source V_{GS} in combination with a drain source

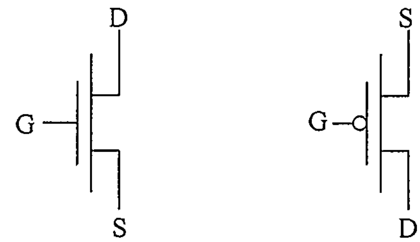

(a) nMOS (b) pMOS

Figure 2.2: CMOS symbols.

voltage V_{DS} induces current to flow through the channel between the drain and source. More specifically, to allow current to flow through the nMOS transistor channel, the voltage V_{GS} must be greater than the threshold voltage V_T, where V_T is positive. Comparatively, for the pMOS transistor, the threshold voltage V_T is negative and current flows when the voltage V_{GS} is smaller (more negative) than V_T. Applied to logic design, when active, nMOS and pMOS devices generally operate in the triode region (for which the nMOS must satisfy $V_{DS} < V_{GS} - V_T$, while the pMOS must satisfy $V_{DS} > V_{GS} - V_T$) and behave like a voltage controlled resistor. Therefore the transistor applied in digital electronics can be considered as a switch: when $V_{GS} < V_T$ no current flows between drain and source and when $V_{GS} > V_T$ the channel is modeled as an equivalent resistance between the source and the drain.

The dynamic behavior of the MOSFET is mostly limited by the capacitive gate input impedance C_g, which for a device with $V_{GS} > V_T$, a channel of length L and width W, is expressed as:

$$C_g = C_{ox} W L, \tag{2.1}$$

where C_{ox} is the capacitance per unit area and, assuming t_{ox} is the oxide thickness and ϵ_{ox} is its permittivity, $C_{ox} = \epsilon_{ox}/t_{ox}$.

To give an insight on the characteristics influencing digital design performance an

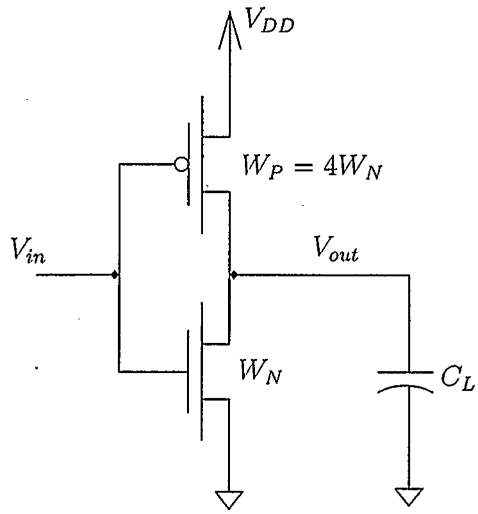

Figure 2.3: Static Inverter Circuit Diagram.

inverter circuit is modeled and its behavior is analyzed. Although multiple structures have been described in digital logic design, in this project only static CMOS design (explained in [2]) is approached. Simply put, static CMOS design is an asynchronous circuit, i.e. the circuit is not controlled with a clock input. Complementary pull-up and pull-down networks consist respectively of pMOS transistors connected to V_{DD} and nMOS transistors connected to ground. For example the static inverter circuit is shown in Figure 2.3 where the output impedance is a capacitor representing the input impedance belonging to the next logic stage. For the inverter, if $V_{in} = 0$ V, the pull-down network is open while current flows through the pMOS transistor. In contrast when $V_{in} = V_{DD}$ V the pull-up network is open while current flows through the nMOS transistor. Note that the transition is not discrete in nature and the V_{out}/V_{in} transfer function is shown in Figure 2.4 where care must be taken to a) maximize the slope at the transition to minimize uncertainty and b) insure the transition occurs at mid-range. Note that to satisfy the second condition the ratio between the nMOS channel width W_N and the pMOS channel width W_P is approximately 4, in effect generating an on-resistance of approximately equal value for the two devices.

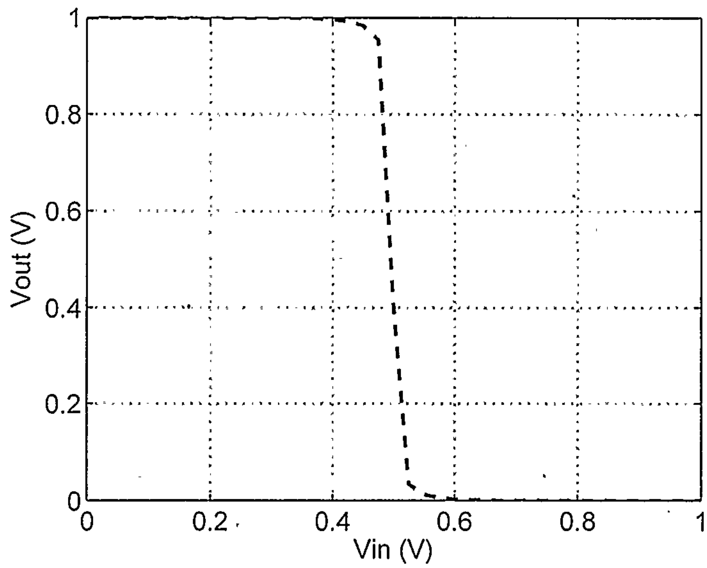

Figure 2.4: Inverter Transfer Function For $C_L = 5$ fF, $W_N = 0.5$ μm

In a second instance we analyze the transient behavior of the inverter with a capacitive load. As mentioned above the equivalent output impedance Z_{out} of the inverter is resistive: when the input voltage is V_{in} is high, the pMOS transistor is off, and the output resistance represents the relationship between voltage and current in the nMOS transistor channel, and similarly when V_{in} is low, the nMOS transistor is off and the output impedance represents the relationship between voltage and current in the pMOS transistor. Because the output impedance is resistive, i.e. $Z_{out} = R_{out}$, the transient response is that of a low-pass filter: the steady-state is attained when the exponentially decaying current in the load capacitance becomes negligible, that is at a delay equal to 5τ, where τ is the time constant defined as $\tau = R_{out}C_L$. This undesired behavior shown in Figure 2.5 for different capacitive loads skews the signal and it is important to design the digital circuits to minimize the time constant. At each transition there is also a spike and as explained in [2] this is due to the capacitor

C_{GD} present between the gate and drain of each transistor.

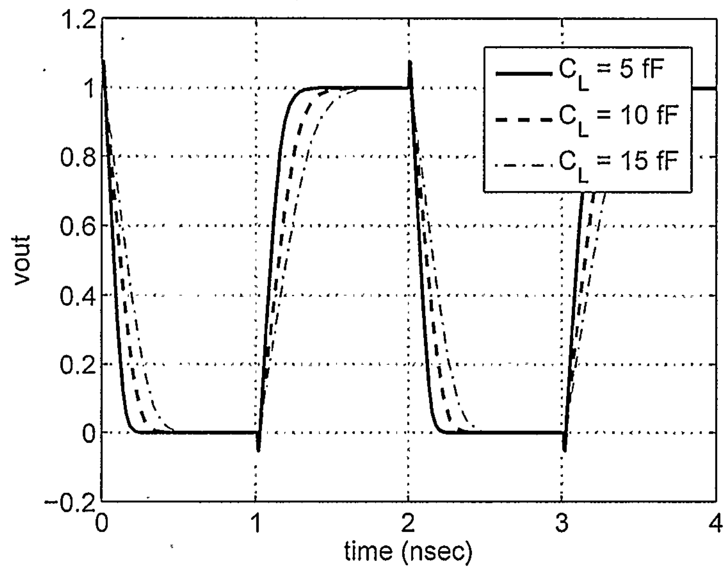

Figure 2.5: Inverter Transient Behaviour For $W_N = 250\ \mu$m

Concerning the power consumption associated with digital electronics, CMOS transistors pose an attractive solution because in steady-state operation the power consumption is almost negligible due to the fact that the nMOS and pMOS transistors are never on simultaneously. However the charging of the capacitors at every signal transition requires power. The proportionality relationship between different variables and the dynamic power consumption of a digital circuit is described in [3] as:

$$P \propto C_L V_{DD}^2 f, \tag{2.2}$$

where C_L is the load capacitance at the output of the circuit, V_{DD} is the supply voltage and f is the average switching frequency of the hardware component. Note that the load capacitance C_L is proportional to the channel length L as stated in Equation (2.1). For example scaling the CMOS technology for a given circuit from 0.35 μm to 0.18 μm and scaling the power supply from $V_{DD} = 1.8$ V to $V_{DD} = 1.0$

V scales the power consumption by a factor of 6.3. It must also be mentioned that reducing the channel length also reduces the area necessary to implement the digital circuits.

2.1.2 Multiply And Accumulate Unit

In this Section we present the minimal MAC functionalities to be implemented in a typical ASIC applied to wireless communications. We present a minimal complexity number representation as well as the digital electronics resources necessary for minimum MAC implementation. Because the multiplier is shown in [3] to require a great amount of resources compared to the adder, we focus our attention on the multiplication operation.

We assume a fixed-point 2's complement representation of numbers, rather than a floating point representation. This is a popular method for DSP design because of its relatively simple arithmetic.

In 2's complement representation, an N-bit word represents integers from -2^{N-1} to $2^{N-1}-1$. The most significant bit (MSB) indicates the sign of the number represented: when it is zero, the number is positive, else the number is negative. Also to convert a positive binary number to its negative counterpart, one must simply invert all bits and add one.

The format of the fixed-point binary value is completely characterized with the word length WL and the position of the binary point as shown in Figure 2.6. In the example shown the equivalent decimal value is:

$$\begin{aligned} val_{dec} = -1 \cdot b_{WL-1} \times 2^{WL-3} + b_{WL-2} \times 2^{WL-4} + \cdots \\ b_2 \times 2^0 + b_1 \times 2^{-1} + b_0 \times 2^{-2}, \end{aligned} \tag{2.3}$$

for which the smallest quantization step representable is 2^{-2}.

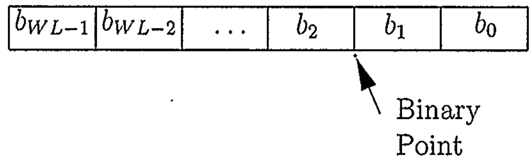

Figure 2.6: Fixed-Point Binary Representation.

The addition of numbers in 2's complement representation follows the same rules as for decimal numbers. The subtraction of two values such as $x - y$ can be accomplished using $x + (-y)$. For example the subtraction of 5.75 with 2.25 using a 6-bit word and for which the fraction consists of two bits is $0101.11_2 - 0010.01_2$:

$$\begin{array}{r} 0101.11_2\ (5.75) \\ \underline{+1101.11_2}\ (-2.25) \\ 0011.10_2\ (3.5). \end{array}$$

Note that the maximum value of the result can be represented on $N + 1$ bits else overflow may occur. Unlike for unsigned representation, using 2's complement notation, the carry out of the most significant bit (MSB) cannot be used to detect overflow. Rather, overflow is detected when both operands are positive and the result is negative or alternatively when both operands are negative and the result is positive. Two operands of opposite signs cannot cause overflow.

Multiplication in 2's complement notation is similar to the multiplication operation in decimal notation. The result of the multiplication of two operands with word length WL_1 and WL_2 respectively must be represented with $WL_1 + WL_2$ bits. The multiplication is carried out by summing all partial products. The partial products must be represented with $WL_1 + WL_2$ bits, and as such, are sign extended to assure that the left side of the partial products are aligned. For example, consider the multiplication of 10.11_2 (-1.25) with 011_2 (3):

$$\begin{array}{r} 10.11_2\ (-1.25) \\ \underline{\times\ 011_2}\ (3) \\ 1110.11 \\ 1101.10 \\ \underline{+\ 0000.00} \\ 11100.01\ (-3.75). \end{array}$$

In this project, a N-bit multiplier is coded in VHDL using the Booth algorithm. As explained in [4] the Booth multiplier component is itself composed of two components: 1) the 'datapath', a component that receives the multiplier and multiplicand and processes the intermediate results, and 2) the 'control unit', itself responsible for managing the multiplication operation and sending control commands to the 'datapath'. The VHDL code for an 8-bit multiplier was simulated using Cadence's NCSim program and was tested using the multiplicand $D = 83$ and the multiplier $Q = 101$. As can be seen in Figure 2.7, the st command from the control unit initiates the multiplication with the values present in registers dd and qq and at each clock (clk) cycle a partial product is obtained in signed-digit form and stored in the aq register. After 8 clock cycles (the number of clock periods necessary is equal to the number of quantization bits) the final result $Q = 8383$ is obtained in the aq register and the flag rdy indicates that the value is available. Note that the adder uses a ripple carry architecture described in [5] to compute partial products.

Furthermore the Booth multiplier simulated in NCSim is evaluated using the TSMC Artisan library of digital components (described in [6]) with Synopsys' Design

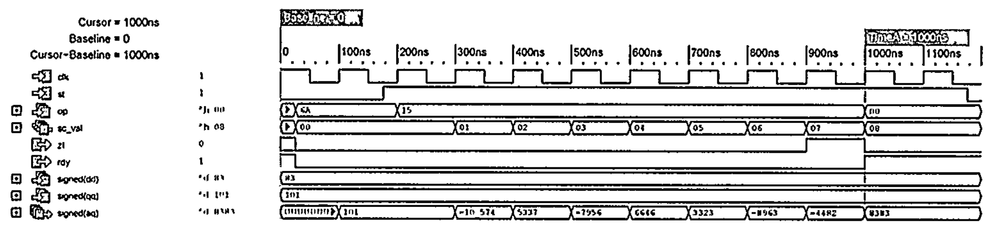

Figure 2.7: Multiplier Behavioural Simulation.

Analyzer. Using this program, the gate level VHDL representation of the multiplier is obtained, and the hardware requirements using 0.18-μm CMOS technology can be estimated. Note that the library characterization is limited to a supply voltage equal to $V_{dd} = 1.8$ V. Also in Design Analyzer, the clock period was defined at $T_{clk} = 50$ nsec and the load capacitance at each pin is $C_L = 5$ fF, which is of the order of MOS gate capacitance. The multiplier requirements are evaluated for different bit counts, and are compiled in Table 2.1. It can be observed that as the bit count increases, the power consumption, area and path delay all increase due to the increase in hardware complexity. Also the total time required to compute the product is $N \times 50$ *nsec*. These results may be compared to results obtained in [3], where empirical equations are used to model the power consumption and area of a two-stage pipelined multiplier in 0.25-μm CMOS technology. For a N-bit multiplier with supply voltage V_{dd} the area A is calculated with

$$A\ (\mathrm{mm}^2) = 0.0044 + 0.0019N + 0.00017N^2, \tag{2.4}$$

while the energy E is:

$$E\ (\mu\mathrm{W/MHz}) = (1.68 + 0.15N + 0.019N^2)V_{dd}^2. \tag{2.5}$$

Therefore, a 12-bit input two-stage pipelined multiplier operating at 600 nsec requires a power consumption equal to 33.6 μW and an area of 0.051 mm^2. This seems to indicate that the Booth multiplier with ripple carry adders designed here is optimized for area but tends to require more power consumption than the design measured in Zhang's work ([3]).

Table 2.1: Multiplier Requirements For Different Bit Count.

Bit Count	Power Consumption (μW)	Area (μm^2)	Path Delay nsec
6	132.5	3512.7	5.14
8	169.2	4437.4	6.53
10	208.1	5498.5	7.98
12	243.9	6429.9	9.43

2.1.3 Wireless Algorithms Digital Integration

In this Section we define the digital architecture of standard wireless block components necessary for detection, synchronization and pulse shaping. The objective is to describe standard components of a digital wireless system intended for integration on chip. In this aspect the MAC unit explained in the previous Section is the foundation for this higher level of abstraction. In a typical design flow, following the definition of the system requirements, comes the hardware description using VHDL (or Verilog) code. Also a preliminary evaluation of the system on FPGA can validate the functionality. The final step involves applying it to the specific semiconductor for ASIC manufacturing and validation of requirements' satisfaction.

The blocks evaluated in this section have different levels of complexity and we start by explaining the requirements for differential phase modulation, particularly for differential quadrature phase shift keying (DQPSK). It is followed with a description of a generic acquisition block allowing a coarse synchronization at the receiver. Adaptive filtering and direct matrix inversion (DMI) are alternative solutions for the evaluation of spatial filter optimal weights which will be detailed in Chapter 4 and both their architectures will be explained here. Finally we will demonstrate the digital hardware implications of implementing a pulse shaping filter.

Differential Phase Modulation

In digital communication systems, phase shift keying (PSK) applies a defined phase to the carrier depending on the input symbol and in contrast to amplitude modulation (AM) it maintains a constant envelop. Binary phase shift keying defines two phases, one for each input symbol. The input symbol is either a zero or a one. In contrast QPSK defines four phases, associated with each input symbol, each symbol being a combination of two input bits. The advantage of QPSK compared to BPSK is that it increases the bandwidth efficiency: for example, a 4-Mbps binary input stream encoded with a QPSK strategy transmits each symbol at 2 Mbaud while the symbol rate for the BPSK encoder remains at 4 Mbaud. Also, to reduce the receiver complexity, differential phase shift keying is an attractive solution. The concept of differential encoding is that the phase of the carrier is changed relative to the previous carrier phase depending on the symbol input. An example of the relationship between the input bit value for the WLAN 802.11b DQPSK scheme is shown in Table 2.2.

Table 2.2: DQPSK Encoder Input-Output Relationship.

Binary value	Phase change
00	0
01	$\pi/2$
11	π
10	$3\pi/2$

The DQPSK encoder block architecture is shown in Figure 2.8 while the DQPSK decoder is represented in Figure 2.9. As can be seen, the implementation of the DQPSK encoder and decoder requires the knowledge of the current and previous symbols to define the current phase output. The QPSK mapper converts the input

2-bit symbol to a phase such as given in Table 2.2. The output of the QPSK encoder consists of two elements: the in-phase and quadrature components are multiplied by $\cos(2\pi f_c t)$ and $-\sin(2\pi f_c t)$ respectively as explained in [7]. The advantage of DQPSK compared to QPSK is that the phase of the locally generated carrier frequency does not have to be aligned with the phase of the received signal and the signal is demodulated non-coherently.

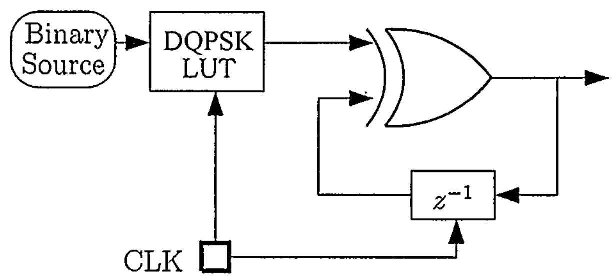

Figure 2.8: DQPSK Encoder Digital Implementation.

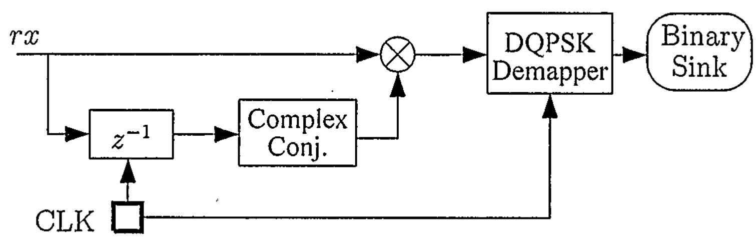

Figure 2.9: DQPSK Decoder Digital Implementation.

Synchronization

In general symbol synchronization is implemented at the receiver baseband in two steps: an initial coarse delay estimation (termed acquisition) synchronizes the received signal to within half a symbol period and the second step, the tracking phase obtains a much better accuracy. The acquisition phase may be accomplished with a sliding window correlator implementation and is the subject of work in [8] while an early-late gate synchronizer described in [9] can further track the received signal with relatively low complexity. In this project we show the implications of acquisition for a coarse delay estimation of the signal while the tracking component is the subject of a further study.

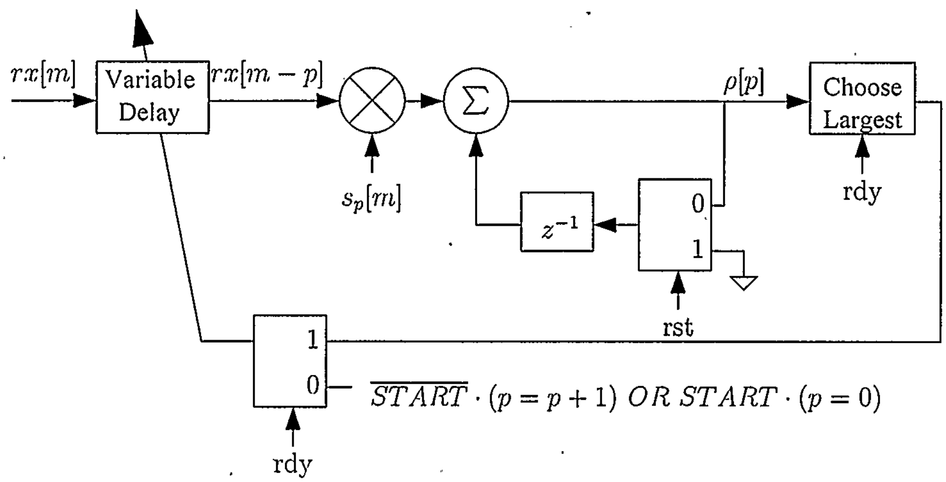

Figure 2.10: Sliding Window Correlator Architecture.

A sliding window correlator (SWC) architecture for implementation using digital hardware is shown in Figure 2.10. Note that an N-symbol periodic reference signal s_p must be transmitted in the data and is also locally generated at the receiver. The objective of the SWC is to synchronize the received signal with the locally generated reference s_p. The basic building block is the correlator which multiplies the complex received signal delayed by p with the locally generated reference at time m and sums the result for all time n from 0 to N. At the start of the acquisition phase the control signal START is set in order to reset the delay p. After each correlation the counter adjusting the delay p must be incremented. Once the acquisition period is completed, the maximum correlation value (assuming it is above a defined threshold) represents the synchronization time, and the delay p of the variable delay block must be adjusted accordingly.

As explained in [8], assuming the symbol period is T_s a single correlation requires NT_s seconds to be completed, and must be repeated for all possible delay arrivals. To complete a sliding window correlation with all possible symbol delays precise to half the chip rate requires $2N \cdot (NT_s)$, where the factor of 2 accounts for the fact the a correlation must be done for each half chip period. In order to decrease the lock time, multiple (K) correlators delayed by an additional symbol index can be implemented in parallel and at the end of the correlation time the delay p must be incremented by the parallel correlator count, i.e. $p = p + K$. This is at the expense of a greater power consumption but may still represent an attractive solution to reduce lock time. For example using $K = 4$ parallel correlators will decrease the maximum lock time by four.

An alternative solution to implement a complete correlation is to memorize the received data sequence and find the biggest peak by integrating with delayed versions of a reference signal such as what has been done in [10].

Adaptive Filtering

Using a receiver with M antennas, the M-tap received signal represents multiple versions of the desired signal accompanied with different noise and interference contributions at each tap. To increase the link reliability a weight can be applied at each tap to minimize the mean square error (MMSE) between the estimate and the expected value. The weight vector $\mathrm{w} \in C^{M\times 1}$ theoretical solution will be shown in Chapter 4. An interesting alternative to the theoretical solution (alleviating the need for matrix inversion) is the adaptive approach. A very simple adaptive method is the least mean square (LMS) algorithm represented in Figure 2.11.

As explained in [11] to effectively obtain optimal weights a reference signal (synchronized with the received signal) is compared at time n with the output of the combiner $\hat{d}_k[n] = \mathrm{w}^H[n]\mathrm{y}[n]$. An error between the reference signal $x_k[n]$ and the

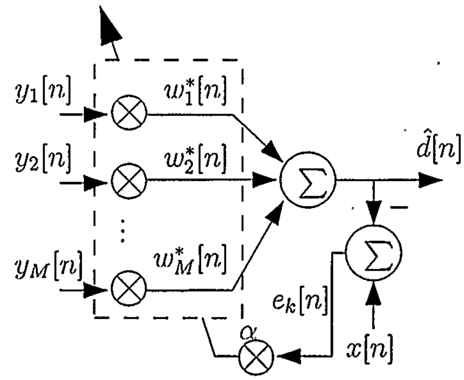

Figure 2.11: LMS Algorithm.

output of the combiner $\hat{d}_k[n]$ is obtained and is weighted with the step-size α to be subtracted from the current weight estimates $\mathrm{w}[n]$ thus obtaining a new weight estimate $\mathrm{w}[n+1]$. The equivalent algorithm is expressed mathematically with:

$$\begin{aligned} \hat{d}_k[n] &= \mathrm{w}^H[n]\mathrm{y}[n]; \\ e_k[n] &= x_k[n] - \hat{d}_k[n]; \\ \mathrm{w}[n+1] &= \mathrm{w}[n] + \alpha e_k^*[n]\mathrm{y}[n]. \end{aligned} \tag{2.6}$$

The step-size α controls the convergence rate and an optimal value must be chosen to insure convergence, while minimizing the final error. As explained in [11] the optimal step-size α_{opt} for energy considerations is actually time varying and is defined with:

$$\alpha_{opt} = \min_{1 \leq n \leq N} \frac{1}{\|\mathrm{y}[n]\|^2}. \tag{2.7}$$

This shows the importance of obtaining an estimate of the received signal vector power $\|\mathrm{y}\|^2$ to calculate the desired step-size and maintain its value below the received signal power for all iterations.

Direct Matrix Inversion

In a multi-tap scenario (for example using an antenna array with M elements) the minimization of the mean square error between the expected value and the output of the received signal can be optimized by applying a weight at each branch. As will be shown in Chapter 4 the optimal weight vector $\mathrm{w} \in C^{M\times 1}$ can be found using the Wiener-Hopf equation expressed as $\mathrm{w} = \mathbf{R}^{-1}\mathbf{p}$, where $\mathbf{R} \in C^{M\times M}$ represents the covariance matrix between each tap and $\mathbf{p} \in C^{M\times 1}$ is the cross-correlation vector between the desired transmit signal and the received signal at each tap.

Direct matrix inversion may be a possible solution to evaluate $\mathbf{R}^{-1}$. As explained in [12] the Gauss elimination is an efficient numerical method to invert a matrix. It consists of reducing the augmented system of linear equations to a triangular form: the left square matrix becomes an upper triangular matrix while the right square matrix (initially an identity matrix) represents the inverse.

Pulse shaping

Discrete data bandwidth occupancy is infinite and applying it to the band-limited analog hardware creates intersymbol interference (ISI). To avoid ISI, the data bandwidth must be limited prior to analog conversion and as explained in [7] Nyquist demonstrated that the necessary condition to avoid ISI is to design a filter with the following impulse response characteristics:

$$h_{eff}(nT_s) = \begin{cases} K, & n = 0 \\ 0, & n \neq 0 \end{cases} \tag{2.8}$$

where T_s is the symbol period, n is an integer and K is a non-zero constant. In other words, the pulse shaping filter's impulse response is zero at integer multiples of the symbol period. The sinc filter defined with:

$$h_{eff}(t) = \frac{\sin(\pi t/T_s)}{\pi t/T_s}. \tag{2.9}$$

satisfies this requirement, but possesses a steep slope around the zero-crossings, causing greater errors when the receiver is not perfectly synchronized. Additionally, it is a non-causal infinite impulse response (IIR) filter which must be truncated. By definition non-causality requires the knowledge of advanced samples of the signal to compute the current output. Note that the Fourier transform of the sinc function is a brick wall filter with a baseband bandwidth of $1/(2T_s)$. Nyquist also proved that a brick wall filter convolved with any arbitrary function also achieves the condition stipulated in Equation (2.8). The raised cosine filter (RCF) is one possible solution satisfying the Nyquist criterion and in the time domain is represented with:

$$h_{RCF}(t) = \frac{\sin(\pi t/T_s)}{\pi t}\frac{\cos(\pi\alpha t/T_s)}{1-(4\alpha t/2T_s)^2}, \tag{2.10}$$

Note that the function contains discontinuities at $t = 0$ and $t = \pm\frac{2T_s}{4\alpha}$ and at these points the tap coefficient must be approximated at the limit. In the frequency domain it occupies a bandwidth of:

$$B = \frac{(1+\alpha)}{2T_s} \tag{2.11}$$

In practical applications the RCF is typically truncated between $[-6T_s, 6T_s]$ to preserve causality. Also its implementation may be separated using identical filters $\sqrt{H_{RF}(f)}$ at the transmitter and receiver. In a frequency flat channel this partition realizes matched filtering while in a multipath channel the equivalent total impulse response between RCF input and channel output is a convolution of the RCF and the dispersive channel; in ([13]) it is shown that in this case the discrete impulse response at time n is the result of a contribution of multiple channel paths convolved with the pulse shaping filter and because the continuous time paths may be added destructively, fading may occur.

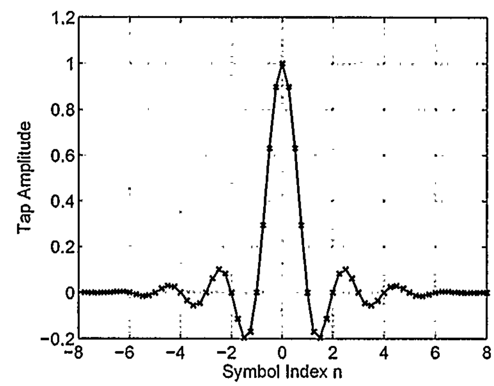

Figure 2.12: Raised Cosine Filter Tap Amplitude For $\alpha = 0.2$.

2.2 Data Converters

Data converters are necessary components in digital communications systems to convert, in a first instance, the digital (pulse shaped) signal to an analog continuous time signal (function accomplished by a digital to analog converter, or DAC) , and in a second instance, the analog signal to a digital signal (accomplished with an analog to digital converter, or ADC).

Different architectures exist for both the DAC and ADC and the objective in the present section is to describe the hardware requirements to maintain the communication performance.

The conversion between analog to digital quantizes the continuous time signal and as explained in [14] this quantization results in a loss of information. For example, an analog-to-digital (ADC) converter representing the input signal whose range is r with a fixed point precision using B bits, results in a quantization step size of :

$$\Delta = \frac{r}{2^B - 1}, \tag{2.12}$$

and the maximum quantization error e_q is limited to:

$$-\frac{\Delta}{2} \leq e_q \leq \frac{\Delta}{2}. \tag{2.13}$$

Following the method in [15], and assuming that the circuitry is matched to 50 Ohms, the one-bit quantization noise is defined as:

$$N_q = 10 \cdot \log \left[\left(\frac{e_q}{50} \right)^2 \right]. \tag{2.14}$$

Note that N_q represents the maximum quantization error. The quantization error power is limited between $-\infty$ and N_q. Although its distribution is unknown, it serves as a comparison with thermal noise as well as noise added by analog circuitry in the system to determine the limiting source of noise.

Additionally as the oversampling ratio OSR relative to the data period increases the noise power is spread across a greater bandwidth. In [16], assuming the signal input occupies the full range of the analog-to-digital converter, the signal to noise ratio (SNR) defined at its output is:

$$SNR\ (\text{dB}) \approx 6.02 \cdot N + 3 \cdot \log_2(OSR) + 1.76, \tag{2.15}$$

indicating that SNR improves by approximately 6 dB for every bit added, and an additional 3-dB SNR improvement can be obtained by increasing the oversampling factor by two. Also in [17] the author evaluates current state-of-the-art ADCs and describes the figure of merit as specified by different manufacturers. It can be seen from the graphs presented by Walden that at 100 Msps, which is in the range of our design sampling frequency, the mean stated resolution is approximately 9 bits. For example, if we assume $N = 6$ bits and an $OSR = 4$ samples/symbol, the output

SNR is 43.9 dB indicating that the quantization noise is negligible. Obviously this is conditional on the fact that the desired signal occupies the full range of the ADC which in general cannot be assumed particularly in multiple user scenarios. Nonetheless, it is possible to adjust the full scale to account for interferer presence as well as imperfect automatic gain control (AGC) and obtain a more realistic approximation of the SNR due to quantization.

Concerning the digital-to-analog converter (DAC), the sample-and-hold operation can be interpreted as a convolution of the sampled data with a square pulse of width $1/T_{sampl}$, T_{sampl} being the sample time (the zero-order hold approximation). Nyquist demonstrated that the minimum sampling period needed to recover a signal band-dlimited at f_c is $T_{samp,min} = 1/2f_c$. Also, the Fourier transform of the square pulse is a sinc function with periodic zeros at frequency $f_z = 1/NT_{sampl}$, where N is an integer. Multiplying a digital band-limited signal in the frequency domain with the sinc function results in image frequencies centered around $f_{im} = (N + 0.5)/T_{samp}$ and these image frequencies can be removed using a low pass image-rejection filter at the output of the DAC. As explained in [14] a greater sampling frequency pushes the image frequencies further away resulting in less strict requirements on the low-pass anti-aliasing filter.

2.3 The Analog Hardware

In the development of a wireless communication system the RF front-ends are typically implemented using analog electronics. On the transmitter side the output of the DAC is up-converted at RF with a mixer and amplified before application at the antenna. In contrast on the receiving end the output of the antenna is applied to a low noise amplifier (LNA) and down-converted with a mixer. In a superheterodyne architecture the down-conversion is separated in two steps: initially the resulting signal is down-converted at an intermediate frequency (IF) and filtered prior to a second down-conversion to baseband. This method reduces the DC offset at the cost of an increased complexity compared to the direct-conversion architecture. Digitizing the signal prior to frequency translation to baseband removes the need for baseband analog hardware, but such an architecture requires very fast data converters, and such high speed devices represent a design challenge in low-power CMOS technology to this date.

In Section 2.3.1 the noise contribution attributed to the analog front-ends is explained. We shall compare in Section 2.3.2 integrated chip front-end implementations for WLAN applications and evaluate their performance. Here the focus is particularly on amplification as well as noise enhancement in order to evaluate the equivalent noise sources present at the digital baseband receiver. Finally, I will also demonstrate in Section 2.3.3 the necessary front-end conditions for reciprocity. In comparison with work already done in [18] where an equal signal-to-interference ratio (SIR) is assumed sufficient to demonstrate reciprocity, I assume reciprocity between the forward link and reverse link by maintaining an equal signal to interference and noise ratio (SINR) at the output of the combiner.

2.3.1 Analog Hardware Noise Figure

Electronic components in the RF chain add noise. For example, using a Δf bandwidth limited measuring device at temperature T_0 (in Kelvin), the available noise power from a resistor is:

$$P_n = kT_0\Delta f. \tag{2.16}$$

It is this, and a number of other physical mechanisms (e.g. shot-noise, flicker noise, etc.) that combine to produce a net noise contribution from the electronics processing the radio signal. The noise figure (NF) represents the noise gain due to analog hardware. Naturally its minimum value is NF = 0 dB. In [19], the effect of cascaded circuits on noise figure is evaluated and the author explains how the first hardware stages (designed to minimize NF, constrained on signal amplification) of the receiver are critical in reducing the noise at the output of the cascaded circuitry. Thus the importance of implementing a low noise amplifier (LNA) at radio-frequency (RF) as the first stage of a receiver. A typical LNA noise figure ranges between 0.8 dB and 3 dB, and the overall NF for different integrated receiver implementations is shown in Table 2.3.

2.3.2 Integrated Chip Receiver Front-Ends

In Table 2.3 we show the receiver specifications for different front-end architectures integrated on chip. Because all chips have different characteristics their performances differ as is outlined in the simple description that follows:

- Samavati & al. : a 5-GHz RF receiver, including a synthesizer;
- Liu & Westerwick: a 5-GHz transceiver with a single RF front-end, and VCO;
- Vassiliou & al: a 5-GHz transceiver with a single receiver front-end with baseband amplification and filtering, and synthesizer;
- Behzad & al.: a 5-GHz transceiver with a single receiver front-end with baseband amplification and filtering, and synthesizer;
- Zargari & al.: a dual-band transceiver, superheterodyne receiver, includes baseband amplification and filtering, and synthesizer;
- Perraud & al.: a dual-band transceiver with a direct-conversion receiver, includes baseband amplification and synthesizer;

- Palaskas & al.: an Alamouti transceiver, with synthesizer and DSP;
- Rahn & al.: a 2x2 MIMO transceiver, superheterodyne receiver with baseband amplification, and synthesizer.

Table 2.3: Specifications For Different Front-End Receiver IC Architectures.

Author	Max. Gain (dB)	Noise Figure (dB)	Chip Size (mm^2)	Power Consumption (mW)	Technology
Samavati & al. [20]	12	5.2	1	12.4	CMOS 0.24 μm
Liu, Westerwick [21]	8.7	3	4	114	CMOS 0.25 μm
Vassiliou & al. [22]	79	5.2	18.5	248	CMOS 0.18 μm
Behzad & al. [23]	93	4.0	11.7	150	CMOS 0.18 μm
Zargari & al. [24]	90	5.5	23	320	CMOS 0.25 μm
Perraud & al. [25]	60	4.5	12	230	CMOS 0.18 μm
Palaskas & al. [26]	-	7.5	< 18	280	CMOS 0.09 μm
Rahn & al. [27]	72	7.4	29.1	536	SiGe 0.5 μm

The chips implemented in Table 2.3 represent current state-of-the-art transceiver front-end designs on integrated chip and their specifications can provide a reference in further hardware implementation, particularly for analog applications.

2.3.3 Effect of Unequal Front-End Gain On Reciprocity

In this Section we explain the consequences of unequal front-end specifications and the requirements needed to allow bi-directional communication with weights found in the reverse link. In this study we assume that the front-end hardware unconditionally operates in its linear mode of operation and that therefore its transfer function can be modeled as a linear operation. As shown in Figure 2.13, the gain of the m_{th} front-end on the access point transmit and receive chain is respectively expressed with the complex gain vector $\mathbf{G}_{TX,AP-m}$ and $\mathbf{G}_{RX,AP-m}$, while the gain of the v_{th} user terminal front-end transmitter and receiver are complex scalars respectively denoted by $G_{TX,UT-v}$ and $G_{RX,UT-v}$.

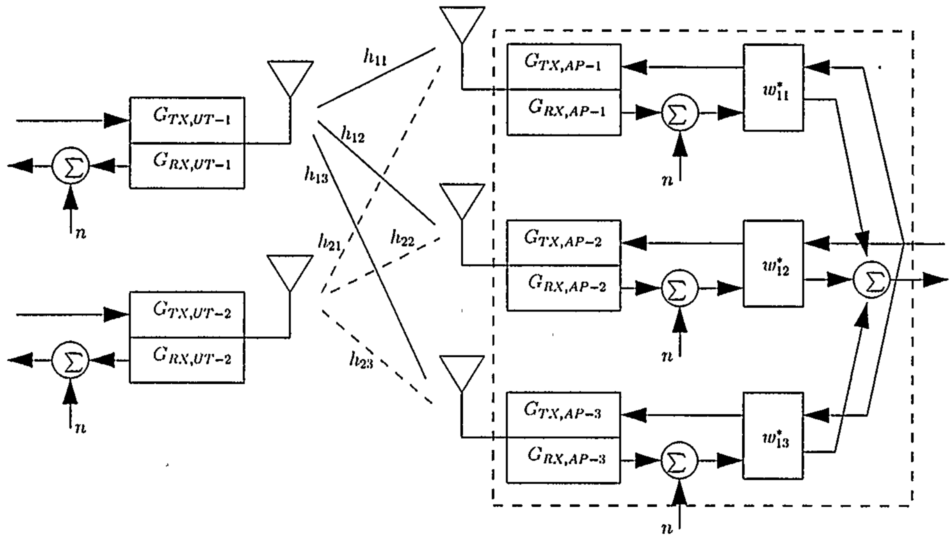

Figure 2.13: Front-End Effect For Bi-Directional Communication.

Following Ung's approach in [18], if we assume the weights are calculated to minimize the error between the transmitted and combined sequence for user v applied to a wireless channel array that is characterized with a complex amplitude $\mathbf{h}_v \in C^{M\times 1}$, in the presence of interference, two conditions must be satisfied concerning the transfer function between the transmitter and receiver. The first condition is:

$$\mathrm{A}_{des} = \mathrm{w}_v^H \mathbf{h}_v = 1, \tag{2.17}$$

while the second condition for the reverse link is:

$$\mathrm{A}_{und,v} = \mathrm{w}_v^H \mathbf{h}_u = 0, \quad 1 \leq u \leq U, u \neq v. \tag{2.18}$$

This second condition states that the contribution of each interferer at the output of the combiner is zero and this is valid only in the condition where the weights are used to remove interference without considering noise power. This is called the zero-forcing solution. In comparison, using the minimum mean square (MMSE) weight solution in the reverse link (in presence of a noise vector $\mathbf{n} \in C^{M\times 1}$ at the input of the combiner) the transfer function representing the noise and interference contribution at the output of the combiner in the reverse link is:

$$\mathbf{A}_{und,v} = \underset{\mathbf{w}_v}{\arg\min} \left| \mathbf{w}_v^H \sum_{u=1,u\neq v}^{U} \cdot \mathbf{h}_u + \mathbf{w}_v^H \mathbf{n} \right|. \tag{2.19}$$

and is minimized at the output of the combiner. For the MMSE algorithm it must be used as the second condition in the reverse link in place of Equation (2.18).

In the forward link the effect of the signal intended to user v at the input of the user u processor as well as noise must be minimized such that:

$$\mathbf{A}_{und} = \underset{\mathbf{w}_v}{\arg\min} \left| \mathbf{h}_u^T \frac{\mathbf{w}_v^*}{\|\mathbf{w}_v\|^2} + n \right|; \tag{2.20}$$

where $\|\mathbf{w}_v\|^2$ is a normalization factor applied at the access point transmitter to force a constant transmit power.

At this point the effect of the front-end is absent in the transfer function between the transmitter and receiver. We now evaluate the transfer function between the mobile units when the front-ends are included in the model first for the zero forcing solution and secondly for the MMSE solution. To demonstrate the hardware requirements needed to maintain reciprocity a system is defined with two user terminals transmitting the data streams x_1 and x_2 respectively in the reverse link to an access point equipped with three antennas as shown in Figure 2.13. The equivalent transfer function must respect:

$$(\text{Cond. } 1 \;-\; \text{Reverse}) \quad G_{TX,UT-1} \cdot \begin{pmatrix} h_{11} G_{RX,AP-1} w_{11}^* \\ +h_{21} G_{RX,AP-2} w_{12}^* \\ +h_{31} G_{RX,AP-3} w_{13}^* \end{pmatrix} = 1, \tag{2.21}$$

to obtain an estimate of x_1, and:

$$\text{(Cond. 2 — Reverse)} \quad G_{TX,UT-2} \cdot \begin{pmatrix} h_{12}G_{RX,AP-1}w_{11}^* \\ +h_{22}G_{RX,AP-2}w_{12}^* \\ +h_{32}G_{RX,AP-3}w_{13}^* \end{pmatrix} = 0, \tag{2.22}$$

to remove the effect of the interferer x_2 at the output of the access point combiner for x_1. Also in the forward link, the constraints on the transfer function are:

$$\text{(Cond. 1 — Forward)} \quad G_{RX,UT-1} \cdot \begin{pmatrix} h_{11}G_{TX,AP-1}w_{11}^* \\ +h_{21}G_{TX,AP-2}w_{12}^* \\ +h_{31}G_{TX,AP-3}w_{13}^* \end{pmatrix} = 1, \tag{2.23}$$

to transmit to UT-1 and:

$$\text{(Cond. 2 — Forward)} \quad G_{RX,UT-2} \cdot \begin{pmatrix} h_{12}G_{TX,AP-1}w_{11}^* \\ +h_{22}G_{TX,AP-2}w_{12}^* \\ +h_{32}G_{TX,AP-3}w_{13}^* \end{pmatrix} = 0, \tag{2.24}$$

to minimize the contribution of x_1 at UT-2. Under the assumption that a zero forcing algorithm is used, Ung shows that the sufficient hardware condition to respect reciprocity is to apply a calibration weight $K_{AP}W_{CAL,m}$ at the m_{th} access point branch during the forward link to maintain an equal branch gain during forward and reverse link, i.e. $K_{AP}W_{CAL,m}G_{AP,TX-m} = G_{AP,RX-m}$. The variable K_{AP} is constant for all transmit branches and models the fact that the AP front-end branches must maintain a constant of proportionality between the forward link and reverse link, and are not restricted to be equal. The calibration weight vector $K_{AP}W_{CAL,m}$ is obtained at system initialization and in Ung's design an additional antenna is added at the access point to calculate the weights.

Alternatively if the weights are calculated with an MMSE algorithm the conditions for the same two-user three-antenna access point example is constrained with the following four equations:

$$\text{(Cond. 1 -- Reverse)} \quad G_{TX,UT-1} \cdot \begin{pmatrix} h_{11} G_{RX,AP-1} w_{11}^{*} \\ +h_{21} G_{RX,AP-2} w_{12}^{*} \\ +h_{31} G_{RX,AP-3} w_{13}^{*} \end{pmatrix} = 1, \tag{2.25}$$

$$\text{(Cond. 2 -- Rvs.)} \quad \underset{\mathbf{w}_1}{\arg\min} \left| G_{TX,UT-2} \begin{pmatrix} (h_{12} G_{RX,AP-1}) w_{11}^{*} \\ +(h_{22} G_{RX,AP-2}) w_{12}^{*} \\ +(h_{32} G_{RX,AP-3}) w_{13}^{*} \end{pmatrix} + \mathbf{n}\mathbf{w}_1^{H} \right|, \tag{2.26}$$

$$\text{(Cond. 1 -- Forward)} \quad \frac{G_{RX,UT-1}}{\|\mathbf{w}_1\|} \cdot \begin{pmatrix} h_{11} G_{TX,AP-1} w_{11}^{*} \\ +h_{21} G_{TX,AP-2} w_{12}^{*} \\ +h_{31} G_{TX,AP-3} w_{13}^{*} \end{pmatrix} = 1, \tag{2.27}$$

$$\text{(Cond. 2 -- Forward)} \quad \underset{\mathbf{w}_1}{\arg\min} \left| \frac{G_{RX,UT-2}}{\|\mathbf{w}_1\|} \cdot \begin{pmatrix} h_{12} G_{TX,AP-1} w_{11}^{*} \\ +h_{22} G_{TX,AP-2} w_{12}^{*} \\ +h_{32} G_{TX,AP-3} w_{13}^{*} \end{pmatrix} + n \right|. \tag{2.28}$$

If we follow the same procedure as Ung, we first define a calibration weight $W_{CAL,m}$ such that $K_{AP} W_{CAL,m} G_{AP,TX-m} = G_{AP,RX-m}$ to equalize the interference contribution in parenthesis between the reverse and forward link. Contrarily to the zero forcing algorithm we see that this condition is no longer sufficient to insure reciprocity, because Equations (2.26) and (2.28) are not equal to zero as was the case in the zero-forcing situation. In order to maintain the same signal to noise and interference ratio between the forward and reverse link a solution is to also calibrate the user terminal front-ends such that $K_{UT} W_{CAL,UT-v} G_{TX,UT-v} = G_{RX,UT-v}$ for each user v. The calibration factor K_{UT} is constant for all user terminals and is equal to $K_{UT} = K_{AP}$. As a consequence, we find that not only is calibration of the AP branches necessary, to maintain the same performance in the reverse and forward link using the MMSE algorithm, it is also necessary to scale the UT branches to effectively maintain equal $SINR$ conditions in the reverse and forward link.

2.4 Antenna Arrays

Antenna arrays are simply a set of antenna elements simultaneously processing a desired signal, in effect increasing the communication performance. Using antenna arrays the directivity of the antenna, defining the concentration of energy in a given direction, can be modified by applying a weight at each antenna element. As defined in [28], the array pattern defined as the radiation intensity as a function of angle depends on each individual element pattern as well as on the array factor. Furthermore, the array factor is defined as the radiation pattern of the antenna array where all the elements are replaced with an isotropic point source.

In this Section we describe the characteristics of antenna arrays for use in multiple user environments. We will initially describe a simple structure, the linear antenna array, to explain the behavior of antenna arrays for application in a multiuser environment. Finally we will explain the design procedure in developing a circular antenna array at 5.6 GHz inspired from a design presented in [29].

2.4.1 Linear Antenna Arrays

A linear array of antenna elements contains M elements. If each element is modeled as an isotropic source the array factor can be determined and in [30] the array factor is demonstrated for a transmitting array. The radiated field of an isotropic radiator at distance r is proportional to:

$$I_m = \frac{e^{-j\beta r}}{4\pi r} \tag{2.29}$$

where I_m is the current of the point source m and β is the phase constant ($\beta = 2\pi/\lambda$). Because the array factor is independent of distance, and defining the phase difference ε_m at at element m, the array factor becomes:

$$AF = \sum_{m=1}^{M} I_m e^{j\varepsilon_m}. \tag{2.30}$$

An equally spaced linear array with point sources is shown in Figure 2.14. The first element is the reference and its phase is defined at $\varepsilon_0 = 0$. In this case the phase difference is $\varepsilon_m = \beta(m-1)d\cos\theta$ and in a transmit scenario the current in each element is :

$$I_m = A_m e^{j\alpha_n}, \tag{2.31}$$

and the array factor is:

$$AF = \sum_{m=1}^{M} A_m e^{(j\beta(m-1)d\cos\theta + \alpha_m)}. \tag{2.32}$$

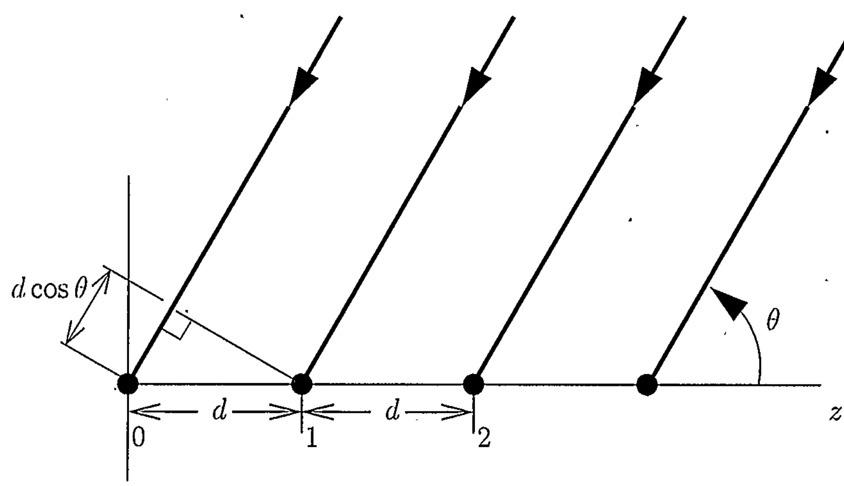

Figure 2.14: Equally Spaced Linear Array of Isotropic Sources.

In Figure 2.15 we show the array factor for a 4-element linear array as well as a 12-element linear array. To simplify the system the same current flows in all branches. We see that the gain is maximum for a 90 degree direction of arrival. Also we see that the beams are narrower with a 12-element antenna array compared to the 4-element and this indicates that spatial separation is more precise as the number of antennas increases.

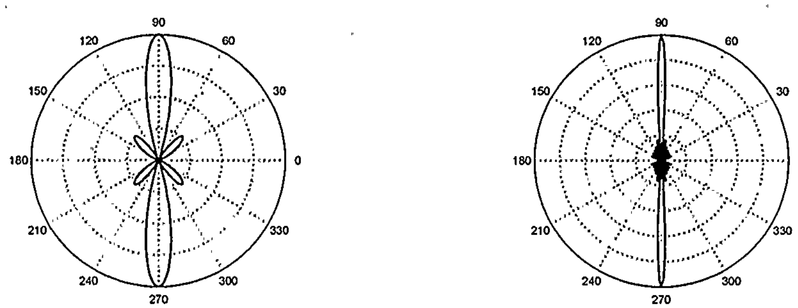

(a) 4 antennas (b) 12 antennas

Figure 2.15: Array Factor For Equally Spaced Linear Array.

2.4.2 Circular Antenna Arrays Design

A 4-element circular antenna is designed for space division multiple access (SDMA) communication. In [29] a 12-element antenna is described for a 1.7-GHz application. In this original design six antennas are horizontally polarized while another six are vertically polarized. In this current project only four antennas can be accommodated by the RF front-ends available and are made vertically polarized. A monopole is used to approximate an isotropic point source. At 5.6 GHz the monopoles' length is approximately $\lambda/4 = 1.3$ cm. Each monopole is surrounded by walls as shown in Figure 2.16 such that the beam width should occupy 90 degrees in space.

For an antenna to radiate, it must allow maximum power transfer with the RF electronics and therefore the impedance match is very important. The measured reflection coefficient for the input port, denoted S_{11}, for each antenna is shown in Figure 2.17. We can see that at 5.6 GHz all antennas have a S_{11} specification below -20 dB which indicates a good impedance match, therefore an optimal power transfer. We

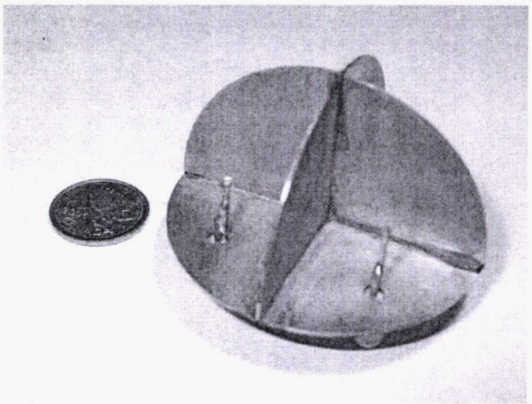

Figure 2.16: Photography of Circular Sectorized 4-Element Antenna Array

also recognize that the impedance match is rather constant over a large bandwidth. Actually all antennas maintain S_{11} below -15 dB between 5.2 GHz and 5.9 GHz.

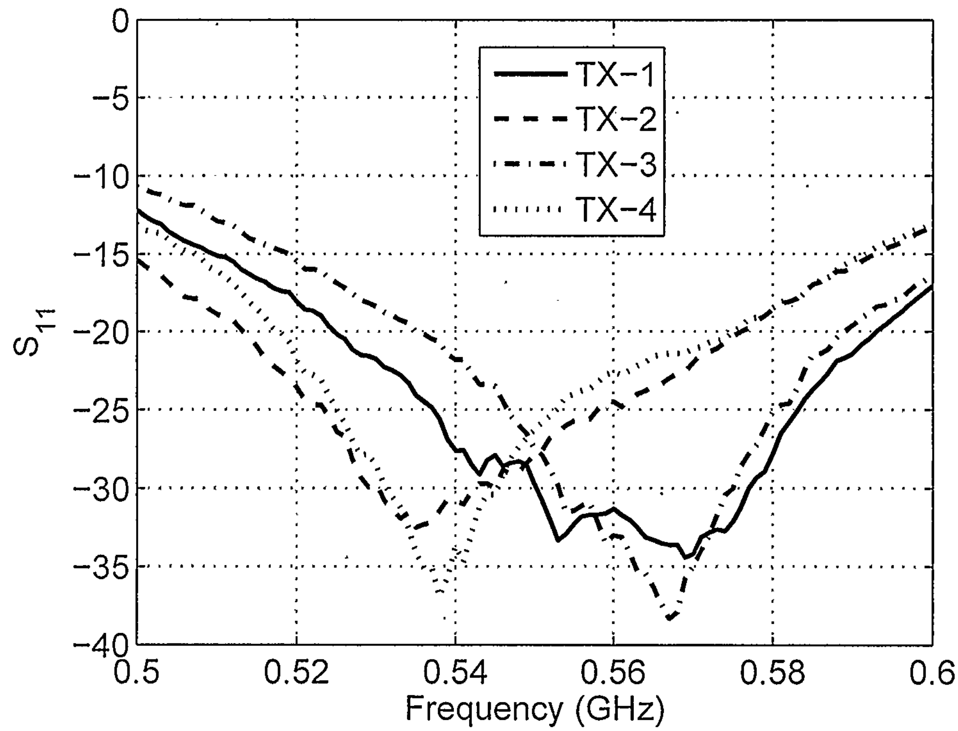

Figure 2.17: Measurements Results for Antenna Array Input Impedance

Chapter 3

Indoor Spatial Wireless Channel

In classical communication performance analysis, the additive white gaussian noise (AWGN) channel typically serves as the first-cut estimate of a wireless system performance. The AWGN model is a very good approximation of low speed, non-mobile channel applications. In mobile channels, small scale variations influence the communication performance. Also, in scattering environments multipath arrivals are the cause of deep fades, as well as dispersion. As the channel dispersion increases relative to the symbol rate, greater intersymbol interference deteriorates the performance of the communication system. Here we intend to characterize an indoor channel for nomadic applications, for which, by definition, the channel remains static for a period of time at least equal to a single connection.

In this Chapter, we present the important sources of noise and their effect at the receiver. Also the wireless channel characteristics between the transmitter and receiver is shown for space-time applications and in particular applied to indoor environments. Finally, we shall describe the methodology followed in this project in obtaining spatial channel measurements. A comparison will made between the models presented in the literature with the parameters extracted from the measurements.

3.1 White Gaussian Noise

In communication theory, noise can be characterized as any signal corrupting the information of interest. A white Gaussian noise source models a random signal with constant power spectral density for all bands of interest. The signal amplitude in the time domain varies at the sample rate and its autocorrelation is a Dirac impulse. The amplitude x follows a Gaussian distribution $N(\mu, \sigma^2)$ with mean $\mu = 0$ and variance σ^2 and, as shown in [31], its probability density function is defined with:

$$f_x(x) = \frac{1}{\sqrt{2\pi\sigma^2}} e^{-x^2/2\sigma^2}. \tag{3.1}$$

The power N_0 of x is equal to σ^2. To succinctly account for the disturbances present in each channel, noise in QPSK systems is treated as a complex random variable. An imaginary component is combined with the real noise source and is also modeled with a Gaussian distribution with $N(0, \sigma^2)$ such that $x_{cplx} = x_{real} + i \cdot x_{imag}$. The resulting power is double that of the real noise source. To obtain the same power as for a real noise source, the signal must be divided by $\sqrt{2}$.

3.1.1 Thermal Noise

Besides responding to electromagnetic signals of interest, receive antennas are also affected by thermal photons which corrupt the message. This thermal noise is dependent on bandwidth and ambient temperature. From [7], the thermal noise power (in Watts) at the input of an antenna is calculated with:

$$P = kT_0 \Delta f \text{ [W]}, \tag{3.2}$$

where k is Boltzmann's constant (given by 1.38×10^{-23} Joules/Kelvin), T_0 is the ambient temperature in Kelvin and Δf is the bandwidth of the system under consideration. Equivalently, the power in dBm at 290 K can be expressed with:

$$P(\text{dBm}) = -173.83 + 10 \log(\Delta f). \tag{3.3}$$

For example, for a signal with a bandwidth limited to 2 MHz, the accompanying thermal noise power is -111 dBm while that of a signal with a bandwidth limited to 20 MHz is -101 dBm.

3.2 Channel Model

In this Section we present the wireless channel model between the transmitter and receiver. The channel model is a combination of different parameters the importance of which varies with the radio application. Here we describe the different parameters useful for multiple input multiple output (MIMO) indoor environments. In particular, we focus our study on multiple access applications where the access point is equipped with multiple antennas while spatially separated multiple users have a single antenna to minimize hardware complexity.

3.2.1 Large Scale Path Loss

A wireless channel is characterized with a mean path loss representing a large scale attenuation between the transmitter and receiver. It has been shown (see [7]) that the mean attenuation $\overline{PL}$ is a logarithmic function of distance d such that:

$$\overline{PL}(d) \propto \left(\frac{d}{d_0}\right)^n, \tag{3.4}$$

where d_0 is a close-in reference distance at which the attenuation is known and n is a path loss exponent. In [7], different path loss exponents are listed for various wireless channel conditions. In free space, the exponent is proven to be $n = 2$, and for clustered indoor environment the author limits the exponent between 4 and 6 to account for attenuation due to obstructions. In [15] channel measurements are taken inside office environments and the author defines $n = 5$ as well as $\overline{PL}(1\text{m}) = 30$ dB. The path loss in dB can be expressed with:

$$\overline{PL}(\text{dB}) = \overline{PL}(d_0) + 10n\log\frac{d}{d_0}. \tag{3.5}$$

Assuming the maximum distance in our indoor environment is 10 meters, the maximum path loss becomes $\overline{PL}(10) = 80$ dB.

3.2.2 Small Scale Fading

In a non line-of-sight(NLOS) scenario, scattering causes multipath arrival at the receiver. The signal received through different channel paths is added at the receiver antenna. In the case where the time delay between the first and the latest non negligible path arrival is small relative to the symbol period, no dispersion occurs, but the signal arrivals may be added constructively or destructively. The addition of destructive (flat-fading) multipath results in a deep fade during which the channel amplitude is very low. To model this fading property in NLOS channels, the amplitude is modeled with Rayleigh (or 'circularly symmetric complex Gaussian') fading statistics. Its probability density function is:

$$f_x(x) = \begin{cases} \frac{x}{\sigma^2}\exp\left(-\frac{x^2}{2\sigma^2}\right), & 0 \le x \le \infty \\ 0, & elsewhere; \end{cases} \tag{3.6}$$

For a signal transmitted through this channel with unit power, the power of the received baseband signal is $P = 2\sigma^2$. The variable x is used to model the channel at different spatial locations, and in a mobile channel, different observations of the channel will follow the distribution of x.

In a line-of-sight (LOS) scenario, although the first path arrival is dominant, an indoor channel is still subject to scattering from objects in the environments and in this case the Rician distribution models the channel amplitude more adequately. The Rician distribution is characterized with a parameter K, defining the ratio between deterministic signal power and variance of the Rayleigh distribution:

$$K = 10\log\frac{A^2}{2\sigma^2}\ \text{[dB]}. \tag{3.7}$$

In a Rayleigh distributed channel the angle of arrival distribution is uniform between $[0, 360]$ degrees. Alternatively, in a deterministic (LOS) channel the angle of arrival is equal to the direction of arrival (DoA) at the receiver. For a Rician channel the angle of arrival is distributed (and follows a Laplacian distribution as explained in [32]) around the mean direction of arrival and its spread decreases as the K factor increases.

Delay spread

As we explained earlier, in a scattering environment, multiple path arrivals are added at the receiver. As the multipath delay increases, the resulting channel $h_{disp}(t,\tau)$ as a function of time t and delay τ contains L discrete path delays and is modeled with:

$$h_{disp}(\tau,t) = \sum_{i=1}^{L} h_i(t)\delta(\tau - \tau_i(t)), \tag{3.8}$$

where $h_i(t)$ represents the amplitude of the channel for delay τ_i at time t. In general, mobility in the channel may affect the channel impulse response in time. To evaluate the received signal at time t, the transmit signal is convolved with $h_{disp}(\tau,t)$.

To quantify the dispersion of the channel, as defined in [7], the mean excess delay $\bar{\tau}$ is:

$$\bar{\tau} = \frac{\sum_{i=1}^{L} h_i^2 \delta_i}{\sum_{i=1}^{L} h_i^2}, \tag{3.9}$$

and the RMS delay spread τ_{RMS} is:

$$\tau_{RMS} = \sqrt{\bar{\tau^2} - (\bar{\tau})^2}, \tag{3.10}$$

where, if we define the channel power $P_i = h_i^2$, $\bar{\tau^2}$ is:

$$\bar{\tau^2} = \frac{\sum_{i=1}^{L} P_i \delta_i^2}{\sum_{i=1}^{L} P_i}. \tag{3.11}$$

For an indoor wireless channel, the delay spread has been shown to vary between 30 nsec $< \tau_{RMS} <$ 180 nsec (see [7]). In [33], channel measurements were taken for various channel conditions and a dispersive channel model was extracted. The authors concluded that the channel contained clusters with each cluster containing multiple path arrivals. In [32] empirical channel models for WLAN 802.11a applications are described and an example of the decaying amplitude profile for a typical office is shown in Figure 3.1. Note that as explained in [32], the amplitude of the first path h_1 is modeled with a Rician distribution while all other paths are modeled with a Rayleigh distribution. In Table 3.1 we present a summary of channel statistical properties as introduced in [32] for different indoor wireless environments.

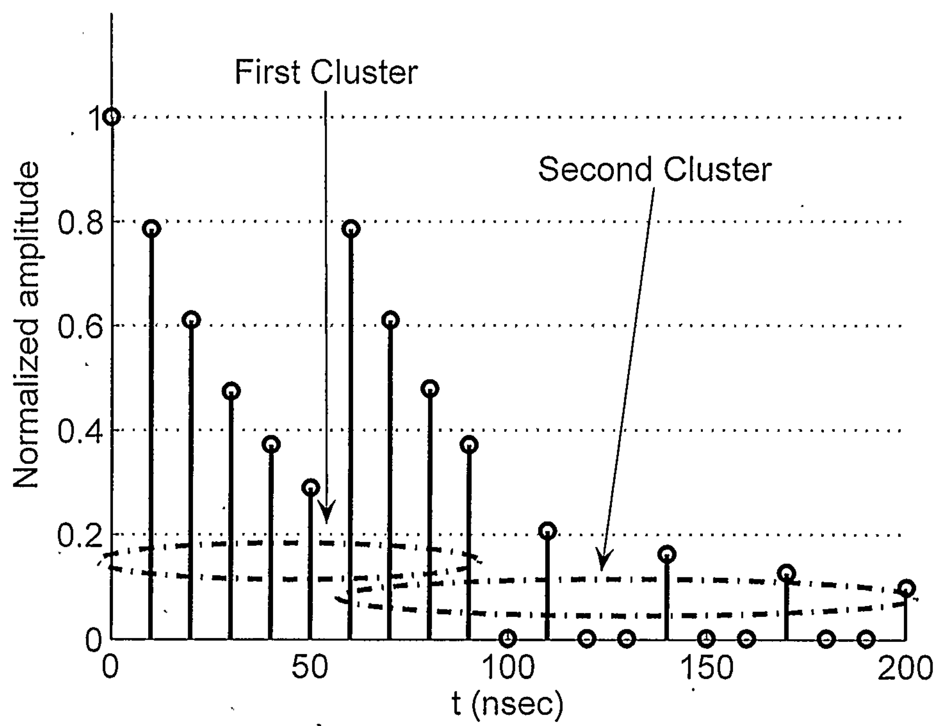

Figure 3.1: Dispersive channel model with multiple clusters.

Doppler spread

Due to motion in the wireless channel, the channel characteristics fluctuate. Not only does each path amplitude $h_i(t)$ vary in time, but so does the path delay $\tau_i(t)$. In [32],

Table 3.1: IEEE Task Group channel model characteristics.

	Typical Office		Large Office	
Condition	NLOS	LOS	NLOS	LOS
Acronym	S1-NLOS	S1-LOS	S2-NLOS	S2-LOS
K (dB)	$-\infty$	3	$-\infty$	6
τ_{RMS} (nsec)	50	30	100	50

the indoor channel is described with an equivalent speed $v_0 = 1.2$ km/hour, from which the Doppler spread at $f_c = 5.6$ GHz is approximately:

$$f_d = \frac{v_0}{c} f_c \approx 6.22 \text{ Hz}. \tag{3.12}$$

Defining the coherence time as the duration over which the channel correlation remains above 0.5 as explained in [7], the coherence time becomes:

$$T_C = \sqrt{\frac{9}{16\pi f_d^2}} \approx 68 \text{ msec}. \tag{3.13}$$

In Figure 3.2 we represent a fading channel with a 6.22 Hz Doppler frequency. Additionally, we represent a quasi-static channel estimated over a period of 40 msec. Using a quasi-static model as defined in [34], the channel is assumed to remain constant between estimations, and the result of the channel estimation is assumed to represent the fading channel at discrete time samples.

Spatial correlation

Spatial correlation measures the resemblance between two spatially separated channels. More precisely the correlation defines how closely the changes in two variables coincide together. The definition of correlation ρ_{xy} between two random variables x (with mean μ_x and standard deviation σ_x) and y (with mean μ_y and standard deviation σ_y) is:

$$\rho_{xy} = \frac{\mathrm{E}[(x-\mu_x)]\mathrm{E}[(y-\mu_y)]}{\sigma_x \sigma_y}. \tag{3.14}$$

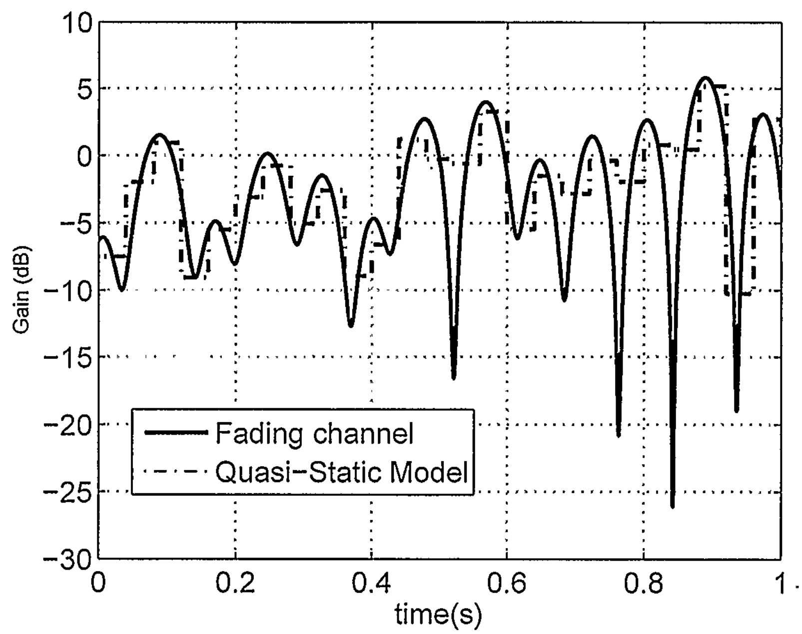

Figure 3.2: Representation of 40 msec quasi-static channel evaluation (f_{dop} = 6.22 Hz).

For an M-element multiple antenna input and U-element multiple antenna output channel, the spatial channel is characterized with $M \cdot U$ random variables which are ordered here such that:

$$\vec{h}_{sp} = [h_{TX_1,UT_1} \; h_{TX_2,UT_1} \; \ldots \; h_{TX_M,UT_U}], \tag{3.15}$$

and the $M \cdot U \times M \cdot U$ correlation matrix for this spatial channel is expressed as:

$$\mathbf{R}_{sp} = \begin{pmatrix} \rho_{(1,1)(1,1)} & \cdots & \rho_{(1,1)(1,2)} & \cdots & \rho_{(1,1)(1,U)} & \cdots & \rho_{(1,1)(M,U)} \\ \rho_{(2,1)(1,1)} & \cdots & \rho_{(2,1)(1,2)} & \cdots & \rho_{(2,1)(1,U)} & \cdots & \rho_{(2,1)(M,U)} \\ \vdots & \vdots & \vdots & \vdots & \vdots & \vdots & \vdots \\ \rho_{(M,U)(1,1)} & \cdots & \rho_{(M,U)(1,2)} & \cdots & \rho_{(M,U)(1,U)} & \cdots & \rho_{(M,U)(M,U)} \end{pmatrix}, \tag{3.16}$$

where $\rho_{(p,v)(q,w)}$ represents the spatial cross-correlation among channels $h_{p,v}$ (between transmit antenna p and user terminal v) and $h_{q,w}$ (between transmit antenna q and user terminal w). To simplify the analysis of the complete channel between the access point and user terminals the correlation matrix can be divided into submatrices. We define a multiple input single output (MISO) correlation matrix $\mathbf{R}_{xm,u}$ between the multiple antenna access point and user terminal u. As shown in Figure 3.3 the spatial correlation between the access point antennas $TX-p$ and $TX-q$ is $\mathbf{R}_{xm,u}(p,q)$. We also define a single input multiple output (SIMO) spatial correlation matrix $\mathbf{R}_{xs,m}$ between transmit antenna m and all user terminals in the channel. In this case the correlation between user terminal $RX-v$ and user terminal $RX-w$ is $\mathbf{R}_{xs,m}(v,w)$ and is represented in Figure 3.4.

3.3 MIMO Channel Measurement

Using a channel sounder described in [15] the indoor spatial channel characteristics are evaluated in the context of a multiple access application. In this Section we

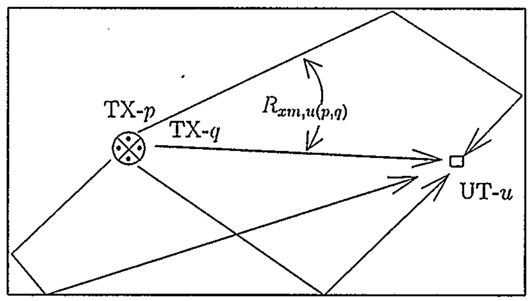

Figure 3.3: MISO Correlation Matrix Definition.

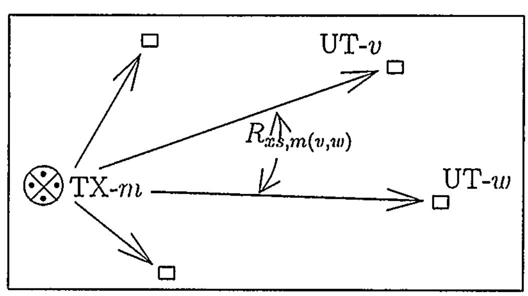

Figure 3.4: SIMO Correlation Matrix Definition

describe the sliding window correlator used for channel measurement followed by the spatial channel measurement methodology and we will conclude with an analysis of the extracted spatial channel information.

3.3.1 Practical Channel Estimation

In this Section we wish to present the sliding window correlator which is a practical implementation of a channel estimator using low power hardware. Channel estimation involves evaluating the impulse response of the channel as a function of the path arrival time. In digital electronics the continuous time channel is represented with a tap delay model.

A straightforward method of evaluating the channel impulse response is to apply an impulse signal at the transmitter and record the signal at the receiver. Such pulse-signal techniques are not common in practice. Alternatively we will demonstrate the possibility of transmitting a pseudo-random sequence x_{ref} at the input of the channel and applying a sliding window correlator at the output of the channel as shown in Figure 3.5.

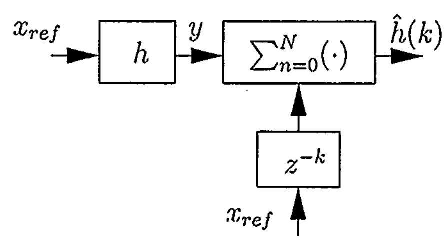

Figure 3.5: Sliding Window Correlator Structure.

First we know that applying a transmit sequence $x_{ref}(t)$ to a multipath channel $h(\nu)$ is equal to the convolution operation such that:

$$y(t) = \int_{-\infty}^{\infty} x_{ref}(t-\nu)h(\nu)d\nu, \tag{3.17}$$

where the integration is applied along the multipath delay ν. At the receiver, a replica of the transmit sequence is generated, advanced by k, and correlated with the received signal. The result is:

$$\hat{h}(k) = \int_{-\infty}^{\infty} R_{xx}(k-\nu)h\nu d\nu, \tag{3.18}$$

and, assuming x_{ref} is a long pseudo-random sequence, the autocorrelation function $R_{xx}(k-\nu)$ is a Dirac function with its impulse at delay k. As a result, the cross-correlation output is a reliable channel estimator at delay k.

To obtain a complete channel characteristics correlation must be repeated for all delays k. An alternative method to retain system causality is to insert a delay k in the received signal rather than advancing the reference signal as explained in [8]. In general, channel estimation is corrupted with noise and at the output of the correlator a threshold must be defined for which the estimation result is assumed reliable.

3.3.2 System Description

In Figure 3.6 we show the channel measurement equipment including the 4-element circularly sectorized antenna at the transmitter and the four user terminals receiver whose monopole antenna is connected to the receiver hardware through a low-loss RF cable.

Using 2 dual-channel arbitrary waveform generators (AWGs) four independent transmit sequence can be sent by the transmitter. Each AWG channel is programmed to send a 2047-chip periodic PN sequence. The chip rate is 200 Mcps and the signal is oversampled by 5 and later pulse shaped using a root-raised-cosine filter. As represented in Figure 3.7, a common PN sequence is used for all transmit channels but is offset by $\Delta_o = 414$ chips. This methodology is used to estimate a multiple input single output (MISO) spatial channel using a single correlation at a receiver elements' baseband processor. At each transmit branch, the data is converted to analog and applied to the front-end hardware circuitry. The front-end hardware is limited to four branches. The antenna shown in Figure 2.16 is connected to the channel sounder and represents a typical antenna array at an access point for spatial multiplexing (the reflecting walls between the elements allow the signals to be directed in four different quadrants).

Each user antenna is a simple monopole and is connected to the channel sounder receiver through 4-meter low-loss RF cables. This allows us to spatially separate the users. There are four front-end elements at the receiver. Using a superheterodyne architecture, the output of each front-end is down converted to an intermediate frequency $f_{IF} = 500$ MHz and the result is sampled at 2 GHz and input to its respective receive channel of the LeCroy digital scope. The LeCroy digital scope is equipped with a Windows operating system. The data at each channel can be saved and a Matlab interface allows further offline digital processing. For each receive channel, initially, the digital data must be converted to baseband and filtered using a root raised cosine filter. The baseband data is oversampled by 10.

Concerning the receiver baseband processing, at the reference receive branch, a single period of the PN sequence is recuperated and is correlated with the transmit PN sequence for all delays. In normal mode of operation, in each window, 4 peaks are present belonging to the transmit sequence of each transmit antenna. An example of the cross-correlation result is shown in Figure 3.8, for the receive channel RX-1. We see that the approximate peak separation (the separation may change due to different delays in the channel) is different between the last transmit channel and the first transmit channel. Because of this observation, each individual wireless channel can be identified and associated with each transmit antenna. Also, reordering all other receive channels to respect the same timing information obtained from the reference receive channel allows for a complete MIMO spatial channel characterization.

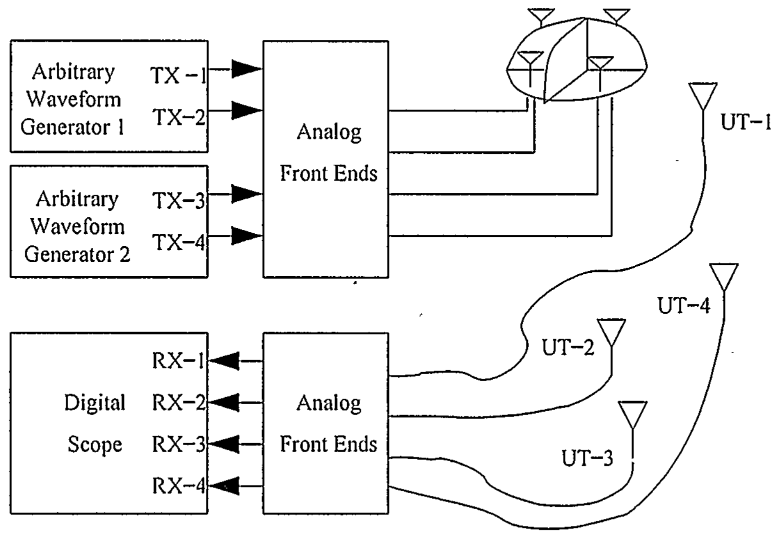

Figure 3.6: Channel measurement equipment.

In this project we wish to evaluate the characteristics of a 20-MHz channel, which is the bandwidth occupancy of current WLAN standards. The channel sounder hardware was originally developed to allow characterization of a 200-MHz channel and to reduce the bandwidth, the cross correlation result representing the frequency selective amplitude may be filtered with a digital low pass filter. Here, the digital filter chosen is an FIR equiripple filter with a band pass frequency of 20 MHz, and a bandstop frequency of 24 MHz. It is sampled at 2 GHz. This type of filter is chosen for its high out-of-band rejection and high in-band linearity.

Channel measurements are taken for different system configurations shown in Figure 3.9. The room A (Rm-A) size is 4.6×5.2 meters while the room B (Rm-B) size dimensions are 6.6×5.6 meters. For the first configuration, the transmitter is situated at the center of Room A and the users are evenly separated such that the direction of arrival is very different for each user. In the second configuration, the transmitter is situated at one extremity of Room A and the users are situated at the

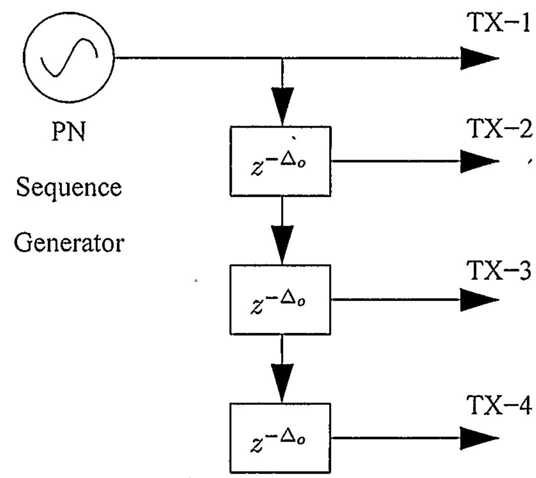

Figure 3.7: AWG Transmit Sequences.

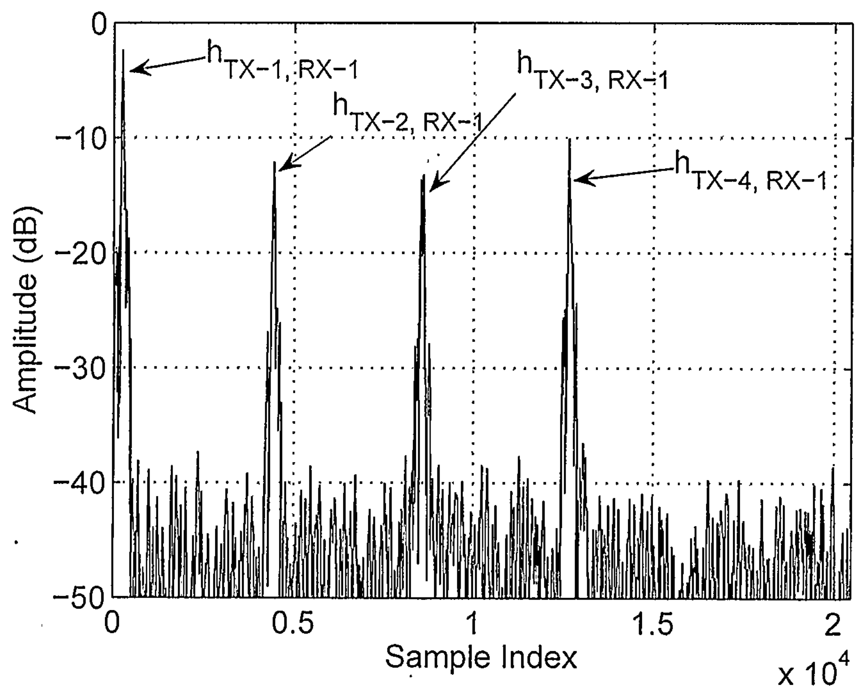

Figure 3.8: Example of cross correlation performance for receive channel RX-1.

other extremity, the angle separation is small between users. Finally, in the third configuration the transmitter is situated in Room B while the receiver is in Room A. Note that a door giving access to Room B is open while the measurements are taken.

For each configuration, $N = 400$ spatial channel measurements are taken in a short time span (approximately 10 minutes). Between each measurement, the transmitter is moved within a one meter square area. The displacement is limited within this area to retain an approximately constant path loss and therefore small scale fading is the major contribution to the channel variations. We can assume that the relative angle between the transmitter and receiver is maintained for two reasons: a) the maximum displacement is small relative to the distance between the transmitter and the user terminals and b) the displacement consists of a translation of the transmitter array without rotation. Because the incremental displacement Δd is of the same order of the signal half wavelength ($\lambda = 2.7$ cm), the channel should appear somewhat uncorrelated between observations.

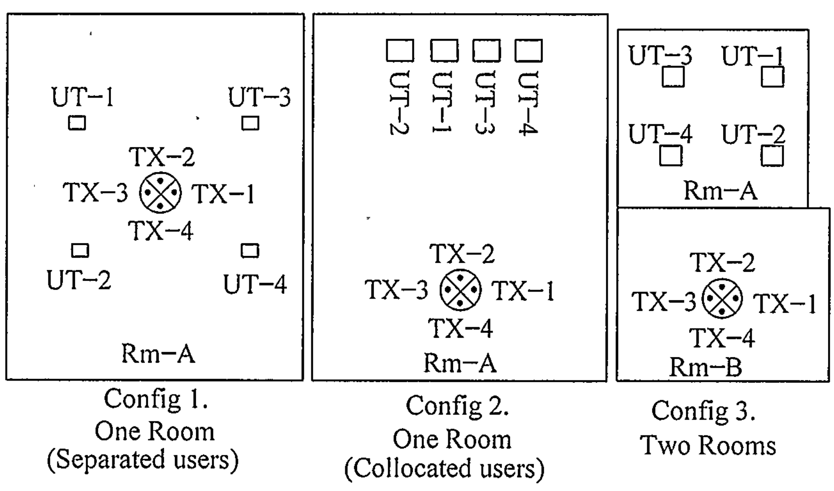

Figure 3.9: Measurement configuration.

3.3.3 Data Analysis

In this Section we analyze the result of the measured channels estimated. After cross-correlation, the $N = 400$, 4x4 channel measurements are concatenated to represent a time-varying (quasi-static) channel model. The set of measurements is normalized with a single value such that the mean spatial (multi-antenna, multiuser) channel power is unitary. Assuming $\mathbf{h}_{u,1}$ represents the first path of the M-element spatial channel to user u, the normalizing factor N_f is:

$$N_f = \frac{1}{N \cdot M \cdot U} \cdot \sum_{n=1}^{N} \sum_{u=1}^{U} \mathbf{h}_{u,1}^H \cdot \mathbf{h}_{u,1}. \tag{3.19}$$

Note that although the first path is used to evaluate the normalizing factor, all paths are normalized with respect to this factor. The resulting normalized multipath channel is characterized. In a first instance we shall demonstrate that although the spatial channel is globally normalized, each individual channel is characterized with a different path attenuation. Also, an analysis of the statistical behaviour of the first path amplitude is followed by the description of the dispersive power profile. Finally the spatial correlation properties for each configuration are explained.

Mean Path Attenuation

Because the sectorized antenna array presents different shadowing conditions to each user, the mean power between each transmitter element and a user terminal element are unequal. Table 3.2 presents a summary of the mean path attenuation between each transmit antenna $TX - m$ and receive antenna $UT - v$ for each configuration. Also shown in this Table is the total power between the AP and a single UT (the power associated with each transmit antenna is summed for each MISO).

For a given configuration, intuitively, we expect a path with direct line-of-sight to have a smaller path attenuation than that with a non-line-of-sight link. Evidently this is because the actual path taken between the transmitter and receiver is longer

Table 3.2: Measured Channel Mean Normalized Linear Power Gain.

		TX-1	TX-2	TX-3	TX-4	Total MISO
Config. 1 LOS Separated	UT-1	0.29	0.21	1.76	5.61	7.87
	UT-2	2.06	0.76	0.67	0.40	3.90
	UT-3	0.87	1.19	0.26	0.36	2.7
	UT-4	0.31	0.18	0.27	0.79	1.6
		TX-1	TX-2	TX-3	TX-4	Total MISO
Config. 2 LOS Colocated	UT-1	1.32	0.34	1.00	0.80	3.47
	UT-2	2.79	1.01	1.78	0.86	6.43
	UT-3	1.03	0.57	0.73	0.46	2.79
	UT-4	1.18	0.52	0.98	0.63	3.3
		TX-1	TX-2	TX-3	TX-4	Total MISO
Config. 3 NLOS	UT-1	1.07	0.82	0.51	1.04	3.44
	UT-2	1.30	0.60	1.58	4.72	8.20
	UT-3	0.49	0.22	0.41	1.05	2.17
	UT-4	0.57	0.34	0.37	0.92	2.19

in the case of the non-light-of-sight scenario. Also, users closer to the transmitter will have a smaller path attenuation.

When comparing the channels for configuration 1 (C1) we expect to obtain a greater power for the transmitting antenna which is in direct line of sight with the receiving antenna. The other antennas at the access point are isolated with the sector walls. The results in Table 3.2 indicate that the receiving element UT-1 seems to receive signals from all antennas with lesser attenuation. This may be due to the fact that the channel sounder could not be calibrated with the flexible 1.5-meter user terminal cables and large fluctuations in the cable loss may have been the origin of such a situation. Nonetheless, for receive elements UT-3 and UT-4 the channel from transmit antenna TX-4 and TX-2 respectively obtain the lowest mean path attenuation as expected. As for receive elements UT-1 and UT-2, with a beampattern rotated (by approximately 30 degrees) counterclockwise from what is shown in Figure 3.9 the greatest path loss agrees with the results (TX-4 and TX-1 respectively) shown in Table 3.2.

For configuration 2 (C2), although the multipath excess delay is short relative to the LOS (the scattering walls are situated very close to the transmitter and receiver), we expect the transmit antenna TX-2 closest to the receiving antennas to admit the smallest attenuation. In contrast, we expect transmit antenna TX-4 to show the greatest path attenuation. In accordance with these assumptions, TX-4 is shown in Table 3.2 to have the lowest normalized power gain for all receivers. Interestingly we find that TX-1 and TX-3 have a greater normalized power gain to all receivers than TX-2. This may be due to the fact that the multipath is binned in the first discrete channel path arrival and is added constructively with the first path. Indeed, using Rm-A dimensions we can approximate the path distances, $d_1 = 5.2$ m and $d_2 = 6.9$ m, and consequently the difference in path arrival is $t_2 - t_1 = 5.8$ nsec. Noting that the channel is precise to $t_{samp} = 12.5$ nsec we find that the second path arrives within the same time sample as the first path.

Concerning configuration 3 (C3) there is no evident LOS. Therefore we expect less variation between channel power. Indeed no relationship can be found between the relative position of each transmit antenna and each receive antenna and the mean channel power.

Tap Amplitude Statistical Characterization

For each channel, the $N = 400$ observations first path's amplitude are represented with a probability density function, from which a cumulative distribution function (CDF) is extracted. The result is compared with a Rician curve and a minimum square error (MSE) method is used to find the Rician distribution A^2 and σ^2 representing each channel. To give more insight on the methodology, the cumulative distribution function for the channel between TX-1 and UT-1 for C1 is shown in Figure 3.10 and is compared to its best fit theoretical Rician distribution. The MSE algorithm evaluates the difference at each point i between the measured CDF CDF_{meas} and the theoretical CDF CDF_{theo}, squares the result and sums all points L such that:

$$MSE = \sum_{i=1}^{L}(CDF_{theo}[i] - CDF_{meas}[i])^2. \tag{3.20}$$

The algorithm is repeated for all Rician parameters A^2 and σ^2 in a defined range and the smallest minimum square error is determined to be the closest approximation.

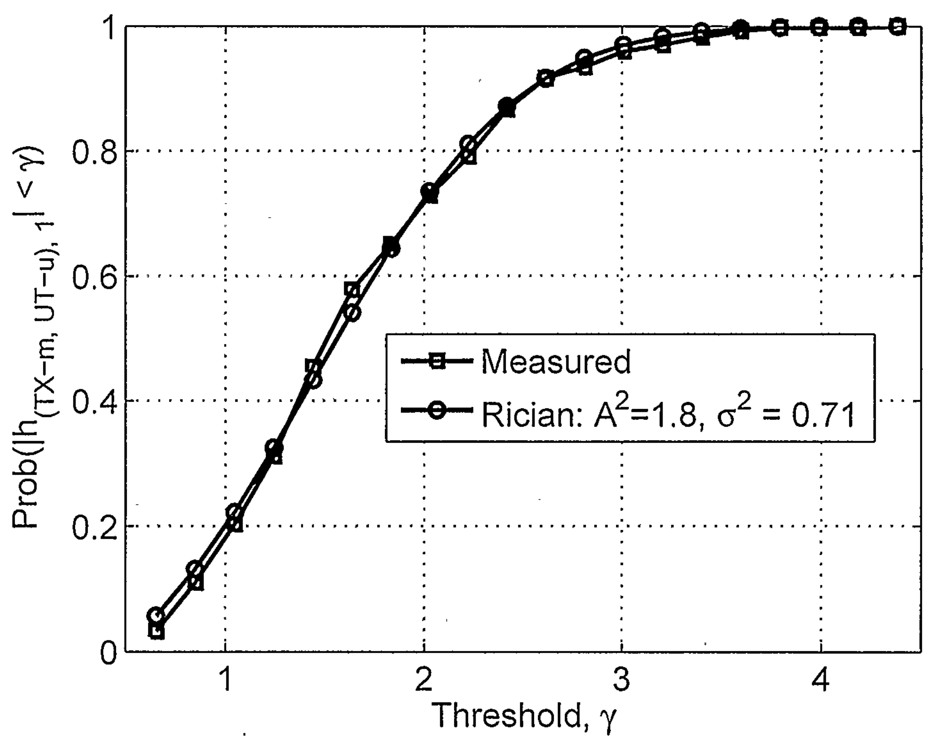

Figure 3.10: Comparison of Measured CDF With Rician for C1, TX-1, UT-1 (MSE = 0.004).

In general, we expect a line-of-sight channel to have a greater Rician K factor because in this case for all measured positions the receiver can be seen by the transmitter, consequently the fading is reduced relative to the deterministic component. In Table 3.3 we present the best fit Rician K factor for all measured channels. We see that for C1 the mean K factor for the MISO to UT-4 is greater than for other UTs.

This is explained because the transmitter was slightly closer to UT-4 (not exactly centered as shown in Figure 3.9). In configuration 2, the smallest MISO mean K factor belongs to TX-4 which contains no LOS to the receivers. The K factor for all channels in configuration 3 are lower than for the two previous configurations and is easily explained because there is no line-of-sight. In Table 3.5 we show the mean K factor for each spatial configuration. It confirms our assumptions where we expected C1 to obtain on average the greatest K factor while C3 was expected to obtain the smallest mean K factor.

Table 3.3: Measured Channel Best Fit Rician K Factor (dB).

		TX-1	TX-2	TX-3	TX-4	⟨MISO⟩
Config. 1	UT-1	0.6	-0.3	-4.0	4.2	1.1
LOS	UT-2	-0.1	**-26.5**	-1.2	2.5	-0.6
Separated	UT-3	-18.4	1.2	3.0	4.8	2.0
	UT-4	**9.8**	4.8	5.3	5.9	7.0
	⟨SIMO⟩	4.7	1.2	2.1	4.5	
		TX-1	TX-2	TX-3	TX-4	⟨MISO⟩
Config. 2	UT-1	2.4	3.0	3.0	3.2	2.9
LOS	UT-2	1.9	2.2	-3.0	**-16.5**	-0.3
Colocated	UT-3	**4.1**	3.7	**4.1**	1.5	3.4
	UT-4	1.1	3.2	4.0	1.1	2.5
	⟨SIMO⟩	2.5	3.1	2.7	0.8	
		TX-1	TX-2	TX-3	TX-4	⟨MISO⟩
Config. 3	UT-1	1.4	1.3	1.8	3.0	1.9
NLOS	UT-2	1.0	2.4	3.5	2.6	2.5
	UT-3	3.6	0.6	**3.7**	3.6	3.0
	UT-4	0.9	**0.5**	2.1	2.0	1.4
	⟨SIMO⟩	1.9	1.3	2.8	2.8	

Dispersive Characteristics

In Table 3.4 we present the mean RMS delay spread τ_{RMS} for all channels of each configuration. We also present the mean RMS delay spread for each MISO and SIMO. In Table 3.5 the mean RMS delay spread for each configuration is also shown.

As expected the LOS configuration with separated users situated relatively close to the transmitter has the shortest delay spread. This is certainly due to the lack of scatterers in proximity of the antennas. In contrast C2 has scattering walls in the vicinity of the transmitter and receiver and this causes the delay spread to increase. Interestingly the average delay spread for C2 is even greater than for C3, the NLOS scenario. Actually the delay spread for C3 is relatively small and this may be due to the open door between room A and room B which could have caused an aperture effect: the main contribution for each channel is the path through the door, while all other paths are attenuated through the drywall. Another hypothesis is that the effect of the single drywall does not scatter the penetrating electromagnetic wave as highly as expected.

Table 3.4: Measured Channel Delay Spread τ_{RMS} (nsec).

		TX-1	TX-2	TX-3	TX-4	⟨MISO⟩
Config. 1 LOS Separated	UT-1	52.4	26.7	36.3	47.6	40.8
	UT-2	51.1	32.0	26.8	51.5	40.4
	UT-3	29.1	39.3	**53.9**	51.34	43.4
	UT-4	**18.9**	50.83	49.7	39.0	39.6
	⟨SIMO⟩	37.9	37.2	41.7	47.4	
		TX-1	TX-2	TX-3	TX-4	⟨MISO⟩
Config. 2 LOS Colocated	UT-1	53.7	**42.1**	59.3	56.0	52.8
	UT-2	67.4	46.3	59.5	63.8	59.3
	UT-3	55.2	47.3	62.6	58.9	56.0
	UT-4	57.2	55.8	**70.0**	65.4	62.1
	⟨SIMO⟩	58.4	47.9	62.8	61.0	
		TX-1	TX-2	TX-3	TX-4	⟨MISO⟩
Config. 3 NLOS	UT-1	40.3	37.5	52.0	49.1	44.7
	UT-2	37.1	42.0	**57.0**	49.5	46.4
	UT-3	48.6	34.5	52.6	53.4	47.3
	UT-4	43.1	**28.4**	44.1	45.5	40.275
	⟨SIMO⟩	42.3	35.6	51.4	49.4	

Spatial Correlation

To complete the analysis of the measured channels we also compute for each configuration the spatial correlation between channels. The first path of each channel is ordered to follow the structure in Equation 3.15 and the complete space correlation matrix dimensions are 16x16. To simplify analysis, the mean spatial correlation for each MISO as well as for each SIMO as explained in Section 3.2.2 is represented in Table 3.5. Note that for C3, the MISO correlation to UT-1 is highest (0.21) indicating that the channel fluctuations are similar for all transmit antennas. In an NLOS environment this behaviour is unexpected. Once again this can be explained because the path through the door is common for all transmit antennas resulting in highly correlated channels. Finally, we can see that generally the mean spatial correlation for SIMOs is low, due to the spatial separation between users.

Table 3.5: Measured channel characteristics.

	Config. 1 LOS	Config. 2 LOS	Config. 3 NLOS
$\langle K \rangle$ (dB)	3.38	2.30	2.16
$\langle \tau_{RMS} \rangle$ (nsec)	41.0	57.5	44.7
$\langle R_{MISO,1} \rangle$	0.08	0.08	**0.21**
$\langle R_{MISO,2} \rangle$	0.08	0.11	0.10
$\langle R_{MISO,3} \rangle$	0.11	**0.01**	0.09
$\langle R_{MISO,4} \rangle$	0.15	0.09	0.16
$\langle R_{MISO} \rangle$	0.11	0.07	0.14
$\langle R_{SIMO,1} \rangle$	**0.01**	0.03	0.04
$\langle R_{SIMO,2} \rangle$	**0.01**	**0.08**	0.04
$\langle R_{SIMO,3} \rangle$	0.03	0.05	0.02
$\langle R_{SIMO,4} \rangle$	0.02	0.03	0.05
$\langle R_{SIMO} \rangle$	0.02	0.04	0.04

Chapter 4

Space-Time Coding For Diversity And Multiple Access

In this Chapter we describe practical multiple access algorithms for indoor wireless channels. A space-time approach incorporating CDMA and SDMA is considered here (Section 4.3). By endowing the network with additional degrees of freedom space-time codes allow for interference suppression while simultaneously profiting from the channel diversity present in fading channels. The component parts are considered separately with Section 4.1 discussing SDMA in detail for the forward and reverse link. Hardware constrained CDMA systems are described in Section 4.2.

4.1 Antenna Arrays in Flat Fading Environments

Time division multiple access (TDMA) and code division multiple access (CDMA) are widely implemented in current standards as a means to share the wireless channel among multiple users. In this project, space division multiple access (SDMA) is proposed as a part of an alternative multiple access scheme. Compared to TDMA where users are allocated a dedicated time slot, and CDMA which spreads the data over a greater bandwidth, SDMA allows simultaneous communication in a single frequency allocation occupied by multiple users [35]. This advantage is very attractive, particularly in licensed spectra, for which the service supplier must pay royalties.

In classical SDMA systems beamforming consists in using multiple antennas to receive replicas of a desired signal which is applied a weight vector nulling the response of the receive antenna array in an interferer's direction of arrival [36]. In modern data networks, SDMA technology must not only consider point-to-point communication in the presence of interference, but rather must process multiple parallel data streams belonging to various users.

To exact control over the receive (or transmit) pattern, SDMA requires the use of antenna arrays. Because user terminals are generally constrained in size, antenna arrays are generally set up at the access point. Thus, a typical SDMA scenario has the multiple-antenna access point dealing with multiple single-antenna users simultaneously. Specifically, in the reverse link, the access point receiver weights the signals received in each antenna branch to maximize and separate the received user signals. Comparatively, in the forward link, the access point precodes the signal with a spatial signature to change directivity of the antenna array and therefore separate users in orthogonal spatial channels. In addition to its multiple access capability, in recent years, antenna array system have been recognized as an efficient means of implementing diversity schemes for single user networks in fading channels [37]; also great capacity improvements are expected when multiple antennas are present at both the transmitter and receiver thus realizing a multiple-input multiple-output (MIMO) system [38, 39].

In this section, we will show the performance of the spatial filter implemented at the access point as described in Section 2.1. Firstly, we will explain the algorithm during the reverse link, followed by two algorithms for the forward link, one chosen for its implementation simplicity, and the other for its superior bit error rate (BER) performance.

4.1.1 Reverse Link

On the reverse link, the spatial filter is implemented at the access point receiver equipped with M antennas. Here, U users share a single frequency allocation, and transmit simultaneously to the access point as shown in Figure 4.1.

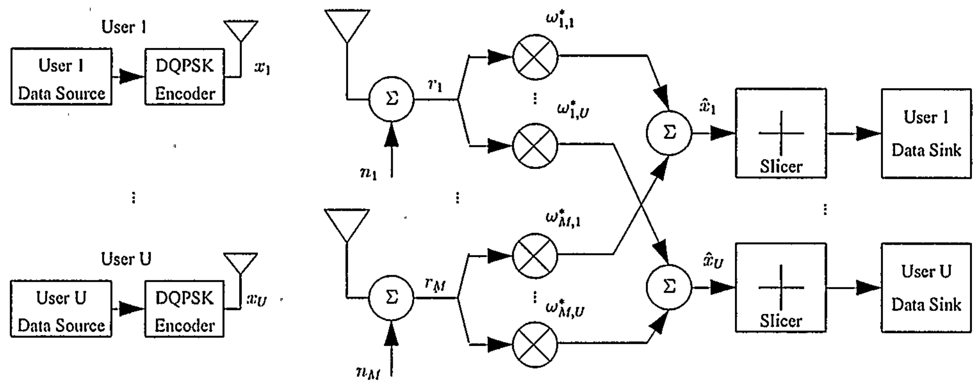

Figure 4.1: Spatial filter for multiuser access in reverse link

A DQPSK data symbol from user u is a complex value represented by the variable x_u input to the channel. The flat fading channel between user u and the access point antenna array is a complex column vector, denoted $\mathbf{h}_u \in C^{M\times 1}$. The total received signal from all users is:

$$\mathbf{r} = \sum_{u=1}^{U} \mathbf{h}_u x_u + \mathbf{n}, \tag{4.1}$$

where $\mathbf{n}$ and $\mathbf{r} \in C^{M\times 1}$ are complex column vectors with M elements. The vector $\mathbf{n}$ represents thermal noise at the combiner input, and is modeled with a white Gaussian random process. The variance of the white noise is N_0.

At the antenna array baseband output, the weight column vector $\mathrm{w}_u \in C^{M\times 1}$ is calculated for user u using a minimum mean square error (MMSE) algorithm (altogether U w_u weight vectors are needed to recover all U signals). Finding a weight vector that minimizes the error for each user allows multiple data streams to be decoded in parallel at the access point. The transmitted signal estimated for user u at the combiner output is:

$$\hat{x}_u = \mathrm{w}_u^H \mathbf{r}. \tag{4.2}$$

In [40], Winters describes the optimum combiner receiver for antenna arrays in a frequency-flat Rayleigh fading environment, and shows that the optimum weights applied at the antenna array are determined by the Wiener-Hopf equation.

The Wiener-Hopf equation is used to solve for the MMSE problem in a system equipped with multiple inputs and in the following paragraphs we shall explain its construction as applied to spatial filters followed by a performance analysis.

The antenna array interference and noise contribution can be evaluated with the covariance matrix, defined with:

$$\mathbf{R} = \mathrm{E}[\mathbf{r}_{und}\mathbf{r}_{und}^{H}], \tag{4.3}$$

where $\mathbf{r}_{und}$ is the undesired component (interference and noise) in the $\mathbf{r}$ signal. The ensemble average is used to remove the dependency of $\mathbf{r}_{und}$ on the transmit sequence.

The cross-correlation vector $\mathbf{p}_v$ between the desired signal for user v, x_v, and the transmitted signal is:

$$\mathbf{p}_v = \mathrm{E}[x_v \cdot \mathbf{r}]. \tag{4.4}$$

Note that in the evaluation of the SDMA filter performance, we use a quasi-static channel model as defined in Section 3.2.2, for which the channel remains constant during a given observation period. For example, when evaluating the probability of error in fading conditions, the simulations are set such that the channel changes at the symbol rate, while in the evaluation of the mean SNR output, the channel impulse response duration consists of many symbols (greater than 1000 symbols) in order to compute the average noise statistics for each channel amplitude. In this project, we assume that the channel remains constant during the processing of a frame, and the frame size is defined accordingly. The evaluation of the BER performance for all fading conditions can be interpreted as the overall probability of error as different frames are transmitted in different fading conditions.

Now, if we assign for each user, u, the transmit signal power P_u, and consider a noise power at the combiner input of N_0, then the antenna array interference-and-noise covariance matrix to user v, $\mathbf{R}_v$, can be redefined as:

$$\mathbf{R}_v = \sum_{\substack{u=1}}^{\substack{u=U,\\ u\neq v}} P_u \cdot (\mathbf{h}_u \mathbf{h}_u^H) + N_0 \cdot \mathbf{I}, \tag{4.5}$$

while the received cross-correlation vector between the desired user, v, transmit sequence and the received signal at each antenna element can be interpreted as the channel array impulse response (including the transmit power), and Equation (4.4) becomes:

$$\mathbf{p}_v = P_v \cdot \mathbf{h}_v. \tag{4.6}$$

In order to remove the interference present between users the MMSE matrix formulation becomes [40, 37]:

$$\mathbf{R}_v \mathbf{w}_v = \mathbf{p}_v, \tag{4.7}$$

calculating the weights to:

$$\mathbf{w}_v = \mathbf{R}_v^{-1} \mathbf{p}_v. \tag{4.8}$$

Note that, as explained in [11], the weights applied to minimize the mean square error are $\mathbf{w}_v^*$. Also, the weights can be normalized (without changing the BER performance) to obtain a constant received signal power at the combiner output as explained in [41]. This involves the transformation of the inverted covariance matrix. If we define the received signal (rather than limiting it to the interference and noise) covariance matrix as:

$$\mathbf{R}' = \mathrm{E}[\mathbf{r} \cdot \mathbf{r}^H] = \mathbf{R} + P_v \mathbf{h}_v \mathbf{h}_v^H, \tag{4.9}$$

applying the matrix inversion lemma (or Woodbury's identity), we find that:

$$\mathbf{R}'^{(-1)} = \left[\frac{1}{1 + P_v \mathbf{h}_v^H \mathbf{R}^{-1} \mathbf{h}_v}\right] \mathbf{R}^{-1}. \tag{4.10}$$

Because the terms in parenthesis represent a scalar, the inversion of $\mathbf{R}'$ is proportional to R, and yields the same BER performance when used in 4.8 to determine the optimal weights. As explained in [11, 7] the weight solution $\mathbf{w}_v = \mathbf{R}_v'^{(-1)} \mathbf{p}_v$ represents the matrix formulation of the Wiener-Hopf equations.

At the output of the combiner for user v, the signal to interference and noise ratio $SINR_v$ can be expressed with [40]:

$$SINR_v = \left\langle \frac{\left\|\sqrt{P_v} \cdot \mathbf{w}_v^T \mathbf{h}_v\right\|^2}{\left\|\mathbf{w}_v^T (\mathbf{n} + \sum_{u=1}^{u=U, u \neq v} \sqrt{P_u} \cdot \mathbf{h}_u)\right\|^2} \right\rangle. \tag{4.11}$$

Note that in this equation, the noise $\mathbf{n}$ as well as the channels $\mathbf{h}_u$ and $\mathbf{h}_v$ are time varying statistical processes, and $SINR_v$ is averaged over multiple signal samples. A variety of averaging domains are used in practice; in some circumstances, it is interesting to average the SINR over all channel fading variations: this provides a global mean $SINR_{g,v}$. Other conclusions, such as the SINR probability density function (pdf), can be extracted for an averaging process over a single (static) channel observation, in which case it is denoted as the local mean $SINR_{l,v}$. In the latter case, for example, a distribution of local $SINR_{l,v}$ output can be evaluated for a given fading channel process. The two definitions of $SINR_v$ described above are shown in Figure 4.2.

To further analyze this system, it is necessary to consider two cases: the single-user network for which the receiver simplifies to a maximal ratio combiner (MRC) and the multiple user network.

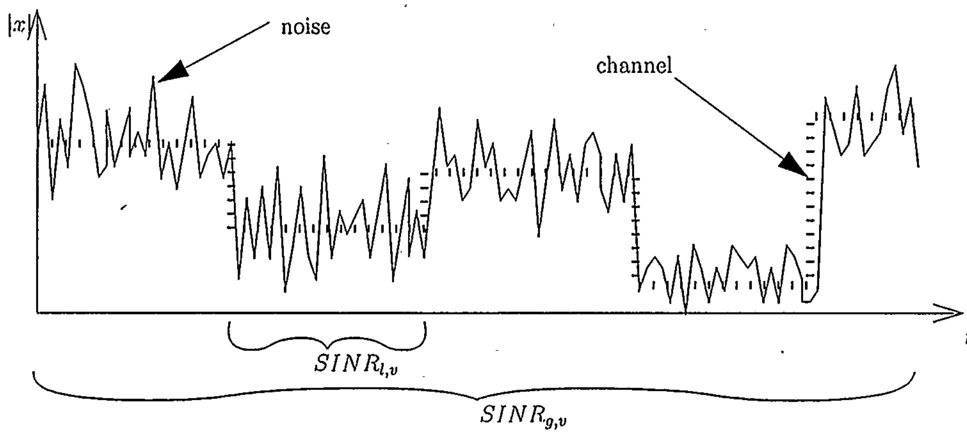

Figure 4.2: Mean SINR definitions in quasi-static channel

Single-User Detection

In a first instance, it is beneficial to analyze the behavior of the system when only one user is present in the network. In this situation, the $\mathbf{R}$ covariance matrix is diagonal and is equal to $N_0 \cdot \mathbf{I}$, where $\mathbf{I}$ is the identity matrix. The inverse becomes:

$$\mathbf{R}^{-1} = \frac{1}{N_0} \cdot \mathbf{I}, \tag{4.12}$$

and the Wiener-Hopf matrix formulation for user v becomes:

$$\mathbf{w}_v = P_v N_0^{-1} \cdot \mathbf{h}_v. \tag{4.13}$$

Equation (4.13) shows that the single user space filter coefficients are simply the complex conjugate of the flat fading channel response scaled by a constant. As mentioned above, this weight calculation implements a maximal-ratio combiner.

It is shown in [7] that the maximal ratio combiner provides a global mean SNR gain given by:

$$SNR_{out} = M \cdot SNR_{in}, \tag{4.14}$$

this statement is valid for fading channels as well as for non-fading channels: combining M identical cophased signals will provide a M^2 power gain, while adding a different noise input sequence will result in a noise power gain of M, proving that the mean SNR gain remains M for the non-fading channel.

The advantage introduced using the maximal ratio combiner in fading environments is diversity: this technique actually reduces the effects of fading. We can appreciate this statement by considering the performance of the MRC in an AWGN channel with multiple antennas: in this scenario, there is no improvement in performance compared to the single antenna case. In contrast, in the case of the Rayleigh, or Rician channel, by using multiple antennas, we are effectively changing the statistics of the equivalent channel. In Figure 4.3, we show the probability of bit error at the combiner output as a function of SNR per bit. The diversity performance is evaluated for various channel Rician factors, K. Also shown are the Rayleigh fading single antenna and white Gaussian channel providing, respectively, lower and upper bound performance. Note that the performance in the Gaussian white noise channel is calculated using:

$$P_e = \mathrm{Q}\left(\sqrt{2 \cdot \frac{E_b}{N_0}}\right) = \frac{\mathrm{erfc}(\sqrt{\frac{E_b}{N_0}})}{2}. \tag{4.15}$$

When comparing the single antenna Rayleigh channel performance with the 4-antenna Rayleigh channel performance, we can appreciate the improvement in bit error rate by adding multiple antennas. For example, to obtain a $BER < 10^{-3}$, the necessary SNR for a 4-antenna receiver is SNR $= 10$ dB, while for a single-antenna receiver, to obtain the same performance, the SNR is greater than 15 dB. Note that as the deterministic component of the Rician channel model increases, the performance improves, due to the fact that the importance of fading decreases. As the K factor increases the performance approaches that of the AWGN channel.

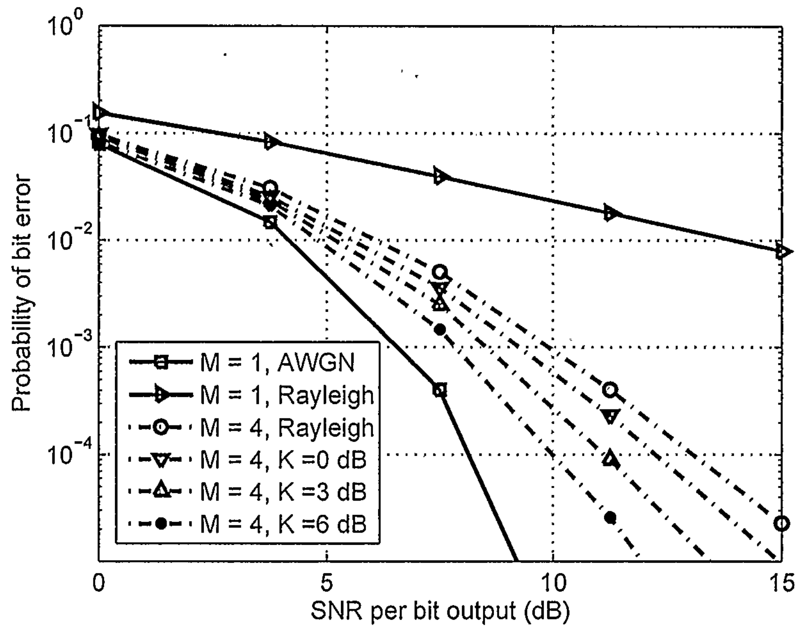

Figure 4.3: Evaluation of diversity performance function of combiner output SNR.

Multiple User Detection

Now, in a network where multiple users can transmit simultaneously over the forward link, the antenna array is used to remove the interference due to users located in the same frequency band. In this case, the antenna array and detector implement SDMA technology proper. Using the Wiener-Hopf equations, the antenna array can theoretically orthogonalize M users transmitting simultaneously.

Here, in order to evaluate the benefit of SDMA for various channel environments, the angle of arrival for each user is included in the model. The antenna array is modeled as a linear uniform structure where each element is separated by a half wavelength ($x_n = \lambda/2$). The resulting signal phase at each branch is calculated using the array factor definition from Section 2.4 and is multiplied with the fading amplitude which is itself modeled with a Rician distribution. To model the Rician distribution a complex Gaussian random variable is generated with a variance $\sigma^2 = 1/2$ in effect generating a channel with unit gain. The result is added a constant value A computed using 3.7 and is finally normalized by $\sqrt{1+A^2}$ to maintain a unitary power. The weight vector found using the Wiener-Hopf equations changes the effective antenna pattern, so as to maximize the desired user's reception.

Two scenarios are evaluated: firstly, the users are assumed to be colocated (users are separated in angle by 5 degrees), secondly, the users are spread in a half plane around the access point (they are equally separated over 180 degrees).

The bit error rate performance is evaluated as a function of user count. To evaluate the system in the presence of noise, at each combiner branch, noise is added to the received signal, and the mean SNR at this point is 12 dB. The results for the simulations on colocated users are shown in Figure 4.4, while the results for the spatially separated users are shown in Figure 4.5.

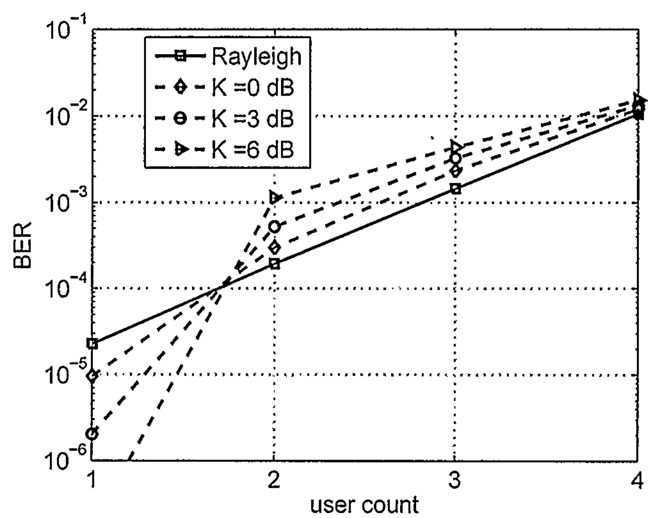

Figure 4.4: Evaluation of colocated multiuser performance function at SNR = 12 dB for various channel models.

In both situations, for a constant input SNR, the performance degrades rapidly as the user count increases. This is due to the fact that the interference reduction is

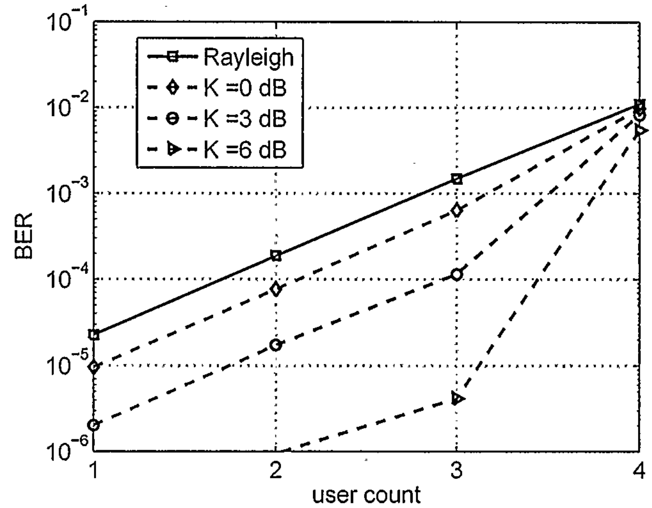

Figure 4.5: Evaluation of separated multiuser performance function at SNR = 12 dB for various channel models.

obtained at the cost of a diversity loss: noise cancellation is reduced.

Also, when comparing the Figures 4.4 and 4.5, we can conclude that for Rayleigh fading environments the angle of arrival parameter can be neglected in the channel model: the performance is equal whether the users are colocated or separated. This is due to the fact that the phase is uniformly distributed for the Rayleigh channel. In contrast, for wireless channels modeled with Rician environments, the user angular separation plays an important role in the communication performance. Because the deterministic component of the channel increases, the angle spread is no longer uniform between 0 and 360 degrees, and varies around the mean angle of arrival (AoA).

We can see that, as the K factor increases, colocated users in a Rician channel obtain a poorer BER performance than colocated users in a Rayleigh channel. Alternatively, separated users in a Rician channel obtain a better performance than in the Rayleigh channel as the K factor increases. We can explain this behavior because in a deterministic channel, the antenna array separates users by modifying its directivity. As the relative variance in the channel decreases (the K factor increases), the AoA variance also decreases, and the mean AoA bears a greater influence on the performance. Hence, when all the users are colocated, it becomes very hard to separate them using a beamforming algorithm, while separated users, can easily be isolated using the antenna array.

4.1.2 Forward Link

In the forward link, the access point must precode the user signal prior to transmission. In general, channel knowledge is assumed, and is used to calculate the optimal weight vector. In this Section, we shall describe the forward link implications for multiuser access in fading channels. We will also describe two valid algorithms to precode the signal in fading channels. The first algorithm ([18]) is a weight reuse solution (calculated during the reverse link) and minimizes hardware complexity. The second solution, a zero-forcing precoder, removes the presence of the interference and obtains the optimal communication performance as seen by the receiver, at the cost of greater transmit power.

Forward Link Spatial Filter Architecture

Before detailing the forward link algorithms under consideration we pause to highlight some important details regarding two different transmission options for either of the two algorithms. Specifically, it can be arranged that either of the two algorithms in question send their pre-weighted signals such that a.) the transmit power is constant or b.) that the received power is constant.

For both algorithms (i.e. the weight re-use and zero-forcing) the general spatial precoder architecture is the same. A schematic of this universal architecture is shown in Figure 4.6. We can observe that the received signal at user v is:

$$r_v = \mathrm{h}_v^T \left(\sum_{u=1}^{U} \mathrm{w}_u^* x_u \right) + n, \tag{4.16}$$

where n is a noise source modeled with a random complex Gaussian process with variance N_0.

In the presence of fading, it is advantageous to evaluate the system performance under a constant transmit power constraint, such as is the case in [42]. If the transmit power at the input of the spatial precoder is P_{TX}, and the noise power measured at the receiver input is N_0, the so-called transmit SNR, defined as,

$$SNR_{TX} = \frac{\mathrm{w}_u^H P_{TX} \mathrm{w}_u}{N_0}, \tag{4.17}$$

becomes the independent variable for further analysis of the communication performance. Note that in order to maintain a constant transmit power, the precoding weights are normalized such that:

$$\mathrm{w}_u = \frac{\mathrm{w}_u^{'}}{\sqrt{(\mathrm{w}_u^{'})^H \mathrm{w}_u^{'}}}, \tag{4.18}$$

where $\mathrm{w}_u^{'}$ represents the unnormalized weight solution. Because weights are applied at the transmitter and the resulting signal vector is normalized prior to application through the fading channel, the receiver effectively sees a channel with reduced flat-fading characteristics where the presence of interference as well as noise have been minimized.

Alternatively, the weights can be computed to maintain a constant channel, $h_{eq,v} = \mathrm{w}_v^H \mathrm{h}_v$, between the AP and user terminal, resulting in a constant received power. As a direct consequence, the fading characteristics are effectively removed prior to transmission. In this case, it becomes more practical to evaluate the performance as a function of received signal to noise ratio, SNR_{RX}. This is similar to approaches presented in [43] and [44], and is particularly interesting in non-fading channels.

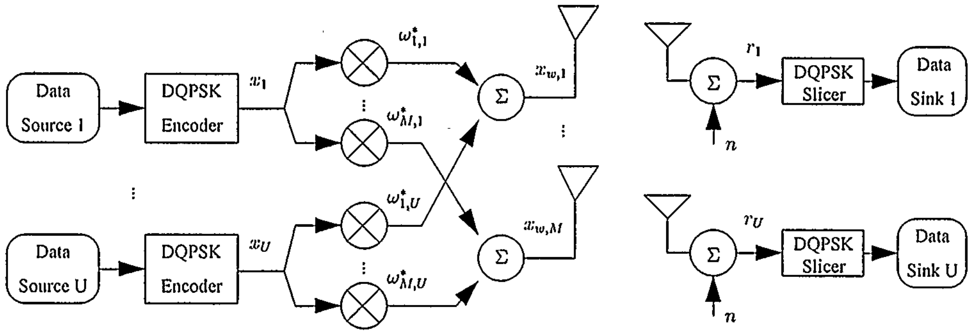

Figure 4.6: Spatial filter for multiuser access in forward link

Because the weights calculated cancel the effect of the channel, and generate an equivalent channel $h_{eq,v} = 1$, the received signal to noise ratio becomes:

$$SNR_{RX} = \frac{P_{TX}}{N_0} \tag{4.19}$$

In this study, a complete evaluation of the system compels us to examine the performance of both a constant transmit and received signal power. The selection of the proper algorithm combined with the proper power normalization scheme are now considered in the selection of an optimal SDMA precoding algorithm.

Weight Reuse Solution

In [18], a transceiver is equipped with a 12-element antenna array to communicate bi-directionally. The author, Ung, assumes that the weights solved in the reverse link can also be applied on the forward link to communicate reliably with multiple users. With this method, the hardware complexity can be minimized, particularly because an adaptive filter, such as that presented in Section 2.1.3 can be implemented during the reverse link to invert the covariance matrix (defined in Equation (4.3)), and consequently applied to find optimum weights for the reverse link.

Application of the weights found on the reverse link to the forward link hinges on the reciprocity of the channel, and this requires several conditions to be in place.

First, it is essential that the fading coherence time is long enough to maintain a constant amplitude for the duration of both the reverse link as well as the forward link. Second, unequal gains, particularly between each transmit and receive AP front-end, can compromise link reciprocity unless properly calibrated for. This issue was discussed in Section 2.3.3. Another qualification to the reciprocity assumption involves the specifics of noise addition to the signal.

Firstly, if the performance is evaluated for a constant received power, the weights applied at the transmitter are equal to the unnormalized weight vector, $\mathrm{w}_u = \mathrm{w}'_u$, found during the forward link, and the equivalent channel at the combiner output is unitary, i.e. $h_{eq} = \mathrm{w}_v^H \mathbf{h}_v$. Therefore, reusing these weights in the forward link implies that the fading process is canceled prior to noise addition. In this circumstance diversity is not applicable and the optimal solution consists in orthogonalizing users without considering the noise added at the receiver branch. Consequently, the unnormalized reuse of weights obtained during the fading reverse link becomes a sub-optimal method.

Secondly, evaluating the weight reuse algorithm for a constant transmit SNR (the weights are reused, but normalized), fading is still present at each user terminal, but with reduced variations in amplitude, as for a diversity receiver. With normalized transmit power, the forward link transfer function between the AP and each UT described in Equation (4.16) is equal to the reverse link transfer function between the UT transmitted signal x_u and the detected signal $\hat{x}_u$ at the AP, and it will be shown in Section 4.1.2 that the performance is identical to the performance of the reverse link. Note that to fully exploit reciprocity, we must respect the conditions in which the reverse and forward link are evaluated. To simplify the performance analysis, we assume the fading channel mean power gain is unitary and consequently the large scale path loss is equal (equal to one) between each access point antenna element and user terminal. During the reverse link, each user terminal transmits with equal power $P_{TX,rvr}$ and at each branch of the AP, the mean received power from one UT is $\mathrm{E}[P_{RX,rvr}] = P_{TX,rvr}$. Similarly, during the forward link, transmitting a total constant power $P_{TX,fwd}$ at the AP antenna array produces at each user terminal a received signal from the AP with mean power $\mathrm{E}[P_{RX,fwd}] = P_{TX,fwd}$. As a consequence, to model the forward and reverse links with the same covariance matrix R, the signal-to noise ratio during forward link must be equal to the signal to noise ratio during reverse link. Assuming each user terminal and the access point all transmit the same power, the noise sources during the reverse and forward link must have an equal average power N_0. This implies that the electronic noise figure characteristics must be similar at the AP and UT. Alternatively if the UT and AP noise figures are $N_{0,UT}$ and $N_{0,AP}$ respectively the AP transmit power must be adjusted such that:

$$P_{TX,fwd} = \frac{P_{TX,rvr}}{N_{0,AP}} \tag{4.20}$$

Zero-Forcing Weight Solution

Rather than re-using MMSE calculated weights from the reverse link to facilitate forward link communication one can simply try to use a different forward weight calculation. As described in [44], using the zero-forcing algorithm, the access point's combiner is used to maximize the signal to interference ratio (SIR), and by definition neglects the presence of noise at each branch (unlike the MMSE algorithm). In this Section, we will see how the weights needed to accomplish this can be calculated using an optimization algorithm, and we will also show how they can alternatively be evaluated using the Wiener-Hopf matrix formulation, as defined in Equation (4.7).

By denoting the user v covariance matrix $\mathbf{R}_v \in C^{M\times M}$ with:

$$\mathbf{R}_v = \mathbf{h}_v\mathbf{h}_v^H, \tag{4.21}$$

and the user v transmit power $P_{TX,v}$ at the AP, the received signal to interference ratio as defined in [44] is:

$$SIR = \frac{P_{TX,v}\mathbf{w}_v^H\mathbf{R}_v\mathbf{w}_v}{\sum_{u=1,u\neq v}^{U}\left(P_{TX,u}\mathbf{w}_u^H\mathbf{R}_v\mathbf{w}_u\right)} \tag{4.22}$$

Also, if we define the total interference covariance matrix for the desired user v as:

$$\mathbf{R}_{int,v} = \sum_{\substack{u=1\\u\neq v}}^{U}\mathbf{h}_u\mathbf{h}_u^H, \tag{4.23}$$

then, the weight vector needed to transfer the highest power to user v while minimizing its presence at the input of all other UTs can be found by solving the optimization problem for $\mathbf{w}_v$ [44]:

$$\hat{\mathbf{w}}_v = \underset{\mathbf{w}_v}{\arg\max}\left(\frac{\mathbf{w}_v^H\mathbf{R}_v\mathbf{w}_v}{\mathbf{w}_v^H\mathbf{R}_{int,v}\mathbf{w}_v}\right). \tag{4.24}$$

This is a generalized eigenvector problem [12] with:

$$\mathbf{R}_v\mathbf{w}_v = \lambda\mathbf{R}_{int,v}\mathbf{w}_v. \tag{4.25}$$

The solution $\mathbf{w}_v$ is the eigenvector associated with the primary eigenvalue $[\lambda]_m = \max(\lambda)$.

Alternatively, one can solve the system using the Wiener-Hopf equation with $N_0 = 0$. Unfortunately, this setting causes the matrix inversion to be singular: it produces more than one solution. To find a unique solution, the system is constrained so that $\mathbf{w}_v^H\mathbf{h}_v = 1$. This indicates that the resulting received signal is constant. The solution is equivalent to the previous method defined by Equation (4.24), and the performance is the same.

Also, whether using the optimization method or the Wiener-Hopf equation (with $N_0 = 0$), the zero-forcing filter for the single-user network offers no solution: the interference covariance matrix $\mathbf{R}_{int,v} = \mathbf{0}$. In this case the precoder becomes a diversity scheme and the weights solve the optimization problem [44]:

$$\hat{\mathbf{w}}_v = \underset{\mathbf{w}_v}{\arg\max} \left(\mathbf{w}_v^H \mathbf{R}_v \mathbf{w}_v\right). \tag{4.26}$$

This method is equivalent to solving the weights by using the Wiener-Hopf method and including the noise N_0 in the covariance matrix. The weights found are equal to the reverse link diversity solution:

$$\mathbf{w}_v = \frac{\mathbf{h}_v}{\|\mathbf{h}_v\|^2}, \tag{4.27}$$

where the denominator is used to preserve an equivalent unitary channel.

Similar to the weight reuse algorithm, in order to send a constant transmit power using the zero-forcing filter, the weights must be normalized using Equation (4.18).

Performance Comparison

In Table 4.1, we present a summary of the performance for all system configurations. The following paragraphs elaborate on the points listed in this Table.

Table 4.1: SDMA Precoder Configuration Performance

	Weight Reuse Solution	Zero-Forcing
Constant Transmit Power	Represents the optimal linear multiuser (MMSE) solution	Removes interference at the expense of noise degradation.
Constant Received Power	Minimal hardware complexity. Suboptimal solution.	Completely removes interference. High transmit power.

Constant Transmit Power Scenario In a first instance we wish to analyze the SDMA precoding scheme for which the transmit power is held constant. A 4-element spatial filter is used at the AP and there are as many as 4 users in the system. The system is analyzed for a Rayleigh channel (for which the user separation is inconsequential), as well as for a Rician channel, with colocated users (i.e. users are situated at separated by 5 degrees relative to the AP) and, secondly, separated users (i.e. users distributed uniformly over a half plane, that is 180 degrees). The forward link performance is shown in Figure 4.7 for SNR_{TX} = 12 dB. For a given channel configuration, the weight reuse algorithm consistently outperforms the zero-forcing equalizer. This is easily explained by noting that the constant transmit power zero-forcing equalizer orthogonalizes users, at the expense of noise deterioration, whereas the weight reuse algorithm (mathematically equal to the MMSE solution), minimizes the signal error at the receiver, and consequently minimizes the presence of noise and interference simultaneously. The difference in performance is only marginal particularly for separated users in a Rician channel. We can attribute this behavior to the fact that the SNR is relatively high and the noise contribution at the receiver is small comparatively to the interference power. Finally it must be noted that as the number of user increases, a greater difference in performance can be observed between the zero-forcing and the weight reuse solution. From this, we can conclude that as the number of users increases, the zero-forcing algorithm separates additional users at the expense of noise deterioration relative to the weight reuse solution.

We can extract similar conclusions from the 2-user BER curves as a function of (transmit) SNR shown in Figure 4.8. Here also, we see that the difference in performance is marginal between the two algorithms for different channel configurations. Particularly in the case of the Rician channel where the two users are separated, the quasi-deterministic (K = 6) channel easily separates users, relieving the burden of the

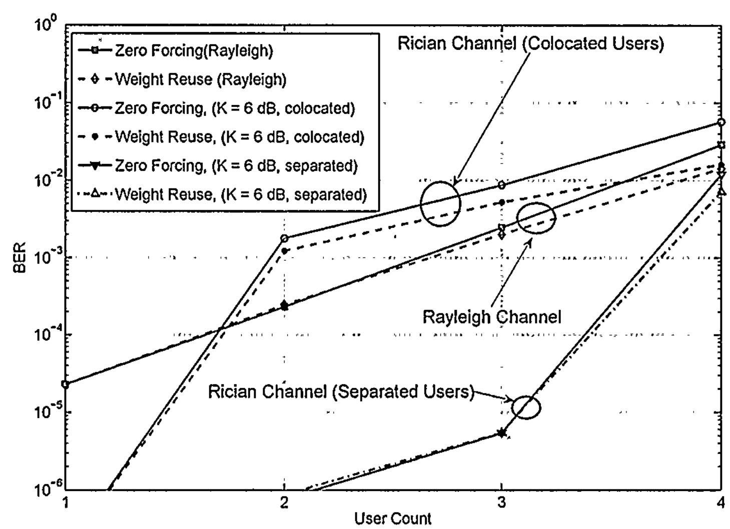

Figure 4.7: Precoder Multiuser BER Performance For SNR_{TX} = 12 dB.

zero-forcing precoder, and therefore minimizing noise deterioration at the receiver.

Constant Received Power Scenario Now, we re-examine our algorithms under the condition that the weights are calculated such that the receive power is held constant. In Figure 4.9, we present the multiuser performance for the zero-forcing spatial filter as well as for the weight reuse algorithm for a receiver SNR = 12 dB. First, we see that the zero-forcing algorithm performance is constant even as the number of users increases. On the other hand, the performance of the re-used MMSE algorithm degrades as the user count increases, particularly for Rician environments in which users are colocated. It is also interesting to note that, under the zero-forcing algorithm, the receiver performance remains constant for different channel conditions and user spatial distributions: the performance in the Rician channel is equal to the performance in the Rayleigh channel no matter the angle separation between users. For an AWGN channel (Rician channel with $\sigma_r = 0$), all channels become perfectly equal, and can only be separated by angle. Without fading or dephasing between

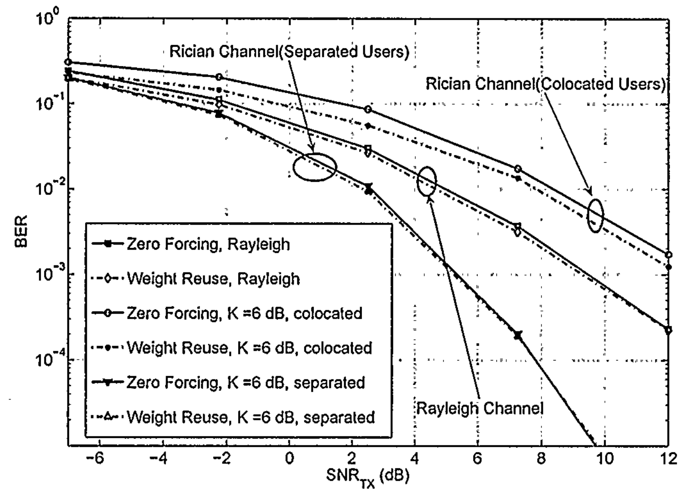

Figure 4.8: Precoder Two-User BER Performance In Presence of Noise For A Constant Transmit Power.

antennas, the zero-forcing algorithm becomes unable to orthogonalize users, causing severe performance degradation. This then, is the one scenario (albeit unrealistic in indoor environment) that the constant transmit power zero-forcing algorithm cannot address.

In Figure 4.10, we show the dependency between receiver SNR and the probability of bit error for two users addressed by the zero-forcing and weight reuse algorithms. Here also, we see that the zero-forcing algorithm performance is equal for all channel configurations and always outperforms the MMSE algorithm. In a Rician channel, the weight reuse algorithm performs better as user separation increases, but cannot attain the performance of the zero-forcing filter.

Also, we present in Figure 4.11 the distribution of transmit power per user in a Rayleigh channel using the zero-forcing algorithm. Assuming the channel as well as front-end gains at the transmitter and receiver are normalized, the total transmit power per user is calculated with:

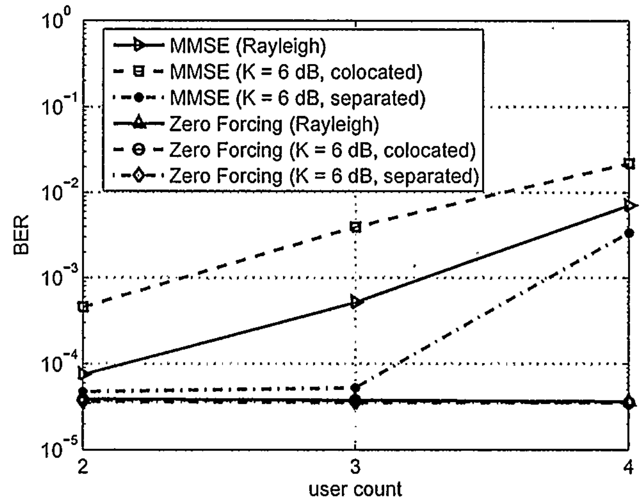

Figure 4.9: Precoder Multiuser BER Performance With SNR_{RX} = 12 dB.

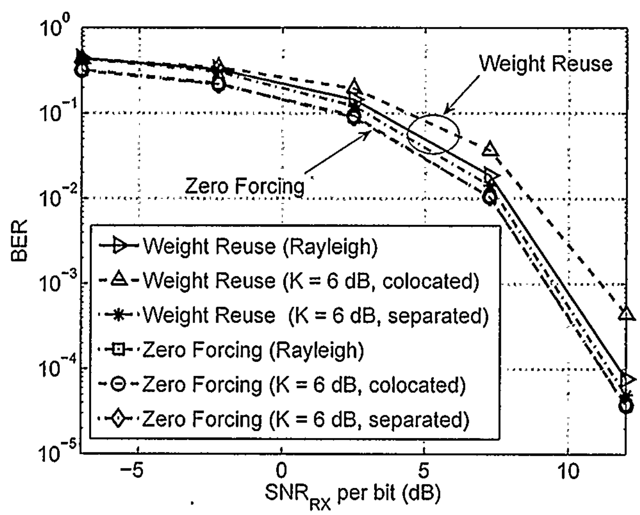

Figure 4.10: Precoder Probability of Bit Error vs. SNR_{RX}.

$$P_{TX,W} = \left(\sum_{u=1}^{U} \mathbf{w}_u^H \mathbf{w}_u \right) / U \tag{4.28}$$

We see from Figure 4.11 that as the user count increases, more power is necessary to orthogonalize each user. In particular, using 4 antennas, broadcasting simultaneously to 4 users requires an impractical amount of transmit power. We see that for 4 users, in a Rayleigh environment, 5% of the time, the calculated weight vector (where weights are calculated for each quasi-static channel) will induce a normalized transmit power per user above 12 dBm. In comparison, to ensure the transmit power is not above a certain threshold for 5% of the time, the minimum transmit power for 3 users is 3 dBm, and for 2 users, it is 0 dBm. These are more reasonable values, but the above characteristics highlight an important limitation to the practicality of the constant receive power zero-forcing algorithm.

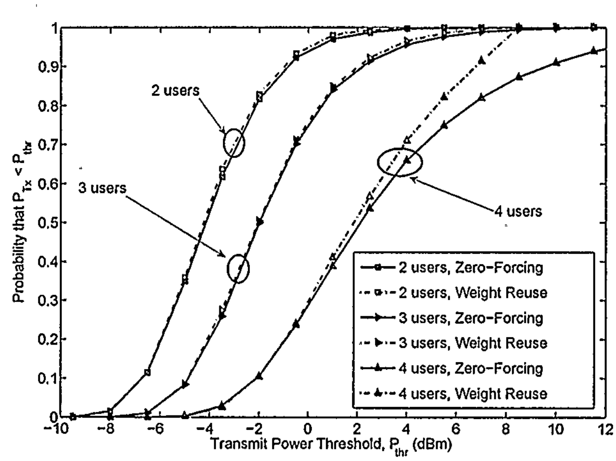

Figure 4.11: Transmit Power Per User Distribution In Rayleigh Channel

In Figure 4.12, we show the same distribution, but for a Rician channel, where $K = 6$ dB. We can see that, when the users are colocated, more power is required, while separated users require less transmit power. Thus, even though the zero-forcing receiver performance is the same for different channel conditions as shown in Figure 4.9, we see that the necessary transmit power required to separate users increases as user angular separation diminishes, particularly as the deterministic component becomes more important.

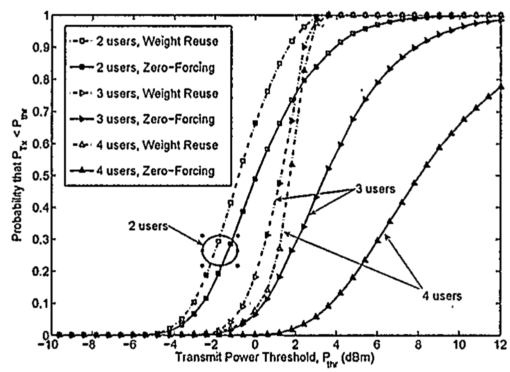

(a) Colocated users

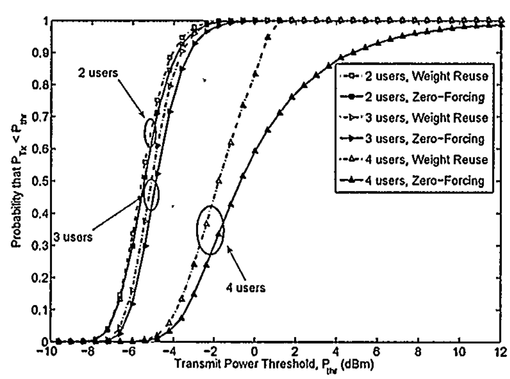

(b) Separated users

Figure 4.12: Transmit Power Per User Distribution In Rician Channel

4.2 Spread Spectrum Technology For Frequency Selective Environments

Spread spectrum technology, as its name implies, spreads the data to be transmitted over a large bandwidth. Direct sequence code division multiple access (DS-CDMA), a spread spectrum technique which multiplies each data symbol with a signature, has been used profusely as a means to increase multiple access performance. The application of the signature serves a dual purpose: it spreads the symbol over a larger bandwidth, and it serves as a mode of identification for each user in a network. For example, as described in [7], the IS-95 standard defines each 1.25-MHz bandwidth channel to be shared among multiple users. During the forward link the data to each user is orthogonalized with a Walsh code resulting in each symbol being spread by a factor of 64. Additionally, the spread signal is superposed with a pilot sequence consisting of 2^{15} chips providing a reference at the user terminals for synchronization and basestation identification. Comparatively, in the reverse link, the spreading code is a long (symbol aperiodic) PN sequence, and the Walsh-modulated data is spread by 4, before being superposed with a pilot PN sequence for synchronization purposes. In another case, the 802.11b standard spreads the modulated signal (in both the reverse and forward link) with an 11-chip Barker code for equalization of the received signal [45] in dispersive channels.

The above examples constitute just a small sampling of the spread-spectrum approaches available in the field. In this project, a main objective is to evaluate the benefit of splicing antenna arrays (and their accompanying spatial processors) with suitable existing multiple access technologies. In the following section, we firstly give a description of a DS-CDMA system, secondly evaluate the importance of the code selected, thirdly, develop a signal model for synchronous and asynchronous links, and finally, give an explanation of different CDMA receiver architectures designed for different conditions. Hence, this Section completes the background necessary to the discussion of our proposed space-time algorithms in Section 4.3.

4.2.1 DS-CDMA General Description

In DS-CDMA, the signal to be transmitted is up-sampled and multiplied with a spreading code c as shown in Figure 4.13. The code is a known random sequence and its signature consists of C chips with binary values $\in \{-1, 1\}$. The code spread factor defines the processing gain (PG), and for a fixed data rate, the resulting bandwidth is spread by PG. Two types of spreading codes may be defined: a short code and a long code. By definition, the short code period is repeated for each symbol, while the long code period spans multiple symbol periods. In this study, we focus our attention on short codes. At the receiver, the correlator shown in Figure 4.14 synchronizes to the beginning of each symbol, multiplies the incoming data with the expected code sequence, and sums the result for each symbol.

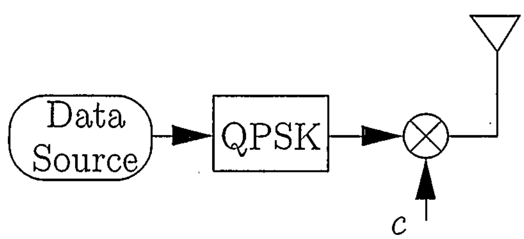

Figure 4.13: CDMA Spreading

In forward link applications, signal reception is synchronous, i.e. the received signal (for the first channel path) at user v consists of superposed sequences intended for different users that are synchronized such that all signatures are aligned. In the reverse link users transmit independently, and the received signal at the AP contains superposed signals arriving asynchronously, i.e. the beginning of the signatures are misaligned. These two cases must be treated differently and to do so the cross-

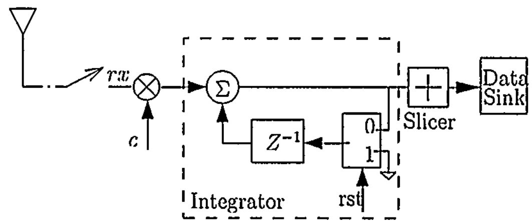

Figure 4.14: Correlator CDMA receiver

correlation between signatures must take into account the delay between signature arrival times. This subject is treated in Section 4.2.2.

Also, hardware constraints, particularly the data converter complexity, as well as the cost of regulated frequency allocation, limit the spread factor. In general, a low spread factor results in signature cross-correlation degradation, particularly in asynchronous channel conditions, leading to degraded multiaccess performance. Additionally, as channels become more dispersive and consequently increase the amount of inter-symbol interference (ISI), CDMA performance degrades because of the imperfect autocorrelation properties in the code. To combat the effect of ISI in CDMA, a RAKE filter may be implemented, but as interference between users increases, more complex structures are required.

4.2.2 Code Selection

Various standard codes are currently used in CDMA technology. For example, the pseudo-random (PN) sequence is generated with a maximum length shift register (MLSR) filter, while the Gold code is simply the combination of two particular PN sequences [9]. The MLSR structure is represented in Figure 4.15 and generates a PN sequence with $C = 2^m - 1$ chips, where m is the number of shift registers. The sequence is generated by summing selected shift register outputs and in the particular case shown in Figure 4.15 can be represented with the polynomial: $h(p) =$

$p^m + p^{m-1} + p^{m-2} + p^1 + 1$. Alternatively, the Walsh code is obtained using the Walsh-Hadamard matrix. Another code studied in this work is the Barker code employed in the 802.11b standard. In order to select the adequate code for a given situation, one must first define the auto-correlation and cross-correlation requirements.

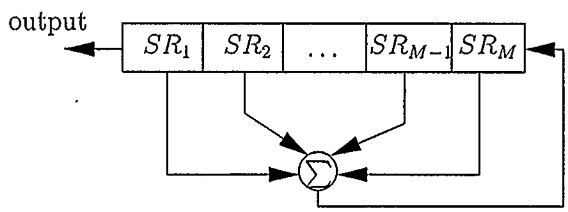

Figure 4.15: Maximal Length Shift Register With Feedback

Auto-correlation describes the resemblance of a signal to delayed versions of itself. Formally, the auto-correlation of a C-chip code $c_x(n)$ is defined with:

$$\rho_x(k) = \frac{1}{C} \sum_{n=0}^{C-|k|-1} c_x(n) c_x^*(n + |k|), \tag{4.29}$$

where k represents the time delay, and n is the chip index $\in 0 \leq n < C$. The auto-correlation result is defined for delays between $[-C, C]$.

We show in Figure 4.16 the auto-correlation results for standard codes. Particularly, in 4.16(a), it can be observed that the Walsh code has very poor auto-correlation properties for different chip delays. In comparison, the 11-chip Barker code, although its code length is rather short, has good autocorrelation properties: off the main path, the mean level of correlation is 5% and never exceeds 10% of the maximum peak. This property makes the code useful in equalizer structures using a relatively short spread. Finally, with a length of 1027 chips, the Gold sequence also obtains good autocorrelation properties: the level of correlation when not synchronized is always below 10% of the maximum peak. As the Gold sequence length shortens, its autocorrelation performance degrades.

(a) 128-Chip Walsh Code

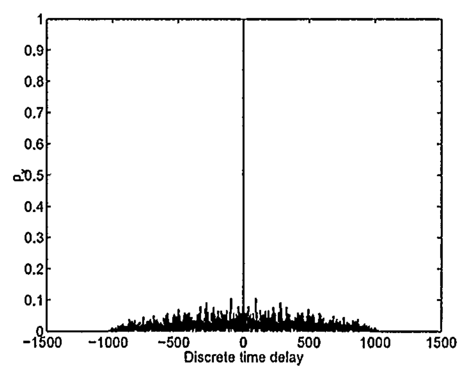

(b) 1023-Chip Gold Code

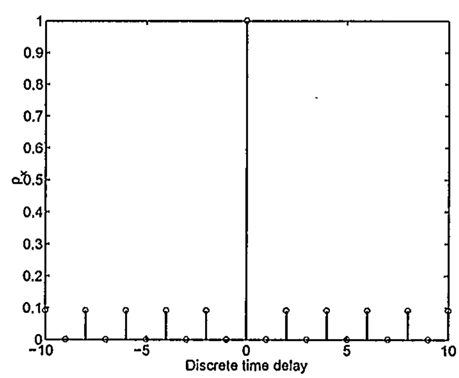

(c) 11-Chip Barker Code

Figure 4.16: Auto-correlation properties of different codes.

Secondly, the cross-correlation function between codes $c_x(n)$ and $c_y(n)$ of equal length C is expressed with:

$$\rho_{xy}(k) = \frac{1}{C}\sum_{n=0}^{C-1} c_x(n)c_y^*(n+k). \tag{4.30}$$

By definition, the codes are limited to a single period, and k represents the relative delay of code $c_y(n)$ in reference to code c_x. For synchronous systems, the cross-correlation at delay $k = 0$ is of particular interest. It becomes:

$$\rho_{xy}(0) = \frac{1}{C}\sum_{n=0}^{C-1} c_x(n)c_y^*(n). \tag{4.31}$$

In asynchronous CDMA the symbol arrivals are not aligned at the AP, and consecutive symbol arrivals must be taken into consideration when calculating the partial code cross-correlation. The time span for the cross-correlation with the reference code c_x is limited to the duration of symbol j. In a multipath channel we define the l_{th} chip delay $\tau_{x,l}$ for code c_x and the l'_{th} chip delay $\tau_{y,l'}$ for code c_y . This scenario is illustrated in Figure 4.17 for $\tau_{y,l'} < \tau_{x,l}$. In this case, a partial cross-correlation is defined at symbol interval j and a second partial correlation is defined at symbol interval $j + 1$. Note that in the situation where $\tau_{y,l'} > \tau_{x,l}$, a partial correlation is defined for interval $j - 1$ and another for j.

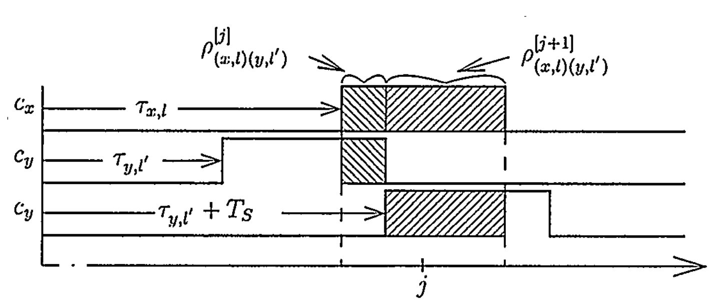

Figure 4.17: Asynchronous cross-correlation for $\tau_{y,l'} < \tau_{x,l}$

We define the relative delay, $\tau = \|\tau_{y,l'} - \tau_{x,l}\|$. If $\tau_{y,l'} > \tau_{x,l}$, the cross-correlations between c_x and c_y are evaluated with:

$$\rho^{[j-1]}_{(x,l)(y,l')} = \sum_{n=0}^{\tau-1} c_x(n)c_y(n + C - \tau), \tag{4.32}$$

$$\rho^{[j]}_{(x,l)(y,l')} = \sum_{n=\tau}^{C} c_x(n)c_y(n - \tau), \tag{4.33}$$

while if $\tau_{y,l'} < \tau_{x,l}$, the cross-correlations between c_x and c_y are:

$$\rho^{[j]}_{(x,l)(y,l')} = \sum_{n=0}^{C-\tau-1} c_x(n)c_y(n + \tau), \tag{4.34}$$

$$\rho^{[j+1]}_{(x,l)(y,l')} = \sum_{n=C-\tau-1}^{C} c_x(n)c_y(n + C - \tau). \tag{4.35}$$

While auto-correlation performance is critical in frequency selective environments, cross-correlation is significant in multiple access networks limited by the user count. For example, a received code c_y with perfect cross-correlation to reference code c_x will be completely eliminated at the output of the filter matched to c_x. Walsh codes present an attractive solution in synchronous systems, because they are orthogonal to each other. For asynchronous systems their performance degrades very rapidly however. In comparison, although their synchronous cross-correlation is imperfect, Gold codes obtain a better cross-correlation performance in asynchronous systems.

4.2.3 System model

In this section, we develop a CDMA system model including interference presence for a dual purpose: a) it will be straightforward to extract the CDMA temporal filter architecture from the model for use in uncoupled space and time processing, and b) it will be possible to efficiently expand it into an optimal space-time model (presented in Section 4.3) combining the SDMA and CDMA techniques. In the CDMA model, the effect of multipath will be considered. Additionally, multiple users with the same modulation scheme but different signatures are made present in a single frequency allocation. In the forward link, the access points transmits simultaneously to all users and we may assume the reception is synchronous (all codes arrive simultaneously), while in the reverse link the reception at the access point from multiple users is asynchronous (the codes arrive with different delays sampled at the chip period).

Forward Link Synchronous Communication

During the forward link, in general, the access point transmits synchronously to U users, where each user has its data spread with c_u. We first describe the simplified model for a synchronous frequency flat channel followed by the model for a frequency selective channel. The model is intended to represent the equivalent mathematical model between the AP and user terminal v.

Frequency Flat Channel Transmitting over a flat fading channel, h_v, produces a received signal:

$$r_v(t) = \sum_{u=1}^{U} h_v c_u(t) x_u(t) + n(t), \tag{4.36}$$

where $n(t)$ represents white Gaussian noise.

In order to describe a multiuser CDMA system, we adopt the notation used by Verdu in [46] for multiple user detection. Although multiple user detection is generally applicable to the reverse link, it proves useful in the modeling of the interference in the forward link as well. Assuming that (at user terminal v) a correlator is implemented for each defined signature c_u, the output of the integrator at time n, $\mathrm{y}_n \in C^{U\times 1}$, is represented in vector form with:

$$\mathrm{y}_n = \mathrm{R}_s \mathrm{H}_{ff} \mathrm{x}_n + \widetilde{\mathrm{n}}, \tag{4.37}$$

where the transmit vector at time n is $\mathrm{x}_n \in C^{U\times 1}$ and is defined as:

$$\mathrm{x}_n = [x_1 \; x_2 \; \cdots \; x_U]^T \tag{4.38}$$

Because the model represents the received signal at user v, all transmitted data is applied to channel h_v, and the flat fading channel matrix is $\mathrm{H}_{ff} = \mathrm{diag}\{h_v \cdots h_v\} \in C^{U\times U}$ and $\mathrm{R}_s \in C^{U\times U}$ is the synchronous cross correlation matrix with elements $[\mathrm{R}_s]_{xy} = \rho_{xy}(0)$ defined with Equation (4.31).

Frequency Selective Channel Unfortunately, in Verdu's work, the fading channel is not explicitly modeled and becomes incomplete for the full scope of our work. In [47], the author explains a useful methodology to model multipath as well as multiaccess in fading channels using a matrix notation for a space-time channel. Because Verdu's mathematical model is more elegant, and can be expressed more easily, the terminology used here is inspired by both publications.

We define the spread spectrum signature to user u c_u. In a frequency selective channel, assuming the multipath channel to user v, path i (where $1 \leq i \leq L$) is expressed with $h_{v,i}$, we define the received signal at user v with:

$$r_v(t) = \sum_{u=1}^{U}\sum_{i=1}^{L} h_{v,i}c_u(t-\tau_i)x_u(t-\tau_i) + n(t). \tag{4.39}$$

As for the frequency flat channel, we denote the transmit symbol vector at time n for all users, $\mathrm{x}_n \in C^{U\times 1}$. The asynchronous multiple user correlation between the U signatures for L path delays at symbol arrival n, $\mathrm{R}_a^{[n]} \in R^{LU\times LU}$ may be represented in matrix form:

$$\mathbf{R}_a^{[n]} = \begin{pmatrix} \rho^{[n]}_{(1,1)(1,1)} & \cdots & \rho^{[n]}_{(1,1)(1,L)} & \cdots & \rho^{[n]}_{(1,1)(U,1)} & \cdots & \rho^{[n]}_{(1,1)(U,L)} \\ \rho^{[n]}_{(1,2)(1,1)} & \cdots & \rho^{[n]}_{(1,2)(1,L)} & \cdots & \rho^{[n]}_{(1,2)(U,1)} & \cdots & \rho^{[n]}_{(1,2)(U,L)} \\ \vdots & \vdots & \vdots & \vdots & \vdots & \vdots & \vdots \\ \rho^{[n]}_{(U,L)(1,1)} & \cdots & \rho^{[n]}_{(U,L)(1,L)} & \cdots & \rho^{[n]}_{(U,L)(U,1)} & \cdots & \rho^{[n]}_{(U,L)(U,L)} \end{pmatrix}, \tag{4.40}$$

where, as defined in Section 4.2.2 (replacing the code length C with the discrete symbol period T_s, and reminding the reader that l represents the l_{th} multipath delay for user x while l' represents the l'_{th} multipath delay for user y), $\rho^{[n]}_{(x,l)(y,l')}$ represents the cross-correlation between the reference signature c_x delayed by l and signature c_y delayed by $l' + n \cdot T_s$. The frequency selective channel matrix between the AP and user terminal v is represented in matrix form, $\mathbf{H}_{fs} \in C^{LU \times U}$ and is defined as:

$$\mathbf{H}_{fs} = \text{diag}(\mathbf{h}_v \ \cdots \ \mathbf{h}_v), \tag{4.41}$$

where each row $(u-1) \cdot L + i$ represents at user terminal v the contribution from transmit signal intended to user u through the path i of the dispersive channel $\mathbf{h}_v$. If we assume the multipath spread spans Δ symbols, the output of the correlators $\mathbf{y}_n \in C^{UL \times 1}$ for all users and all paths at time n is:

$$\mathbf{y}_n = \sum_{k=-\Delta}^{\Delta} \mathbf{R}_a^{[k]} \mathbf{H}_{fs} \mathbf{x}_{n+k} + \widetilde{\mathbf{n}}. \tag{4.42}$$

where $\mathbf{R}_a^{[k]}$ is the asynchronous cross-correlation matrix for delay k and $\widetilde{\mathbf{n}} \in C^{LU \times 1}$ is the equivalent noise vector at the output of the the correlators. In the forward link, we assume that the maximum path delay is smaller than a symbol duration. This assumption is motivated by the data bandwidth expected of our system and a general appreciation for the gross characteristics to expect of our wireless channel. For example, assuming the uncoded symbol rate is 2 MHz, a realistic indoor channel delay spread of $\tau_{RMS} = 60$ nsec will contain non-negligible paths only for a fraction of the symbol period of 500 nsec. Therefore, the multipath spread spans only $\Delta = 1$ symbol. In this situation, it becomes insightful to expand Equation (4.42) to:

$$\mathrm{y}_n = \mathrm{R}_a^{[-1]}\mathrm{H}_{fs}\mathrm{x}_{n-1} + \mathrm{R}_a^{[0]}\mathrm{H}_{fs}\mathrm{x}_n + \mathrm{R}_a^{[1]}\mathrm{H}_{fs}\mathrm{x}_{n+1} + \widetilde{\mathrm{n}}. \qquad (4.43)$$

Note that $\mathrm{R}_a^{[-n]} = \left(\mathrm{R}_a^{[n]}\right)^T$. In [46], Verdu arrives to the same mathematical model between the transmit x_n and the received signal y_n and expresses it using an equivalent discrete Z-domain transfer function $\mathrm{y}(z) = \mathrm{S}(z)\mathrm{H}_{fs}\mathrm{x}(z)$, and in this form, the asynchronous cross-correlation matrix $\mathrm{S}(z) \in R^{LU\times LU}$ becomes:

$$\mathrm{S}(z) = \left(\mathrm{R}_a^{[1]}\right)^T z^{-1} + \mathrm{R}_a^{[0]} + \mathrm{R}_a^{[1]}z, \qquad (4.44)$$

where the notation Gz^{-k} denotes a delay by k symbols of the input vector $\mathrm{x}(z) \in C^{U\times 1}$ followed with a multiplication by G.

Note that in the forward link, this complete model is somewhat unrealistic if intended for a direct hardware implementation because this requires each mobile to implement a correlator for all known signatures in the network, and in general the user terminal not only ignores the signatures of other users, but is also constrained by its hardware complexity. Nonetheless, the above model can still prove itself useful in the simulation of multipath channels as well as partial multiuser detection (for which the number of correlators implemented for detection of the desired user is limited).

Reverse Link Asynchronous Communication

In general, during the forward link, DS-CDMA is synchronous, i.e. the codes arriving at the user terminal are time aligned. Only multipath arrivals are asynchronous. In the reverse link, users transmit to the access point without prior knowledge of precise timing with other users. Additionally, each signal is transmitted through a different channel, with different time delays. Under such circumstances, it becomes very difficult to synchronize all transmitters such that all signals arrive at the access point synchronously.

Nonetheless, it is possible to adequately model the reverse link using the same notation as described above for synchronous multipath communication links. We must keep in mind that in the reverse link, all signals propagate through different channels. Applied in a multipath channel, the output of the correlators can still be modeled with Equation (4.42). The channel matrix defined in Equation (4.41) must be modified to take into account the fact that multiple users transmit to the access point through different multipath channels, and becomes:

$$\mathbf{H}_{fs} = \mathrm{diag}(\mathbf{h}_1 \ \cdots \ \mathbf{h}_U). \tag{4.45}$$

Using the system model developed, it is now possible to efficiently simulate the architecture of CDMA receivers and in particular to evaluate their performance in the presence of interference.

4.2.4 Receiver Architectures In Frequency Selective Channels

In a single user network for which the channel is ideal (AWGN), the CDMA matched filter, which is shown in Figure 4.14, provides processing gain (PG) equal to the length of the signature. In a typical receiver, a sliding window correlator will synchronize the beginning of the signature sequence with the received signal and provide a channel estimation prior to matched filtering. The minimum clock rate at this stage is the chip rate. For more precise channel estimation (including time delay), the clock may be upsampled. Once the received signal is aligned with the locally generated signature, it is multiplied at the chip rate by the appropriate spreading code or signature. Because the chips are binary, the signature can be represented on a single bit. At the start of each symbol, the integrator is reset and adds the result of each multiplication together. The symbol emerging from the integrator comes out at the symbol rate, that is, it is downsampled by PG with respect to the correlator's input. Assuming the received signal contains a phase error ϕ the integrator output must be cophased (complex multiplication with $-\phi$) before being decoded with a traditional PSK slicer. Alternatively when the signal is differential encoded, cophasing is unnecessary at the cost of a 3-dB loss in BER performance. Note that the correlator is (once synchronized) a real-time receiver.

The correlator is the fundamental building block in CDMA receivers and as the signal becomes more corrupted with interference this component must be upgraded. In this project, the different sources of interference studied are the Gaussian (noise limited environment), the inband interference (multiple users with different signatures) and the time dispersive property of the channel (multipath interference).

In Section 4.2.2, the correlation properties of the chosen codes are described. It will be shown that imperfect correlation properties influence the performance of the CDMA communication link and in this Section, we will show different receiver architectures for channels corrupted by different sources of interference.

We will describe firstly the optimal receiver for dispersive, noise limited environments (induced by perfect signature correlation performance), followed by a receiver for interference limited environments, in which the interference is due to other users spread with signatures with poor cross-correlation properties. Finally, we will show a possible CDMA filter architecture minimizing noise and interference at the decoder input.

RAKE Receiver: Noise Limited Channel

Using the multiuser model presented in the previous section, in the noise limited environment, correlators are implemented uniquely for the L_F path arrivals belonging to the desired user: the effect of the interference belonging to other signatures is considered negligible, a valid assumption when the signatures have low cross-correlation for the specific timing requirements.

Similar to the spatial maximal ratio combiner discussed in Section 4.1, the L_F-branch combining algorithm maximizes the signal-to-noise-ratio at the output of the combiner by weighting the output of each correlator y_i with $h^*_{v,i}$ where h_i is the amplitude of the wireless channel at multipath delay i. This structure is called the RAKE filter and is shown in Figure 4.18 for user terminal v.

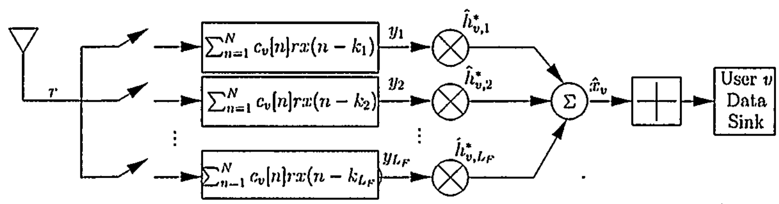

Figure 4.18: RAKE Receiver Block Diagram

Ideally, a correlator is synchronized to each path arrival. The synchronization is facilitated by a channel estimation algorithm searching for the L_F greatest path amplitudes. As explained in [48], low pass filtering with a cutoff frequency of F_C limits the bandwidth of the received signal and effectively correlates (and smears) path arrivals separated by less then $1/F_C$. Because of this, the detected paths are separated by a minimum of one chip period. Also, because the multipath profile is decaying, latter path arrivals become negligible. In order to implement an efficient RAKE receiver, it is necessary to use the optimum number of correlators; increasing this count improves diversity gain at the cost of hardware complexity which includes increased power and silicon area consumption.

To explain diversity gain obtained in a RAKE receiver, in Figure 4.19, we show the distribution of SNR gain for a multipath channel modeled with an exponentially decaying power profile. Each channel path amplitude is modeled with a Rayleigh fading process. Data is spread with a 512-chip Gold code and is transmitted at 16 Mcps. We show the performance for a 3-finger and a 4-finger RAKE filter and for different channel RMS delay spread, τ_{RMS}. It can be observed that for a $\tau_{RMS} = 59$ nsec, the 4-finger RAKE receiver SNR gain is greater, but as the frequency selectivity (i.e. the spread) decreases the additional finger benefit becomes negligible. At $\tau_{RMS} =$ 19.4 nsec, a 3-finger RAKE filter obtains the same diversity gain as the 4-finger RAKE receiver.

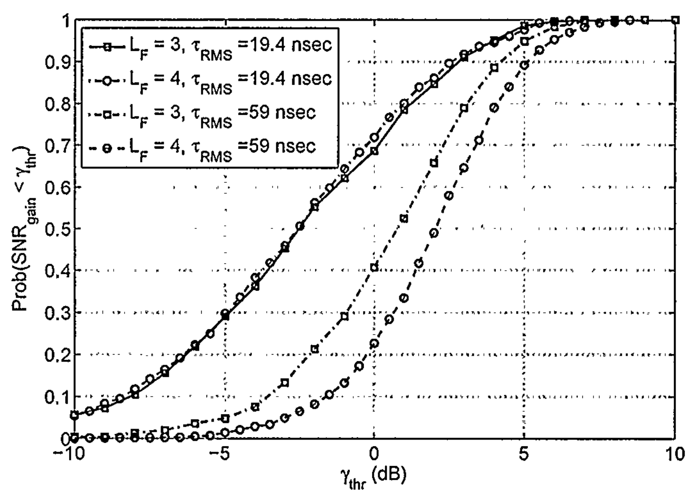

Figure 4.19: SNR Gain Distribution For Gold Code.

Also, in Figure 4.20, we compare the diversity gain using the 11-chip Barker code with the 512-chip Gold code using a 4-finger RAKE receiver for various channel delay spreads. Both codes are sampled at 16 Mcps. Note that this sets the data rate to 1.45 Mbps and 31.25 kbps for the Barker code and Gold code respectively. We can see that for any SNR gain threshold, the probability that the SNR gain is smaller than the threshold γ_{thr} is greater using the Barker code than that for the Gold code. In other words, the 512-chip Gold code diversity performance is better than the Barker code. This is due to the fact that the Barker code auto-correlation performance is poorer than the Gold code sequence, a behavior which is due in part to its much shorter code length. Despite this performance loss, the Barker code remains attractive because, for a constant channel bandwidth (16 Mcps), the symbol rate is much greater (1.45 Mbps) than using a Gold code (31.25 kbps).

As explained earlier, the Walsh code as well as short Gold codes exhibit very poor auto-correlation properties in multipath environments. Using such codes will provide very little diversity gain leaving the RAKE receiver essentially useless. More sophisticated receivers must be implemented even for single user communication.

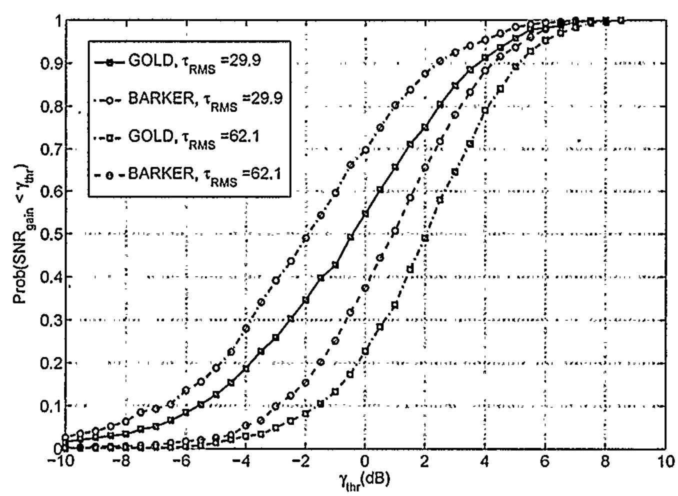

Figure 4.20: Comparison of SNR Gain Distribution For Gold And Barker Code.

Decorrelating Detector: Interference Limited Channel

In [46], the author describes the decorrelator structure for multiuser detection. This filter removes known interference and considers multipath as simply another source of interference. This property requires that a correlator be implemented for the L_F non-negligible path arrivals of the U known signatures. The output of the correlators is represented with the vector y $\in C^{L_F U \times 1}$, and using notation described in Section 4.2.3

for multipath, multiuser CDMA systems, the output of the correlators are combined by applying the linear transform:

$$\mathrm{H}_{fs}^{H}\mathrm{S}(z)^{-1} = \mathrm{H}_{fs}^{H} \cdot \frac{1}{\det \mathrm{S}(z)} \cdot \mathrm{adj}(\mathrm{S}(z)). \tag{4.46}$$

The output becomes:

$$\hat{\mathrm{x}}_n = \mathrm{H}_{fs}^{H}\mathrm{S}(z)^{-1}\mathrm{r} + \mathrm{n}' = \mathrm{H}_{fs}^{H}\mathrm{S}(z)^{-1}\mathrm{S}(z)\mathrm{H}_{fs}\mathrm{x}_n + \mathrm{n}' = \mathrm{H}_{fs}^{H}\mathrm{H}_{fs}\mathrm{x}_n + \mathrm{n}', \tag{4.47}$$

where the noise vector $\mathrm{n}' \in C^{U\times 1}$ is the equivalent noise at the output of the combiner. The matrix $\mathrm{H}_{fs} \in C^{L_F U \times U}$ represents the multiple user frequency selective channel response, and the application of H_{fs}^{H} represents a maximal ratio combiner at the output of the signature decorrelation. This modified decorrelator architecture is represented in Figure 4.21. To simplify the figure, only the detection of the first user is shown, but this type of receiver can simultaneously process parallel data streams from different users.

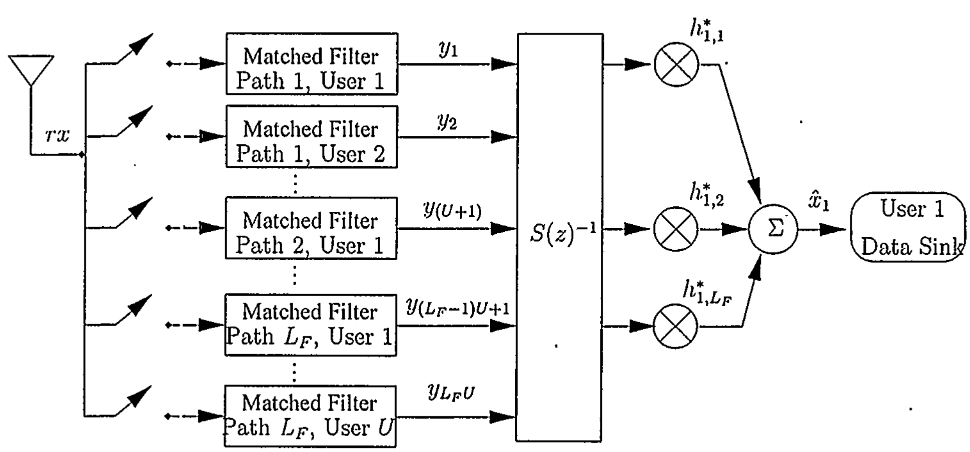

Figure 4.21: The Asynchronous Decorrelator With Diversity Improvement.

The decorrelator is often seen as an impractical filter because the time dependent matrix inversion is computationally intensive. For U known signatures, and L_F implemented correlators for each signature, a $L_FU \times L_FU$ time dependent matrix must be inverted. As shown in Equation (4.46), the inversion of $\mathrm{S}(z)$ can be separated into two sequential filtering stages. First, the determinant in the denominator is a non causal infinite impulse response (IIR) filter. For real-time applications, the IIR filter must be truncated to a reasonable number of taps. Additionally, it was shown in [49] that for certain conditions, there is no solution to the matrix inversion. This is due to the fact that the IIR poles are situated on the unitary circle, a source of instability [50]. To prevent this situation, the code must be selected with caution, and matrix inversion must be evaluated for all possible code correlator delays for a given application. Secondly, the adjoint matrix can be represented with a combination of finite impulse response (FIR) filter outputs at each code correlator branch. Note that the number of taps for each FIR filter is dependent on the number of correlators, while the coefficients of each FIR filter are dependent on the asynchronous cross-correlations (Equations (4.33) and (4.35)). As explained in [51], the values can be calculated for each multipath multi-signature conditions, or can be read from tables.

In a situation where the receiver detects a single user, for example at a user terminal, the matrix inversion is partial. In order to remove all unwanted interference from the output of the correlator for path 1 to user v, mathematically, the row $(v-1)L_F+1$ of the matrix $\mathrm{S}(z)$ is evaluated. In this case, the hardware complexity is reduced. This is shown in Figure 4.22.

The detector considered in this Section, like the zero-forcing equalizer which it resembles, maximizes SIR, but neglects the noise contribution. This causes the decorrelator to behave very poorly in the presence of noise.

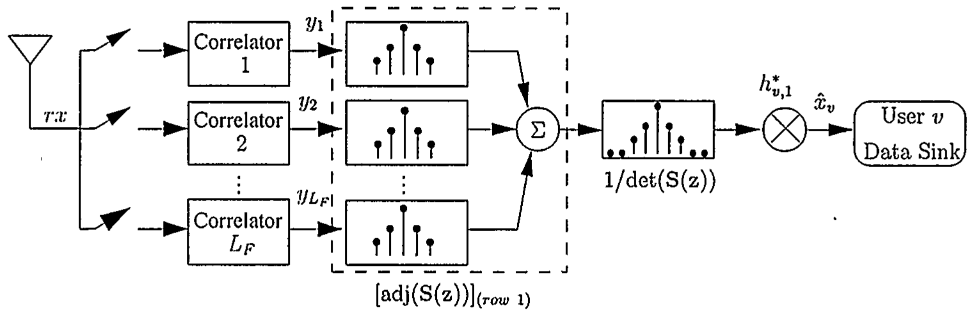

Figure 4.22: Hardware Structure Of The Single-User Multipath Decorrelator.

MMSE Detector: Multiuser Noisy Channel

In [52], Bottomley describes the architecture of a modified RAKE receiver optimized for simultaneous noise and interference minimization. Among other conclusions, he notes that an increased finger count is necessary to implement the generalized RAKE (G-RAKE) receiver (removing noise and interference) relative to the RAKE receiver for the noise limited environment. Following the author's demonstration, it is easy to recognize that the G-RAKE receiver is a specific MMSE filter for forward link applications.

The model described in Equation (4.42) defines the correlator output vector $\mathrm{y} \in C^{LU\times 1}$ and we recall that the receiver processing is implemented at the output of the correlators as described in Section 4.2.3. Using the model described in the previous section, and following the demonstration in [47], we can prove that the sufficient statistic $\varsigma \in C^{U\times 1}$ is:

$$\varsigma = \mathbf{H}_{fs}^{H}\mathrm{y}(n). \tag{4.48}$$

By definition, the sufficient statistic ς contains all the necessary information to further estimate and detect the data frame. The multiplication of the correlator vector output $\mathrm{y}(n)$ with H_{fs}^{H} is a maximal ratio combiner where, for each user, all paths are weighted and summed. In contrast to the multipath decorrelating detector outlined in the previous sub-section, the MRC is applied before the interference cancellation. In a single user environment, the sufficient statistic ς represents the output of a RAKE receiver, while in multiple user detection, the sufficient statistic ς serves as the input to more advanced receiver architectures. The equivalent spread spectrum linear transform $\mathbf{H}_{ss}^{[n]} \in C^{U \times U}$ between the transmit vector and sufficient statistic at time n becomes:

$$\mathbf{H}_{ss}^{[n]} = \mathbf{H}_{fs}^{H} \mathbf{R}^{[n]} \mathbf{H}_{fs}. \tag{4.49}$$

The model in Equation (4.42) can be expanded to account for consecutive symbol arrivals. At time n, we define the transmit vector $\mathbf{x}_n \in C^{U \times 1}$ and if N consecutive symbols are transmitted we then define the vector $\mathbf{x} \in C^{NU \times 1}$ such that:

$$\mathbf{x} = [\mathbf{x}_1^T \ \mathbf{x}_2^T \ \cdots \mathbf{x}_N^T]^T. \tag{4.50}$$

Also, the equivalent time varying channel matrix $\mathbf{H} \in C^{NU \times NU}$ is:

$$\mathbf{H} = \begin{pmatrix} \mathbf{H}_{ss}^{[0]} & \mathbf{H}_{ss}^{[1]} & \cdots & \mathbf{H}_{ss}^{[\Delta]} & & & \\ \mathbf{H}_{ss}^{[-1]} & \mathbf{H}_{ss}^{[0]} & \mathbf{H}_{ss}^{[1]} & \cdots & \mathbf{H}_{ss}^{[\Delta]} & & \\ & \mathbf{H}_{ss}^{[-\Delta]} & \cdots & \mathbf{H}_{ss}^{[0]} & \cdots & \mathbf{H}_{ss}^{[\Delta]} & \\ & & \mathbf{H}_{ss}^{[-\Delta]} & \cdots & \mathbf{H}_{ss}^{[-1]} & \mathbf{H}_{ss}^{[0]} & \mathbf{H}_{ss}^{[1]} \\ & & & \mathbf{H}_{ss}^{[-\Delta]} & \cdots & \mathbf{H}_{ss}^{[-1]} & \mathbf{H}_{ss}^{[0]} \end{pmatrix}. \tag{4.51}$$

The output $\mathbf{y} \in C^{UN \times 1}$ is defined as $\mathbf{y} = [\mathbf{y}_1^T \ \cdots \ \mathbf{y}_N^T]^T$. Then:

$$\mathbf{y} = \mathbf{H}\mathbf{x} + \widetilde{\mathbf{n}}. \tag{4.52}$$

In [47], the MMSE problem is described with:

$$\hat{\mathbf{W}}_M \underset{\mathbf{W}_M \in R^{L_F U \times L_F U}}{\arg\min} \mathrm{E}[\|\mathbf{x} - \mathbf{W}_M \mathbf{y}\|^2], \tag{4.53}$$

and the weight matrix $\mathbf{W}_M \in C^{NU \times NU}$ solving this optimization problem is:

$$\mathbf{W}_M = (\mathbf{H} + \sigma^2 \mathbf{I})^{-1}. \tag{4.54}$$

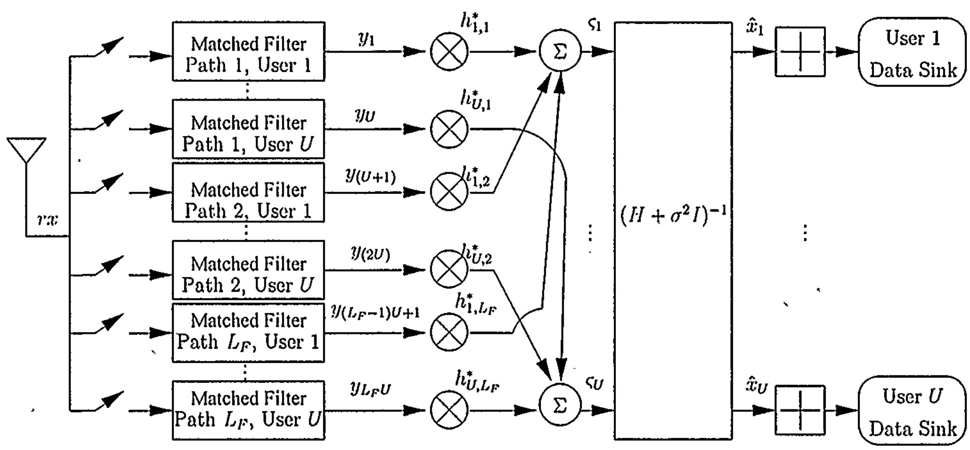

Figure 4.23: MMSE CDMA Receiver.

Because the dimensions of the $\mathbf{W}_M$ matrix depend on the number of users U as well as the number of symbols N, the matrix inversion is computationally intensive, but can be solved using an adaptive algorithm. In particular, we can find the optimal weight vector $\mathbf{W}_M|_v$ at row v for user v by implementing a UN-tap least mean square (LMS) algorithm, for example. The user v transmitted signal sequence must be known, and serves as a reference in the adaptive algorithm. The same procedure should be repeated in parallel for each desired user.

4.3 Space-Time Processing For Multiple Access

Having presented space processing and CDMA processing independently, we now explore the possibility of implementing a space-time algorithm for multiuser access. Obviously, the addition of multiple antennas requires a greater power consumption, as well as increased complexity in architecture. Nonetheless, the communication performance gain is appreciable, and suboptimal or iterative methods can be considered for implementation on the physical layer.

4.3.1 Single User Detection

In [34], the authors describe a complete system which consists of a RAKE receiver enhanced with an antenna array. The channel is fading and dispersive. If we assume code auto-correlation is perfect, in a single user network, the optimal receiver in the presence of noise is the space-time maximal ratio combiner (MRC). This type of combiner can be separated in two main components. First, a spatial filter processes the received signal vector present at the antenna array for each non-negligible path delay. Secondly, the result of the spatial filter at each path delay is combined using a RAKE receiver structure.

Note that in [53], a similar system with reduced complexity is developed: the weight vector for the unique maximal ratio combiner is $\mathbf{w}^* = \mathbf{h}_1^*$ and is maximal for the first path. The unique output of the spatial combiner is applied to the RAKE receiver shown in Figure 4.18. This configuration minimizes hardware complexity, at the cost of reduced theoretical performance. As the channel becomes more dispersive, the performance degrades, because the contribution of the suboptimal paths beyond the main paths will increase at the output of the RAKE receiver.

In [10], such a system consisting of a single beamformer used in conjunction with a CDMA RAKE receiver is implemented in CMOS technology. It is intended for a

W-CDMA reverse link receiver and its bandwidth is 5 MHz. The receiver consists of a 4-element array, and the block diagram of the digital processor is shown in Figure 4.24. Also, the receiver behavioral model defines two states: a preamble detection state, and a data decoding state.

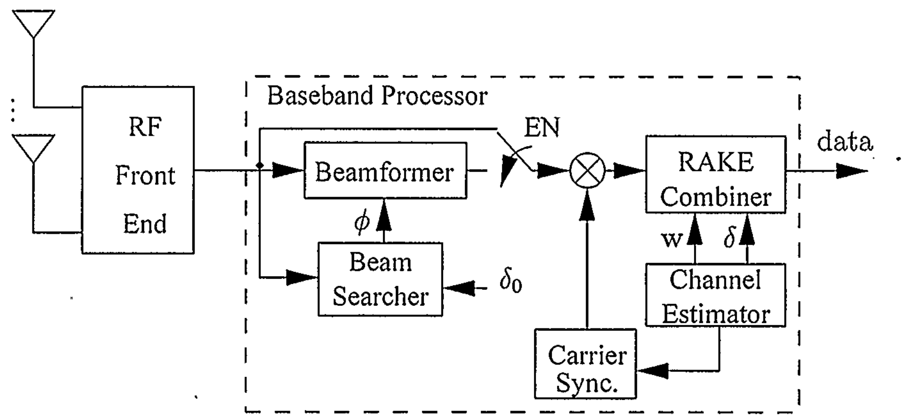

Figure 4.24: Single User Space-Time Receiver Block Diagram.

During the preamble state, the channel estimator block has a dual responsibility: first, it must synchronize with the user signature and, secondly it must determine 4 non-negligible path arrivals as well as their respective amplitude. Note that a single antenna is used as the input to the channel estimator during the preamble state and it is assumed that the temporal dispersive profile is similar at all branches. The result is used by the RAKE combiner in the detection state. Also, the beamformer is intended to change the directivity of the antenna array in a single user environment. To achieve this, the M-element beamsearcher must, during the preamble state, find the optimum weights $\phi \in C^{M\times 1}$ by averaging the output of all four correlators at each antenna branch. As defined in beamforming theory, the weights change the phase of each branch, without modifying the amplitude. Therefore, the combined dispersive profile is maintained at the input of the RAKE receiver, and the weights found for a single antenna can also be applied at the input of the spatial filter. Note that if the resulting dominant path is in a deep fade, the beamformer is disabled, and the output from a single antenna is fed to the next block. Finally, the carrier synchronization block employs a phase lock loop to realize phase and frequency synchronization.

This type of receiver can function well in a deterministic frequency selective channel. For Rayleigh fading channels, deep fades cannot be compensated by a beamforming algorithm and instead an MRC filter is necessary. Also, the Rayleigh channel dispersive profile is not constant for all branches, and a more sophisticated channel estimation algorithm is necessary to find the optimal weights at the output of the spatial filter. To obtain optimal performance, a beamformer and beamsearcher block will need to be implemented for each defined multipath arrival. In this situation, the performance upgrade comes at the expense of greater hardware complexity.

4.3.2 Multiple User Detection For Reverse Link

The combination of CDMA with SDMA can lead to multiple access performance increase. In general, it is reasonable to use antenna arrays at the access point for which the hardware dimensions as well as power consumption constraints are more relaxed.

Here we will show how simultaneous space-time processing can be used on the reverse link to increase communication performance. We limit our study to linear processing. We shall explain the space-time multiuser model as demonstrated in [47]. During the reverse link, the access point receives data from multiple users present in the indoor environment. Here, we assume that each user is assigned a CDMA signature that will be used to spread the DQPSK data. In the reverse link, the data arrives at the access point asynchronously, whose responsibility it is to synchronize with each desired user individually before further data detection. Similarly to the CDMA multiple user detection receiver presented in Section 4.2.4, the received signal at each antenna serves as the input to a vector of correlators for each known user, and each non-negligible path arrival. This is shown in Figure 4.25.

For the purpose of modeling a space-time system, the multipath spatial channel $\mathbf{h}_v \in C^{M\times 1}$ between user v and the access point is defined as:

$$\mathbf{h}_v = \sum_{l=1}^{L} \alpha_{v,l} g_{v,l} \delta(t - \tau_{v,l}), \tag{4.55}$$

where $g_{v,l}$ is the amplitude of the dispersive channel at delay l, and $\alpha_{v,l} \in C^{M\times 1}$ represents the array response vector, or alternatively in a fading channel represents the spatial channel amplitude, and is modeled with a random process with variance σ_r as explained in Chapter 3.

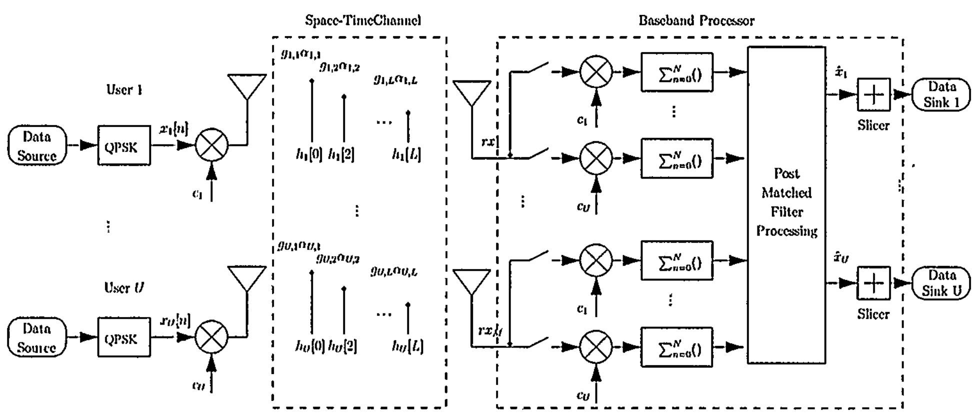

Figure 4.25: Multiple user Space-Time Channel.

In [47], the authors demonstrate that the sufficient statistic to estimate the transmit data consists, for each user v, in applying the output of the user v correlators firstly, to a spatial MRC filter for each defined path delay, and secondly, to a RAKE combiner. The spatial MRC filter weights for user v and path l are equal to the channel fading amplitudes $\alpha_{v,l}$ while the RAKE combiner weights are equal to $[g_{v,1} \cdots g_{v,L}]$. Alternatively, the combining can be processed in a single step where the outputs of each user v correlators at antenna element m and path l is applied the weight $g_{v,l}[\alpha_{v,l}]_m$, where $[\alpha_{v,l}]_m$ is the fading channel amplitude at antenna element m.

Respecting the terminology in Section 4.2.3, the transmit sequence $\mathrm{x}_n \in C^{U\times 1}$ at time n is:

$$\mathrm{x}_n = [x_1\ x_2\ \cdots\ x_U]^T, \tag{4.56}$$

and the signature asynchronous cross-correlation matrix $\mathrm{R}_a^{[n]}$ is defined in Equation (4.40).

We define the multipath channel to user v as $\mathrm{g}_v = [g_{v,1}\ g_{v,2}\ \cdots\ g_{v,L}]^T$ from which we also express the multiuser dispersive channel $\mathrm{G}_{fs} \in C^{LU\times U}$ in matrix notation as:

$$\mathrm{G}_{fs} = \mathrm{diag}(\mathrm{g}_1\ \cdots\ \mathrm{g}_U), \tag{4.57}$$

while the fading variation $\Phi \in C^{M\times UL}$ is also expressed in matrix form as:

$$\Phi = [\alpha_{1,1}\ \cdots\ \alpha_{1,L}\ \cdots\ \alpha_{U,1}\ \cdots\ \alpha_{U,L}]. \tag{4.58}$$

The sufficient statistic $\mathrm{y}_n(n) \in C^{U\times 1}$ becomes ([47]):

$$\begin{aligned} \mathrm{y}_n(n) &= \textstyle\sum_{k=-\Delta}^{\Delta} \mathrm{G}_{fs}^H[\mathrm{R}_a^{[k]} \circ \Phi^H\Phi]\mathrm{G}_{fs}\mathrm{x}_n(n+k) + \tilde{\mathrm{n}} \\ &= \textstyle\sum_{k=-\Delta}^{\Delta} \mathrm{H}_{st}^{[k]}\mathrm{x}_n(n+k) + \tilde{\mathrm{n}}, \end{aligned} \tag{4.59}$$

where the $\circ$ operator denotes element-wise multiplication. The sufficient statistic at the output of the correlators is represented in Figure 4.26 for user v. It is assumed that a correlator is implemented for delay arrivals between $[1, L_F]$ where the signal is sampled at the chip rate. The same architecture must be repeated for each user.

Furthermore, the notation can be expanded to account for N successive symbols. We define $\mathrm{x} \in C^{UN\times 1}$ as:

$$\mathrm{x} = [\mathrm{x}_1\ \mathrm{x}_2\ \cdots\ \mathrm{x}_N]^T, \tag{4.60}$$

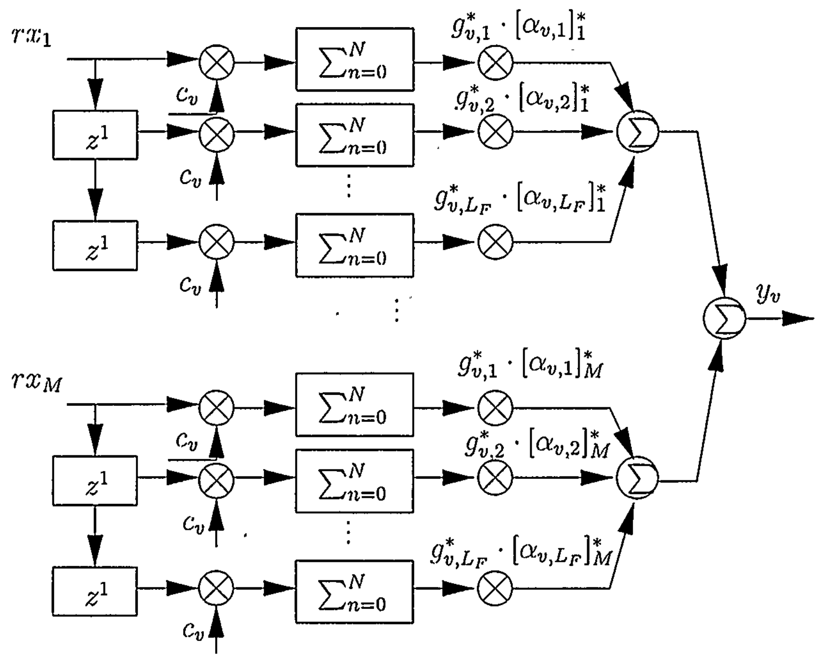

Figure 4.26: Sufficient statistic processing for one user.

and the equivalent multiuser linear transform $\mathbf{H} \in C^{UN\times UN}$ between the transmit vector $\mathbf{x}$ and the sufficient statistic $\mathbf{y} \in C^{UN\times 1}$ is:

$$\mathbf{H} = \begin{pmatrix} \mathbf{H}_{st}^{[0]} & \mathbf{H}_{st}^{[1]} & \cdots & \mathbf{H}_{st}^{[\Delta]} & & & \\ \mathbf{H}_{st}^{[-1]} & \mathbf{H}_{st}^{[0]} & \mathbf{H}_{st}^{[1]} & \cdots & \mathbf{H}_{st}^{[\Delta]} & & \\ & \mathbf{H}_{st}^{[-\Delta]} & \cdots & \mathbf{H}_{st}^{[0]} & \cdots & \mathbf{H}_{st}^{[\Delta]} & \\ & & \mathbf{H}_{st}^{[-\Delta]} & \cdots & \mathbf{H}_{st}^{[-1]} & \mathbf{H}_{st}^{[0]} & \mathbf{H}_{st}^{[1]} \\ & & & \mathbf{H}_{st}^{[-\Delta]} & \cdots & \mathbf{H}_{st}^{[-1]} & \mathbf{H}_{st}^{[0]} \end{pmatrix}, \tag{4.61}$$

and:

$$\mathbf{y} = \mathbf{H}\mathbf{x} + \tilde{\mathbf{n}}. \tag{4.62}$$

In order to obtain a better estimation of the transmitted data $\hat{\mathbf{x}}$, a linear transformation, represented with the matrix $\mathbf{W} \in C^{MU\times MU}$, is applied at the output of the sufficient statistic. If the decorrelator is implemented, the interference is removed, at the expense of noise and the weight matrix $\mathbf{W}_{dec}$ is:

$$\mathbf{W}_{dec} = \mathbf{H}^{-1}. \tag{4.63}$$

Alternatively, the MMSE minimizes the error between the transmit vector and the output of the correlators. In this case, the weight matrix is:

$$\mathbf{W}_{mmse} = (\mathbf{H} + \sigma \cdot \mathbf{I})^{-1}. \tag{4.64}$$

Because the dimension of $\mathbf{H}$ (the dimension is proportional to the symbol count in the window, as well as the known user count in the network) is usually relatively large, matrix inversion is computationally intensive.

4.3.3 Multiple User Transmission For Forward Link

In this work, we wish to develop a multiple access scheme, building an access point that not only receives simultaneously from spatially separated users, but can also transmit simultaneously to the same users. In Section 4.1, we showed a spatial architecture using solely SDMA for downlink transmission. Combining SDMA with spread spectrum technology, it is possible to increase the multiple access performance, and additionally, in a fading dispersive environment, benefit from time diversity.

In [54], a space-time algorithm is shown and weights are applied such that the transmit signal for user v, $\mathrm{s}_v \in C^{M\times 1}$, becomes:

$$\mathrm{s}_v = \sum_{i=1}^{L_F} \mathrm{w}_{v,i}^{*} x_u(t + (i - L_F + 1)T_s), \tag{4.65}$$

where T_s is the sampling period, and the signal is delayed by $(L_F - 1)T_s$ to ensure causality. The author explains how the precoding scheme consists of a pre-RAKE architecture ([55] and [56]) for each antenna branch. By definition, the pre-RAKE combiner multiplies the transmit sequence by the time inverse of the channel impulse response complex conjugate. Using the method described in the cited work, the weights calculated should minimize the transmit power while assuring that the SINR at the receiver is greater than a defined threshold.

In the present work, we use a linear multiuser detection algorithm to find optimal weights, and the approach taken during the forward link is to apply the same linear transform at the AP transmitter as on the receiver. Note that in the forward link the order of operations is reversed compared to the reverse link. Also the transmit sequence at the antenna array input must be normalized to transmit a constant power. Using this access point architecture, each mobile unit can be limited to a single correlator. The resulting transmitter architecture for a single user is represented in Figure 4.27. For multiple user precoding, at each antenna, the outputs of the pre-

RAKE filters for each user u must be summed together.

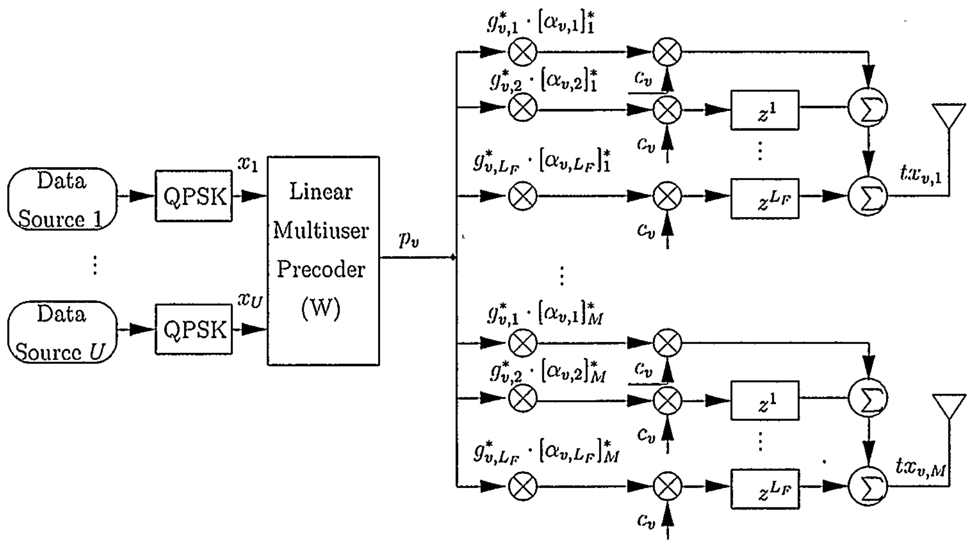

Figure 4.27: Multiuser Space-Time Precoding Architecture for One User.

The reverse link is subject to asynchronous reception, while the forward link is not. Using multiple CDMA codes, the cross-correlation properties are different in the forward and reverse link, and this results in different equivalent mathematical models. Although the architecture is designed to maintain reciprocity, weights must be recalculated for the forward link. Also, as explained in [56], the pre-RAKE performance is poorer than the RAKE performance on the receiver, and we should expect a degradation of performance when using the above method to compute precoding weights.

In Figure 4.28 we show the pre-RAKE bit error rate performance as simulated in Matlab for a space-time precoding algorithm. The transmit power is held constant and an MMSE filter is applied. The antenna array consists of 12 elements and 8-chip Walsh codes are being used. The CDMA codes are reused among spatially separated users. It can be seen that spatially separated users in a Rician channel obtain the

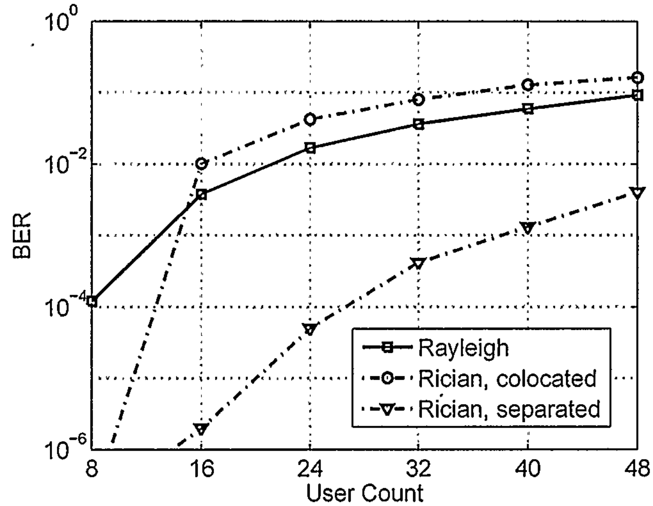

Figure 4.28: Pre-Rake Multiuser Performance at SNR_{TX} per bit = 11 dB

best multiuser performance in the forward link. Also in a Rayleigh channel the space-time algorithm can provide a good diversity gain while separating a multitude of users. Obviously the efficiency of the space-time filter for colocated users in a Rician environment degrades compared to the other two scenarios. Also note that the space-time algorithm is quite involved and we expect it to require a great of power consumption at the AP.

Chapter 5

Space-Time Coding Applied To Forward Link Applications

Having explained the hardware constraints in Chapter 2, the wireless channel characteristics in Chapter 3, and multiple access information theory in Chapter 4, in this Chapter I wish to evaluate the benefit of adding multiple antennas at the access point to increase the multiple access performance. In a first instance I build a system architecture for a wireless link where the multiple access is efficiently shared between CDMA and SDMA. Because the system is intended to be built on chip the complexity must be constrained, and a suboptimal forward link space-time scheme is developed consisting of a spatial precoder at the AP and a temporal equalizer at the UT. Also the ultimate goal here is to define the DSP requirements while keeping in mind the contributions from non-ideal analog electronics and wireless channel characteristics. The hardware requirements are evaluated using Cadence's Design Analyzer, effectively providing the transistor level circuitry information when input the VHDL code, and assuming the Artisan 0.18-μm CMOS library from TSMC provides the low-level logic operations construction, such as the flip-flop, the inverter and the XOR. After simulation with Design Analyzer, in the digital design flow, the next step before testing and manufacturing is the definition of the chip layout. In a second instance we evaluate the possibility of adding an antenna array to WLAN 802.11b basestations in order to increase the number of users that can share the same time and frequency slots during communication. In order to evaluate the performance of this system we employ the channel measurements taken in Section 3.3 and show that the capacity can be doubled using 4 circular antennas at the basestation.

5.1 Spectrally Efficient Multi-Access Application

In this Section I use the space-time multiple access schemes developed in Chapter 4 to develop a spectrally efficient multiple access scheme which simultaneously transmits data to spatially separated users in an indoor environment. In this design I profit from the fading conditions characterizing the indoor channel. The user data rate is 4 Mbps and is DQPSK modulated. A 12-element antenna array is used at the access point while a single antenna is present at each mobile. There may be as many as 32 users simultaneously occupying a single channel. Although this network is optimized for forward link communication, it is designed to allow reasonable communication speeds in the reverse link as well: the reverse link data, which is currently used solely for synchronization and channel estimation, may be made to contain a payload in future design iterations. To limit the bandwidth, the chip rate is made 16 Mcps, and the spread message occupies a bandwidth of 19.2 MHz after pulse shaping (the pulse shaping factor is $\alpha = 0.2$). The spread factor is 8 and Walsh codes as well as PN sequences are available for spreading. The signal is transmitted in the 5.6-GHz unlicensed spectrum. A time division duplex (TDD) scheme is adopted to divide the allocated bandwidth between a first time slot dedicated to the reverse link and a second for the forward link. The complete TDD period spans 40 msec, which is of the same order as the channel coherence time (see Chapter 3). Therefore, the data obtained during the reverse link may be used to estimate the channel for the forward link. The channel information is necessary to calculate precoding weights at the access point and the channel estimator is assumed to provide perfect amplitude, phase and delay information.

In this Section, firstly, I present a rudimentary physical layer interface to allow network control for multiple users in a single frequency slot and secondly we describe the physical layer architecture for multiple access communication. The definition of the message format outlines the input-output ports of the physical layer and thus serves as a more detailed description of the chip to be built. We shall present the bit error rate performance and provide an evaluation of the digital signal processing hardware requirements in 0.18-μm CMOS technology. The physical layer is first described for flat fading conditions and is then evaluated for a more realistic dispersive channel. In the forward link, the hardware complexity is shared among the access point (responsible for the spatial filter) and the user terminal equipped with a minimum complexity temporal decorrelating equalizer inspired by multiple user detection. This suboptimal method will be compared with a space-time precoder structure implemented at the access point.

5.1.1 Network Control

To define the digital hardware requirements of the physical layer, in this Section we describe the latter's input/output interface and the frame structure it is expected to process.

Having defined the analog hardware and channel characteristics in Chapters 2 and 3 respectively, here we add the protocol to the upper layers in the communication stack. The protocol represents the minimal input commands needed to provide user access to the network. It also describes the data to be transmitted (input) and the detected data (output) as well as other messages between the upper layers and the physical layer itself. The physical layer is divided into two separate entities: the first is responsible for processing public messages (intended to all UTs in the network), and the second is responsible for processing dedicated messages (private communication with each UT). The physical layer hardware description in this project is limited to the processing of dedicated messages. As indicated above, we will provide, for this dedicated message processor, the format of the frame on the reverse and forward link to allow synchronization in reception mode, and allocate proper resources for channel estimation and adaptive filtering.

Physical layer interface

The physical layer structure is shown in Figure 5.1 where the PHY controller is an entity responsible for controlling the physical layer in a fashion similar to the medium access controller in the 802.11 standard. Note that in this architecture the physical layer is a stateless entity: it simply reacts to the commands of the controller and contains no major behavioral logic.

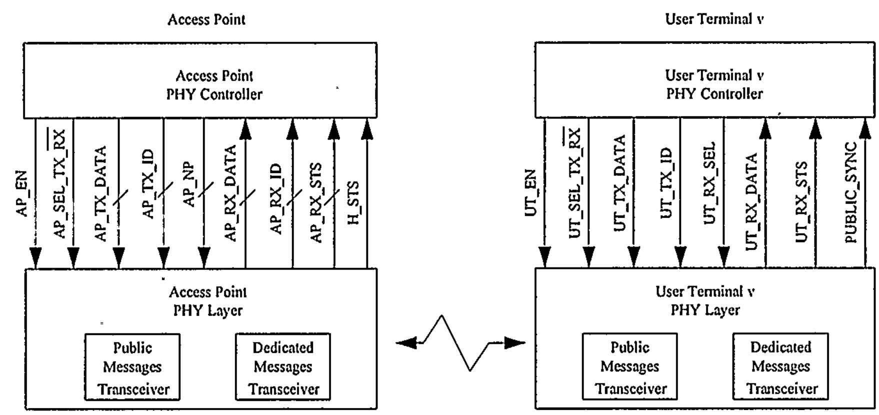

Figure 5.1: Network Modules

The TDD scheme defines two time slots applied on a single allocated channel:

- The forward link, where the AP communicates to the UTs,
- The reverse link, where UTs transmit to the access point.

The time allocation for each slot and the timing of the control signals is represented in Figure 5.2. The complete TDD period spans 40 msec. For synchronization of the time slots, the AP transmits an uncoded public message. Before initiating communication and requesting a network ID, each UT must initially attempt to synchronize to the beginning of this public message. Once the user is locked to the public message,

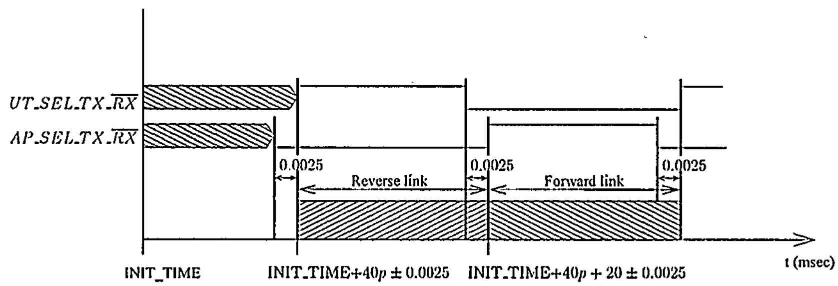

Figure 5.2: Timing Of the Reverse And Forward Link Slots.

the synchronization time, representing the beginning of the first TDD period is forwarded to the PHY Controller. The original synchronization time is denoted in Figure 5.2 as INIT_TIME. To reflect current standard definitions (UMTS defines the TDD period precision at 2.5 μsec), the TDD period precision is 2.5 μsec. The UT upper layer is responsible for setting the $UT\_SEL\_TX\_\overline{RX}$ during reverse link and clearing it during the forward link. In parallel the AP upper layer is responsible for setting the $AP\_SEL\_TX\_\overline{RX}$ during the forward link and clearing it during the reverse link. In both cases the upper layer uses the INIT_TIME information to maintain the period precision and as shown in Figure 5.2 the access point reception is enabled at time $t = (INIT\_TIME + 40p - 0.0025)$ msec while the user terminal reception is enabled at time $t = (INIT\_TIME + 40p + 20 - 0.0025)$ msec where p represents the TDD period index. This relieves the burden on the sliding window correlator described in Section 2.1.3: after initial synchronization with the public message transmitted by the AP, the INIT_TIME is defined and the sliding window correlator will only attempt to synchronize within 5 μsec after the command $UT\_SEL\_TX\_\overline{RX}$ is cleared. We can observe that because the AP receiver must be started 2.5 μsec before the actual start of the reverse link, there is a band guard at the end of the forward link. The effective forward link duration becomes 19.9975 μsec rather than the defined 20 msec. A band guard is also present at the end of the reverse link to allow time for the UT receiver to synchronize.

The dedicated messages are simultaneously sent through a unique frequency allocation with a bandwidth of 19.2 MHz at $f_c = 5.6$ GHz. A combination of SDMA and CDMA techniques are used to increase the multi-access performance.

The access point transmits dedicated messages simultaneously to a maximum of 32 users in a single time-slot (reserved for the forward link) and receives dedicated messages from the users in the second time-slot (reserved for the reverse link). The transmit frames are precoded and modulated at the physical layer. For the forward link, as specified in the requirements, the data rate is fixed at 4 Mbps (per user) and during transmission mode, the binary data AP_TX_DATA is transmitted by the AP's physical layer. Note that the chip rate is constant for both the reverse and forward link: it is set to 16 Mcps. During the reverse link each symbol is encoded with a unique 511-chip Gold code to keep a low code correlation. This allows a reciprocal characterization of the channel during the reverse link, at the cost of a reduced data transmission rate of 62.5 kbps.

MESSAGE	DESCRIPTION	STRUCTURE
AP_EN	Enables communication.	1 bit
AP_SEL_TX_RX	Sets transmitting (1) or receiving (0) mode.	1 bit
AP_TX_DATA	Data bus to U UTs at time n.	AP_TX_DATA[u]: Current Binary Data
AP_TX_ID	Code ID bus to U UTs at time n.	AP_TX_ID[v]: Current user code ID
AP_NP	Noise power at all UTs.	AP_NP[v]
AP_RX_DATA	Data bus from U UTs,	AP_RX_DATA[v]: Detected Binary Data
AP_RX_ID	Code ID bus from U UTs,	AP_RX_ID[v]: 1 byte
AP_RX_STS	Current receiver status.	1 byte
H_STS	Channel status	1 byte

Table 5.1: AP Physical Layer Interface Messages Definition

The exchanged data structure between the physical layer and the upper layers of the network is defined in Table 5.1 for the AP. The corresponding data structure necessary at the user terminals is shown in Table 5.2. At this point, only the structure needed for dedicated messages is taken into account and the design of the physical layer does not currently account for public messages, which may be transmitted through a different medium (for example, to test the dedicated message functionality, the public messages can be sent through a wired connection). The role of each IO is elaborated in the description of each hardware component (i.e. the access point transmitter and receiver, the user terminal transmitter and receiver) in Section 5.1.2.

MESSAGE	DESCRIPTION	STRUCTURE
UT_EN	Enables communication.	1 bit
UT_SEL_TX_$\overline{\text{RX}}$	Sets transmitting (1) or receiving mode(0).	1 bit
UT_TX_DATA	Dedicated data to AP,	1 bit
UT_TX_ID	User Transmit Code ID	1 byte
UT_RX_SEL	Selection of receiver architecture: 0: RAKE, 1: Decorrelator	1 bit 1 bit
UT_RX_DATA	Dedicated data from AP.	1 bit
UT_RX_STS	Current status of the receiver.	1 byte
PUBLIC_SYNC	Indicates TDD start time.	

Table 5.2: UT PHY Interface Messages

Frame Content

To implement a practical system, it is necessary to add a training sequence in the frame to synchronize and compute optimal weights. In a first instance we shall show the necessary timing requirements on the reverse link, followed by those for the forward link. The network timing requirements for the reverse and forward link receivers are shown in Table 5.3.

In the reverse link, the symbol is encoded with a 511-chip Gold sequence. At the receiver, a sliding window correlator produces a coarse acquisition of the signal.

Table 5.3: Reverse and Forward Link Timing Requirements

	Formula	Duration
Reverse link		
Single Correlation	511×62.5 nsec	31.9 μsec
Maximum Sync. Time	31.9 μsec $\times 80 \times 2/4$	1.3 msec
Channel Estimation	511×62.5 nsec	31.9 μsec
Adaptive Filtering	200×31.9 μsec	6.4 msec
Total	(1.3 +0.0319 +6.4) msec	7.7 msec
Forward Link		
Single Correlation	511×62.5 nsec	31.9 μsec
Maximum Sync. Time	31.9 μsec $\times 80 \times 2/4$	1.3 msec
Channel Estimation	511×62.5 nsec	31.9 μsec
Total	(1.3 +0.0319) msec	1.33 msec

This is similar to the structure presented in [48]. The acquisition is precise to within half a chip and 4 correlators are implemented in parallel to reduce synchronization time. In this project, because the chip period is 62.5 nsec, a single correlation requires approximately 31.9 μsec, and repeating until synchronization within a 5- μsec window (equivalent to 2×80 sample delays) requires a maximum time of 1.28 msec.

Also, assuming all paths are estimated in parallel, a channel estimation algorithm precise to the chip period requires a single correlation (for each path) spanning 31.9 μsec.

Finally, assuming a symbol rate adaptive algorithm is used to calculate spatial precoding weights, multiple iterations are required to allow the estimation to converge and consecutive symbol arrivals must be considered. Using results in [18], we assume that 200 points (6.4 msec) are sufficient to converge toward the optimal solution. The total time for pre-detection processing is 7.7 msec (240 symbols), and we allow a 50% headroom which amounts to 11.5 msec (360 symbols). Assuming the time division duplex period is equally separated in two slots of 20 msec each, the reverse link payload occupies 36% of the frame.

During the forward link, time must be allowed to synchronize and implement a channel estimation algorithm. Note that a (16-Mcps) 511-chip scrambling Gold code is added in the header of the transmit signal at the AP and a replica is locally generated at the UT receiver for synchronization. No adaptive algorithm is necessary at the UT receiver. Reusing the same sliding window correlator implemented on the reverse link, the time required for synchronization and channel estimation is 1.33 msec. The payload occupies approximately 93% of the frame.

5.1.2 Hardware overview

Reverse Link Operation - The User Terminal Transmitter

Firstly, we describe the network control protocol necessary for a user to begin transmission on the reverse link. A user terminal v desiring access to the network must transmit a request for an identification to the access point through a public message. In the upper layers of the network stack, the user terminal attempts to synchronize with the beginning of the forward link until synchronization is confirmed. Once it is synchronized, the user terminal may send a request for network identification to the AP during the next reverse link time slot. If the access point is available, an identification grant is returned to the user terminal with a specific network ID in the forward link time slot. Upon reception of this network ID, the network upper layer selects the appropriate code c_v associated with the network ID and forwards this information to the physical layer for dedicated communication. Only then can the user terminal begin bi-directional communication with the access point using this ID.

Secondly, we describe the development of the DSP hardware necessary for the dedicated message format transmitter. To limit the user terminal power consumption an asynchronous UT_EN control message can be cleared at the user terminal physical layer. With this setting, the physical layer ignores changes to its IOs. In contrast, when the UT_EN and $UT\_SEL\_TX\_\overline{RX}$ are set, the physical layer's digital baseband modulates, encodes and pulse shapes the information data UT_TX_DATA synchronously read from the input signal before applying it to the digital to analog converter (DAC). This is shown in Figure 5.3.

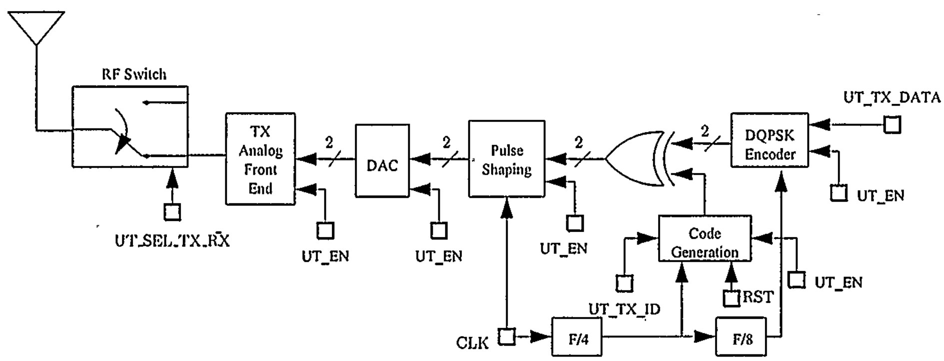

Figure 5.3: User Terminal Transmitter Physical Layer Architecture.

The DQPSK hardware structure is shown in Figure 2.8. To respect the symbol rate, its input clock period is 2 MHz. The output contains the in-phase and quadrature components and is spread by the locally generated spreading code. The spread code clock input period is 16 MHz. Finally, the data is applied to a raised cosine filter using a truncated IIR filter implementation as described in Section 2.1.3. Its sample rate is 64 Msps to further the output minimum image frequency at 64 MHz allowing flexibility in the design of the image-reject low-pass filter. As explained in Section 2.1.3, the pulse shaping filter is typically truncated to ± 6 symbol periods, hence the equivalent FIR filter tap count is $T = 48$. The filter coefficient at tap t, C_t is represented using a 7-bit fixed point precision (which is denoted $C_{fx,t}$). This effectively limits the total coefficient squared error SE defined as:

$$SE = \sum_{t=1}^{T} (C_{fx,t} - C_t)^2, \tag{5.1}$$

below 10^{-4}, thus providing an output approaching floating point precision. Application of a binary signal to this filter requires 48 additions of the content of the 7-bit shift register at each tap delay. Because the maximum total power at a given sample time is $P_{tot} = \sum_{t=1}^{48} C_t^2 = 24.5$ W and the full scale representation of each register is 1 V, the matched filter output is approximately 5 times the input full scale range. To represent a signal 5 times greater than the input a minimum of 3 bits must be added to avoid overflow resulting in a minimum of 10 bits at the output of the raised cosine filter.

Reverse Link Operation - The Access Point Receiver

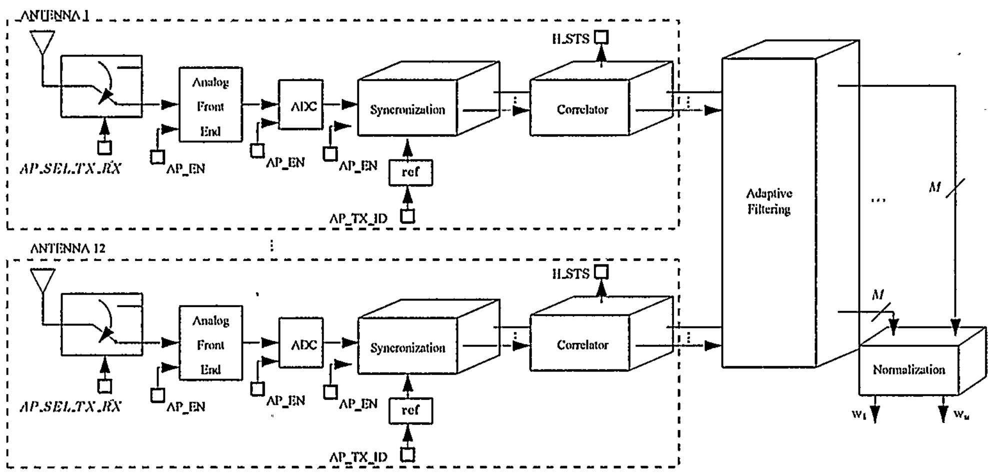

Figure 5.4: Access Point Receiver Physical Layer Adaptive Filtering Architecture.

The reverse link is asynchronous, i.e. the received signals at the access point are not aligned to the beginning of each symbol. Because the propagation speed of an electromagnetic signal in air is 3×10^8 m/sec, the signals are received by the access point with a maximum delay of 33 nsec after the beginning of the reverse link time slot (the maximum main path propagation distance is 10 meters). After downconversion and conversion to a digital representation, the physical layer is responsible for synchronizing to the main path arrival of the received signal for each user. This is achieved with a sliding window correlator previously described in Section 2.1.3. In this

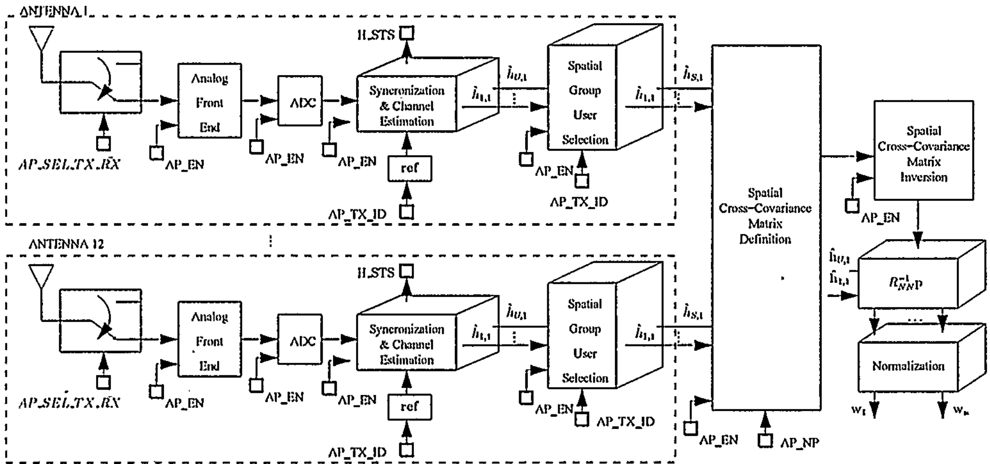

Figure 5.5: Access Point Receiver Physical Layer DMI Architecture.

project, after synchronization, we wish to find spatial filter weights to separate users that are coded with a common signature. The focus is on the forward link weights. For each group of users with common code c_x, the spatial weight reuse algorithm (with a constant transmit power) described in Section 4.1.2 is used to separate the users within the group. In a low-power digital design, the challenge remains in obtaining weights and two methods can be considered: a) an adaptive method shown in Figure 5.4 and b) a direct matrix inversion (DMI) method shown in Figure 5.5. In [18], Ung solves the spatial weights adaptively in a flat fading fading channel for re-use in the forward link and we will demonstrate that this is also possible combined with spread spectrum techniques if strict conditions are met. Alternatively, the direct matrix inversion (DMI) solution involves defining the linear transfer function representing the relationship between the access point transmitter and all user terminal receivers with a closed-formed mathematical equation. In this situation, solving the optimal weight requires not only estimating each element of the space-time cross-covariance matrix between the antenna array elements, but also inverting this matrix. These steps are usually quite involved.

In Section 4.1.2 we describe the weight reuse algorithm for a flat fading channel without spread spectrum. Here, we are using the antenna array to spatially separate users coded with a common spreading code where CDMA provides additional multiple access capabilities to the basic spatial scheme. Also, the 19.2-MHz indoor channel is known to be dispersive. The space-time algorithms presented in Section 4.3 require complex processing and are impossible to implement in low-power designs. A complete characterization of the multiple user forward link model requires a space-time matrix and is dependent on the signature cross-correlation for the relative channel delays. The optimal forward link MMSE weight vector is provided with a space-time pre-equalizer and spans multiple symbol periods. In this case, not only is the adaptive algorithm impractical, the dimensions of the square matrix to be inverted are directly proportional to the user count U and symbol count N necessary for equalization. Above all, a channel estimation algorithm responsible for determining the channel characteristics (multipath amplitude and phase) at each antenna m for each recognizable path delay l and each user u increases the complexity of the physical layer. To limit the access point complexity we are spatially precoding uniquely the first path arrival on the forward link rather than implementing the space-time architecture shown in Figure 4.27. The temporal processing is neglected at the transmitter in the forward link because we expect the user terminal receiver to have the hardware capacity to perform temporal equalization. To find the flat fading optimal theoretical weights as discussed in Section 4.1 using reverse link weight re-use, it is necessary to evaluate (flat fading) channel reciprocity in these new conditions.

To evaluate reciprocity, initially we describe the most basic system already developed in Section 4.1 and evaluate the consequences of incrementally upgrading the system. Initially, for an uncoded system reduced to an SDMA algorithm in a frequency flat channel with quasi-static channel fading conditions, the symbol asynchronous properties (characterized with misaligned multiuser symbol arrival times at the access point) in the reverse link bear no consequence on the cross-covariance matrix: the mathematical model is equal in both directions and the weights adaptively evaluated during the reverse link can be re-used. As concluded in Section 4.1.2, in a theoretical synchronous flat fading reverse link, the space-time linear transform representing the forward and reverse link are reciprocal.

Alternatively, in Section 4.3.3 we have demonstrated the lack of reciprocity between the (asynchronous) reverse link and (synchronous) forward link using space-time encoding. At this point it is important to note that, on the forward link, because we intend on using Walsh codes the flat fading cross-correlation performance is perfect. In order to provide an equivalent cross-correlation performance on the reverse link, examining closely the equivalent cross-correlation matrix defined in Equation (4.40), it can be seen that the difference is due uniquely to the asynchronous properties of the reverse channel coupled with the given spreading code.

From the above discussion, adaptive methods on the reverse link will not offer the exact flat-fading solution unless the asynchronous code cross-correlation properties are null as is the case in the forward link. Additionally the off-peak auto-correlation of the codes applied in the reverse link must be null to insure that the output of the single correlator matched to the first path is not corrupted with inter-symbol interference and acts as a perfect time equalizer precise to the symbol rate.

A single path, direct matrix inversion (DMI) solution, although quite involved, represents the flat fading optimal solution for pre-coding in the forward link. Because matrix inversion is computationally intensive, the matrix dimensions must be restrained. In respecting this condition, the access point responsibility during reverse link is limited to a) evaluating the channel dispersive properties, and b) defining a spatial weight optimized to minimize the mean square error when applied to the first channel path. Because the 511-chip Gold code used during the reverse link has relatively good properties (the maximum off-peak auto-correlation and cross-correlation are approximately 0.06), an adaptive algorithm offers a good alternative solution and should also be evaluated. In forward link frequency selective channels, both these solutions are suboptimal compared to a space-time precoder, but the system relies on the user terminal receiver to equalize the received signal and maintain a reasonable quality of service (QoS).

Finally, the channel dispersive characteristics are transfered to the upper layers of the access point receiver using the H_STS message (see Table 5.1). The H_STS message is critical because, as we will see, it defines the maximum user count allowable in the forward link.

In Figure 5.5, we show the hardware architecture for the AP reverse link receiver including the front-end and analog-to-digital converter (ADC). At each antenna element, the output of the ADC is synchronized with a reference training signal associated with each user network ID. Note that for synchronization purposes during the reverse link a scrambling code unique to each user must be present in the frame header to allow acquisition with each user at the AP. The sliding window correlator used for synchronization also produces a channel amplitude (and phase) estimate at each antenna element m and for each user v. The multipath channel estimation result is forwarded to the network upper layers which will define the maximum user count in the channel. The first path arrival channel estimation is also used to evaluate the weight vector w_v to be applied on the forward link. To achieve this, the users are separated in spatial groups in which the CDMA code c_x is reused. The code reuse is allowable because the users shall be spatially separated. In Figure 5.5, the structure is shown for a single group and all hardware blocks following the synchronization must be repeated for all defined groups. Because of spatial theoretical restrictions stating that the maximum number of users that can be spatially separated with M antennas is M (see [40]), the maximum number of groups is limited to 12. For a given group associated with code c_x, the users are spatially separated. Because Walsh codes used in the forward link provide perfect cross-correlation performance, inter-group interference is null and it is possible to segregate the complete linear transform in independent sub-matrices. The covariance matrix for all users of a group with a unique CDMA code is defined in Equation (4.9) and repeated here for convenience:

$$\mathbf{R} = \sum_{u=1}^{U} P_u(\mathbf{h}_u^H \mathbf{h}_u) + N_0.$$

The noise power N_0 represents the noise power at the user terminal receiver and it is obtained with the message AP_NP from the network upper layer. Here we assume that a wireless scheme (for example using the public message protocol) allows users to share the mean noise power property with the access point. Because of theoretical limitations, we define a maximum of twelve users per group. Using 8 different signatures will accumulate to 96 users but because the interference rejection in this case amounts to poor BER performance, the maximum number of user is limited to 32, in which case the reuse count is 4. In severely dispersive channels, we will show that hardware constraints at the user terminal receiver restrict the system to a single CDMA code and then all users (up to a maximum of 8) belong to a unique spatial group.

To obtain the forward link weights the remaining steps involve:

1. $\mathbf{R}$ matrix inversion for each group,
2. Application of the cross-covariance vector $\mathbf{p}$ for each user,
3. Normalization of the weight vector to maintain a constant transmit power.

In Figure 5.4 a possible alternative for the direct matrix solution, using an adaptive algorithm, is represented. As we explained previously, using the adaptive algorithm, we expect a degradation in performance (compared to the DMI solution which obtains optimal theoretical weights under the assumption that channel estimation is perfect) due to imperfect signature cross-correlation when obtaining weights. Nonetheless, the simple digital architecture is very appealing. Indeed, not only can the correlator be used for channel estimation, it is also the input to each adaptive filter. An adaptive filter must be implemented for each desired user, and the processing can be done in parallel such that the weights can be solved in a minimum time requirement.

Forward Link Operation - The Access Point Transmitter

Over the forward link, all signals are transmitted synchronously. The access point transmitter architecture is shown in Figure 5.6. A control command AP_EN enables the access point physical layer hardware components and the command AP_SEL_TX_$\overline{\text{RX}}$ enables the transmitter components of the physical layer when set. At 4 Mbps a new set of binary data AP_TX_DATA is updated at the input of the physical layer for all desired users and is transmitted by the physical layer. The digital processing involves DQPSK encoding as described in Section 2.1.3 followed by encoding with CDMA signatures. Note that the signature IDs for each user are input by the upper layer and they may be reused. Users with reused codes are spatially separated. There are as many as eight CDMA codes, which may be re-used a maximum of twelve times. In Section 5.1.3, we will show the importance of code selection for different channel conditions: in this design for relatively low channel dispersive properties a Walsh code is applied and as the conditions deteriorate the application of a common PN code for all users allow a simple equalizer structure at the user terminal receiver. The re-use ratio is limited by the theoretical spatial filter performance with 12 antennas. As explained in [40], the maximum possible number of spatially separated users (for a given group coded with code c_x) is equal to the antenna count. After CDMA encoding, each user v is applied an 8-bit with fixed point representation spatial weight vector $\mathbf{w}_v^*$. The quantization precision is chosen to limit the quantization error below 1% of the full scale range. The weights implementing a linear minimum mean square error (MMSE) filter for a fading path arrival have been computed during the reverse link and are optimal in a flat fading channel. For a frequency selective channel, the performance is suboptimal, but we are assuming the user terminal may implement a time equalizer structure to limit the degradation due to multipath.

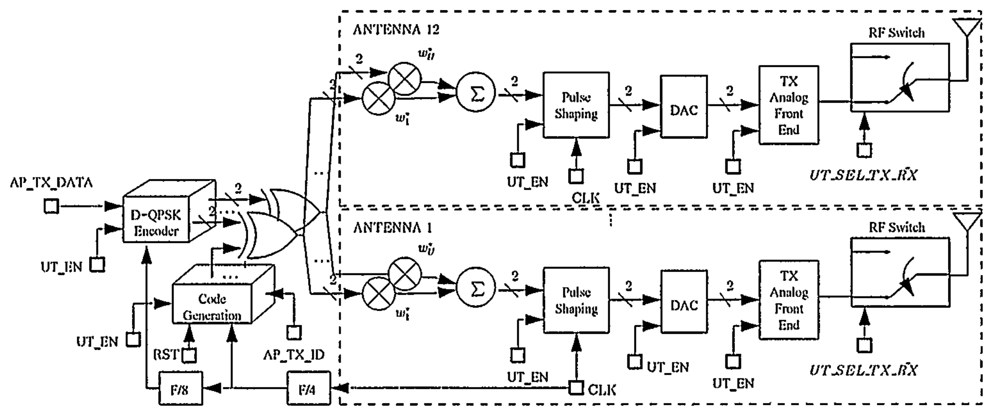

Figure 5.6: Access Point Transmitter Physical Layer Architecture.

The output of the spatial combiner is applied to a raised cosine filter with similar specifications as the raised cosine filter present in the user terminal. The filter is characterized with 48 taps each using 7-bit representation coefficients, and the output of the filter is quantized with an 11-bit precision.

We evaluate the access point precoder power consumption for a supply voltage V_{dd} = 1.8 V. The calculations for the adder and multiplier are based on empirical models cited in [3] for CMOS 0.25-μm, and scaled to 0.18 μm, using the linear relashionship between power consumption and capacitance C_L described in Equation (2.2). For the other logic functions and shift register accesses, the power consumption is found in

[6]. The power consumption for the transmitter components is reported in Table 5.4.

Table 5.4: Access Point Precoder Power Consumption Analysis

	Module Count	Bit Precision	Power Consumption (mW)
<u>CDMA Encoder</u>			
Exclusive-OR	32	1	0.64
<u>Spatial Precoder</u>			
Real Multiplication	4 x 12 x 32	8	16.06
Real Addition	2 x 12 x (32-1)	11	3.33
Total			19.37
<u>Raised Cosine Filter</u>			
Unit Delay	(48-1) x 12 x 2	8	76.18
Real Multiplication	48 x 12 x 2	8	704.48
Real Addition	(48-1) x 12 x 2	11	10.08
Total			790.74

Forward Link Operation - The User Terminal Receiver

The access point is responsible for spatial separation of users and is designed for frequency flat channels. As the channel characteristics become dispersive, a time equalizer must be implemented at the user terminal. In this project, for severely degraded multipath conditions, we use multiple user detection theory to implement a multipath decorrelator that completely removes the effect of multipath at the output of the code correlators. The multipath decorrelator is described in Section 4.2.4. In this situation, the amount of users must be restricted and a single code must be present in the network to limit hardware complexity at the user terminal receiver. Alternatively, as the dispersive properties of the channel become less severe, a RAKE receiver becomes sufficient in obtaining a reasonable communication performance. The structure of the user terminal receiver is shown in Figure 5.7. A control signal UT_EN enables the individual blocks of the receiver physical layer. Additionally, the $UT\_SEL\_TX\_\overline{RX}$ command redirects the signal at the antenna to the user terminal receiver.

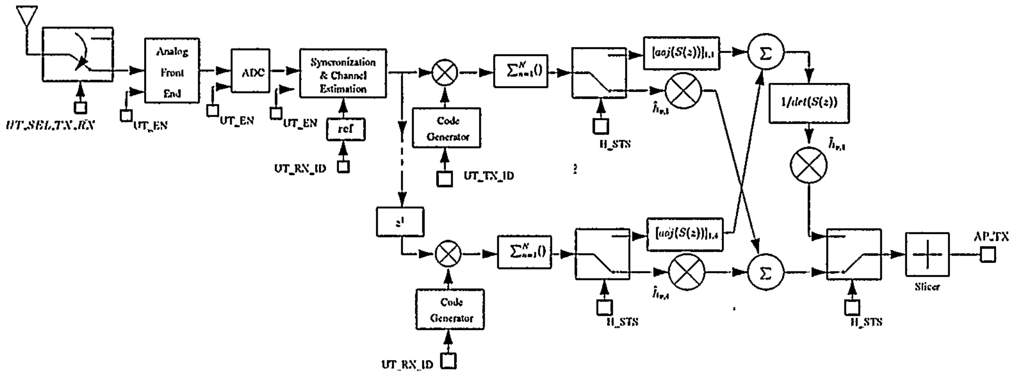

Figure 5.7: User Terminal Receiver Physical Layer Architecture.

After analog-to-digital conversion (ADC), the first step involves synchronization with the reference signal and channel estimation. A reference signal is compared with the received signal (the reference signal was also transmitted in the header of the frame) and a sliding window correlator is implemented. The channel estimation is precise to the chip period and is evaluated at four consecutive chip delays (including the first path arrival) spanning a delay spread of 250 nsec.

Following the synchronization, a code correlator is implemented for each known path. In this system, three fingers are implemented and combined to increase performance. Because channel estimation is limited to only three chip delays following the main path arrival, the receiver selects the three greatest path amplitudes among the four estimates for combining.

A switch selects the type of combiner to implement at the output of the correlators: the RAKE filter or the decorrelator. The type of filter used depends on the channel delay spread and is defined with the input H_STS. Note that the CDMA code ID is input from the upper layer and sets the ID of the code to be generated. When the decorrelator is implemented, the PN code c_{dec} = [11100011] is generated, while when the RAKE filter is implemented, a Walsh code is generated. Because the decorrelator offers no solution for certain codes when applied to a channel with four discrete chip delays, the specific code c_{dec} was selected to assure a solution existed for all multipath combinations.

As shown in Figure 4.18, the RAKE receiver multiplies the output of each finger synchronized to the delay l with the complex conjugate of the channel amplitude $h^*_{v,l}$ at this delay.

As interference increases, the RAKE receiver output can no longer sustain the necessary QoS. In this case a decorrelator inverting $\mathrm{S}(z)$ is preferable. Unfortunately, for multiple groups, the decorrelator power consumption is very large. For example, implementing a decorrelator involving 2 CDMA groups, each received using 3 matched filters, will require a 6×6 matrix inversion. Although this multiuser decorrelating filter is limited to 11 tap delays, the amount of operations needed to compute the adjoint filter coefficients cannot be reasonably accommodated by practical low-power IC implementation. Additionally, it cannot be assumed that user terminals know all user signatures in the network.

Removing multipath distortion from just the first path arrival, only decorrelated data for the first path is needed, and only the first row of $\mathrm{S}(z)^{-1}$ is computed. In this case, the output of the decorrelator z_v at user terminal v is:

$$z_v = \frac{[\mathrm{adj}(\mathrm{S}(z))_{1,1}\ \mathrm{adj}(\mathrm{S}(z))_{1,2}\ \mathrm{adj}(\mathrm{S}(z))_{1,3}]}{\det(\mathrm{S}(z))} \times \mathbf{y}_v,$$

where z_v is the decorrelator output and represents the output of the first matched filter with removed inter-symbol interference. Each adjoint element of the 1×3 sub-matrix of $\mathrm{S}(z)^{-1}$ is a FIR filter with 5 taps; the filter generates a delay of 2 symbols in the signal path to ensure causality. The necessary adjoint coefficients are calculated using the asynchronous cross correlation coefficients, and vary for different discrete multipath selections.

Following the summation of the time dependent adjoint filters at the output of each code correlator, the signal is filtering with the $1/\det(S(z))$ IIR filter. This filter must be truncated to a reasonable amount of taps to respect causality and ensure a minimal delay is present in the system. The tap filter coefficients for the chosen PN code are shown in Figure 5.8. They are dependent on the code cross-correlation matrix and for a single code the only variable parameter controlling the coefficient becomes the path arrival selection. Actually, in applying the decorrelator, using a 3-finger receiver synchronizing to the 3 maximal amplitude paths out of a possibility of four consecutive paths, only four different path selections are possible. In Figure 5.8 the filter taps are shown for the four different path selections. Interestingly, it can be seen that different dispersive channels result in the same filter coefficients and only two sets of coefficients must be kept in memory to account for all possibilities. We can also conclude from this Figure that a seven-tap FIR filter shall adequately represent the IIR filter. The output of the $1/\det(S(z))$ is applied to a DQPSK decoder, and the binary data is updated at the output UT_DATA_RX of the digital processor. Finally, note that in a traditional QPSK system the output of the decorrelator must be co-phased but for DQPSK modulation this step may be skipped.

The binary data UT_RX_DATA estimated is forwarded to the network upper layers. As well, the receiver status is forwarded to the network upper layers through the message UT_RX_STS.

In [57], we evaluate the power consumption of the receiver detector using 0.18-μm CMOS. The simulator used is Cadence's Design Analyzer. For the decorrelator filter coefficients, using a floating point to fixed point conversion, it is found that the adjoint filter coefficients must be represented with 12 bits, and the inverse determinant filter coefficients use 16 bits to obtain a maximum imprecision error of 10%. Also, for the RAKE combiner, knowing that a 0.1 weight amplitude normalized to the first path

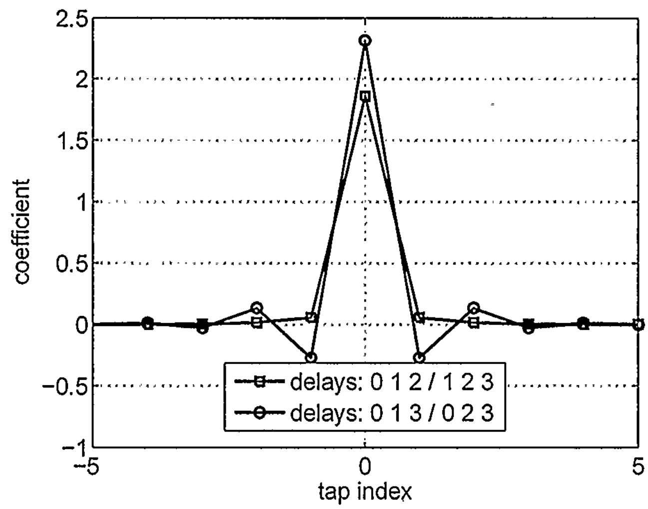

Figure 5.8: One Over Determinant Filter Coefficients.

will have minimal effect at the output of the combiner, the combiner weights are represented with 6 bits. Concerning the received signal quantization, we arbitrarily set the automatic gain control (AGC) dynamic range to twice the maximum signal amplitude. It is found through Matlab bit error rate simulations that the necessary bit count for the 32 UT RAKE combiner is above 4. Further simulations have shown that the 6 bit representation is very close to floating point precision for both the decorrelator and the RAKE combiner.

In [57], we also evaluate the signal path power consumption for a supply voltage V_{dd} = 1.8 V. The calculations for the adder and multiplier are based on empirical models cited in [3] for CMOS 0.25-μm, and scaled to 0.18 μm, using the linear relashionship between power consumption and capacitance C_L described in Equation (2.2). For the other logic functions and shift register accesses, the power consumption is found in [6]. The power consumption for the receiver filters is reported in Table 5.5. In total, the RAKE receiver requires 0.3 mW, and the zero-forcing equalizer, 2.0 mW. In comparison, assuming it is possible to invert the $6{\times}6$ matrix, a 2-user decorrelator detecting the uth user requires 6.9 mW.

Table 5.5: User Terminal Detector Power Consumption Analysis

	Module Count	Bit Precision	Power Consumption
Correlator Bank			
Sign inversion	48	6	5.0 μW
Additions	48	6	6.7 μW
Unit Delay	42	6	51.4 μW
Total			63.1 μW
RAKE Combiner			
Real Multiplication	12	6	230.2 μW
Real Addition	2	12	3.1 μW
Total			233.3 μW
Adjoint Filter			
Real Multiplication	30	12	1095.9 μW
Real Addition	24	12	18.5 μW
Unit Delay	24	6	29.4 μW
Total			1143.8 μW
Filter $det(S(z))^{-1}$			
Real Multiplication	14	16	734.8 μW
Real Addition	14	12	10.8 μW
Unit Delay	12	12	29.4 μW
Total			775 μW

5.1.3 Communication Performance

To evaluate the communication performance, I initially performed the simulations using Matlab 7.0, and I further validated the results using CoWare's Signal Processing Designer (formerly know as SPW) version 4.85 which provides a graphical interface as well as a low-level communication library. Both simulators were initially set up to simulate floating-point precision and SPW also provides a DSP library with fixed-point representation.

In the forward link, the data is sent synchronously. Additionally, in the frequency flat channel, there is no multipath arrival, therefore no loss in autocorrelation performance. Using an 8-chip per symbol spread factor, the maximum number of orthogonal (Walsh) codes is limited to eight. In order to increase the user count in the channel, users reusing the same code can be separated using a spatial filter. In Figure 5.9, we represent the space-time performance as a function of SNR in a frequency flat fading channel. The performance is represented for different scenarios. First, it can be observed that the 8-user scenario obtains a great performance and is theoretically equal to the single user performance. This is due to the fact that the codes are synchronous and in this situation Walsh codes present perfect orthogonality. In addition to CDMA orthogonality, the users are also spatially separated. This dual orthogonalization greatly increases performance. We also present the performance for four spatially separated users reusing the same CDMA code. In this case, only spatial precoding is used to separate users and this explains the loss in performance. In contrast, by observing the 32-user performance, we see that reusing codes among spatially separated users allows the reliable communication with many more users in the channel. Actually, if we compare the situation where a single group of 4 users (with a single CDMA code) is spatially separated with an increased amount of groups encoded with a different (orthogonal) code, the performance is equal. This shows the benefit of SDMA technology when combined with CDMA.

In Figure 5.10 we show the performance of the multiuser space time algorithm with an increasing amount of users in the network. Here again, the channel is flat fading and a noise source is present at the receiver such that the transmit SNR per bit is equal to -8 dB. This Figure validates our previous assumption: different groups of spatially separated users each coded with a unique signature are orthogonal amongst themselves and there is no loss of performance as the number of groups (coded with different signatures) is increased. Note that here the CDMA code is re-used among four users. Alternatively, for a constant code count (there are eight codes), as the

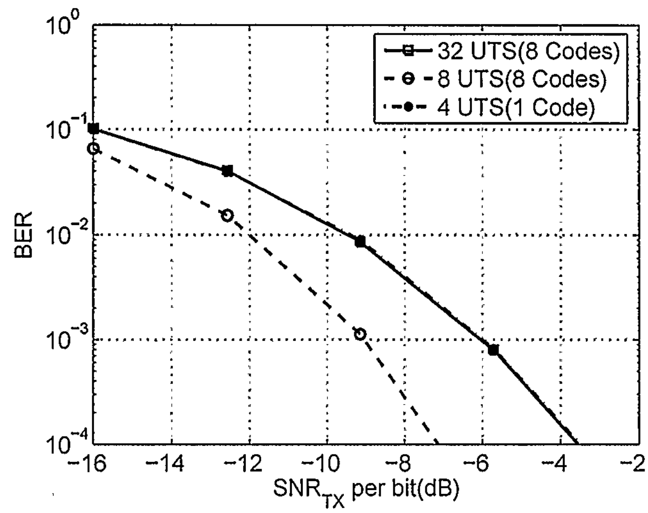

Figure 5.9: Space-Time Performance vs. SNR in Flat Fading Channel.

codes are repeated, the performance deteriorates as the number of users increases from 8 to 96.

In Figure 5.11, we show our space-time algorithm performance for a frequency selective channel where the $\tau_{RMS} = 30$ nsec as a function of SNR per transmit bit. The path count is limited to four discrete paths binned at the chip period. The system is evaluated for a 3-finger RAKE receiver as well as a 3-finger multipath decorrelator. We can see that in low signal-to-noise ratio environments, the 8-user and 16-user RAKE receiver outperforms the 8-user decorrelator. But above $SNR_{TX} = 4$ dB, the RAKE receiver seems to be limited by an irreducible BER while the decorrelator performance continues to increase. This is due to the fact that as SNR increases, the relative interference contribution to the undesired component is greater relative to the noise contribution. The RAKE receiver is a diversity scheme and it is optimal for noise limited environments. Because there is interference due to multipath, the RAKE receiver, particularly at high SNR is suboptimal. In contrast, the decorrelator performance is optimal for interference limited environment, which explains the

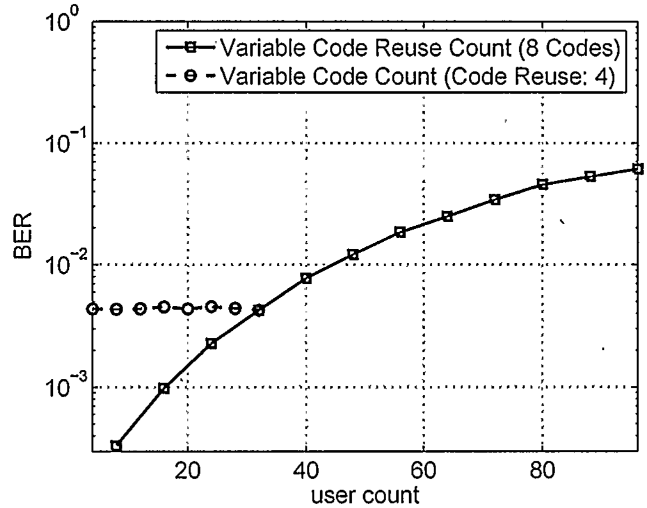

Figure 5.10: Multiuser Space-Time Performance In Flat Fading Channel (SNR_{TX} = -8 dB)

difference in performance.

Also, in Figure 5.12 the performance of our space-time algorithm is evaluated as a function of delay spread for an SNR_{TX} per bit = 0 dB. The delay spread varies from 5 nsec to 65 nsec, and we see that for low delay spread the RAKE receiver outperforms the decorrelator. More specifically, for τ_{RMS} < 18 nsec, the 32-user network still outperforms the decorrelator and as the delay spread increases, the user count in the network must be reduced, up to a limit (here, the limit is 40 nsec) where the receiver architecture must be switched to a decorrelator structure for best performance. Note that, from the conclusions we extracted from the previous Figure, we would expect the difference in performance between the decorrelator and the RAKE receiver to diverge even more as the noise power is decreased. The receiver characteristics for the different channel conditions is summarized in Table 5.6.

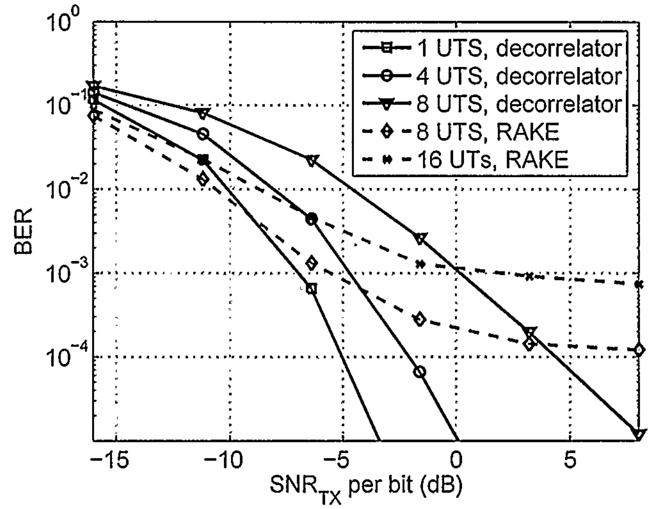

Figure 5.11: Space-Time Performance vs. SNR_{TX} per bit(dB).

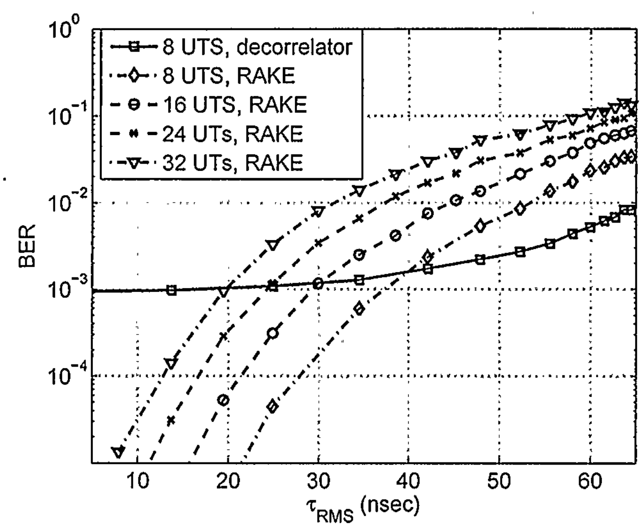

Figure 5.12: Space-Time Performance vs. τ_{RMS} .

Table 5.6: System Configuration For Different Delay Spreads

Max. Channel τ_{RMS}	18 nsec	25 nsec	30 nsec	40 nsec	-
Max. Number of Users	32	24	16	8	8
User per Spatial Group	4	3	3	1	8
Code Selection	Walsh	Walsh	Walsh	Walsh	PN
Receiver Architecture	RAKE	RAKE	RAKE	RAKE	Decorrelator

5.2 Benefits For 802.11b Technology

Currently WLAN multiple access is managed with a collision sense multiple access (CSMA) algorithm. CSMA seeks to avoid collisions between users by first sensing whether or not a transmission is occurring. Simultaneous transmission is not possible and when messages are corrupted by interfering users the frames must be dropped. In this Section, the benefit of adding antenna arrays to already existing WLAN access points is studied minimizing the forward link interference as seen by each user. Because the standard is currently vastly deployed for commercial use, minimal changes are proposed and the current access points are simply equipped with a new multiple antenna front end (including spatial coding) as shown in Figure 5.13. We can observe that the reverse link is useful in solving the optimal weights and the received signal is forwarded to the WLAN baseband processor. In the forward link the spatial weights solved previously for each user are applied to the transmit signal to modify the antenna array response.

As specified in the 802.11b standard ([45]) data is differentially modulated, simplifying receiver complexity at the expense of a 3 dB loss when compared to PSK modulation schemes. In normal mode of operation (at 1-2 Mbps), the data is spread with an 11-chip Barker code, with good autocorrelation properties. Alternatively, in the high rate configuration (5.5 - 11 Mbps), the data is modulated with complementary code keying (CCK). In this project, although the proposed spatial filter can be

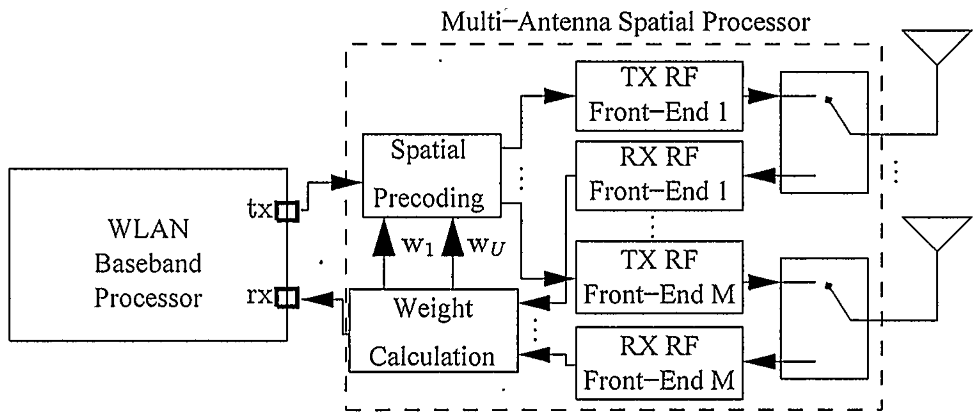

Figure 5.13: WLAN Spatial Processor Structure.

applied to both modes, the performance is simply analyzed at 2 Mbps combined with a 3-finger RAKE receiver. It is expected that the capacity improvement suggested by the normal mode will equally be applicable to the high rate of operation.

The 802.11b standard defines each frame with a preamble, header, and payload. The preamble consists of 128 spread bits used for synchronization. As explained in [42], precise channel information between all users communicating over the specific frequency allocation and the access point array must be available to provide adequate spatial weights on the forward link. Here, the frame preamble has a processing gain, $PG = 10 \cdot \log(1408) = 31$ dB, and when received at the access point during the reverse link, it can provide a reliable channel estimation.

In [54] a space-time precoding solution is proposed to increase the WLAN multiple access performance. This space-time solution is similar to the architecture explained in Section 4.3.3 and involves finding weights for multiple pre-RAKE taps for each antenna element as well as for each user. Because the forward and reverse link are not reciprocal for a given frequency (the reverse link is asynchronous while the forward link is synchronous) the weights cannot be adaptively found during the reverse link and a direct matrix inversion method must be applied. This requires a great amount of hardware complexity. Alternatively, here we propose to implement a spatial precoding scheme synchronized with the greatest path arrival. To evaluate the performance, the system is applied to the spatial channel measured in Chapter 3. The performance for the different configurations (shown in Figure 3.9) will be compared and we will show the performance increase compared to a single antenna WLAN.

Because the measured channels have been proven to have individually different statistical models, a different performance can be obtained for different combinations. Given that we have measured MISO channels to U UTs, and that we want to select V UTs to which we are going to transmit, the MISO channel combination count (independently of order), $C_{channels}$ is:

$$C_{channels}(V,U) = \frac{V!}{U!(V-U)!}. \tag{5.2}$$

Because the system must be tested for each desired user channel individually, there are V possibilities for each channel combination, increasing the total amount of simulations to $C_{sims} = V \cdot C_{channels}$.

In order to reduce simulation time, only the combinations resulting in the best and worst performance shall be entirely evaluated. A preliminary simulation for C_{sims} is run at an average performance (choosing a lower SNR) from which the best and worst two combinations will be selected and run for all other necessary SNR values.

In Table 5.7, the channel combinations resulting in best and worst BER results are shown.

In Figure 5.14 we show the single user performance for different statistical models (explained in Table 3.1) as well as for the three measured configurations. We must note that the statistical channel models are represented using an exponentially decaying power profile and each path amplitude is modeled with a Rician distribution. The angle of arrival at each user is also defined but bears no influence on the single

Table 5.7: Multiuser Combinations Performance

		Config. 1 LOS	Config. 2 LOS	Config. 3 NLOS
4 users (Best combo)	Desired UT	4	1	4
	Interferers	1, 2, 3	2, 3, 4	1, 2, 3
4 users (Worst combo)	Desired UT	3	2	2
	Interferers	1, 2, 4	1, 3, 4	1, 3, 4
3 users (Best combo)	Desired UT	4	1	4
	Interferers	1, 2	2, 4	1, 2
3 users (Worst combo)	Desired UT	3	2	2
	Interferers	1,2	1, 3	1, 4
2 users (Best combo)	Desired UT	4	1	4
	Interferer	1	2	2
2 users (Worst combo)	Desired UT	3	2	3
	Interferer	4	1	4
1 user (Best)	Desired UT	4	1	4
1 user (Worst)	Desired UT	2	2	2

user performance. If in a first instance we compare the statistical models and see that the large office space with line-of-sight (S2-LOS) model obtains a better BER performance than the small office space with non-line-of-sight (S1-NLOS) because a) the deep fades are reduced in a LOS channel, and b) the greater delay spread characterizing S2-LOS allows it to benefit from greater temporal diversity compared to the S1-NLOS statistical model. Also if we observe the performance for the measured channels we see that the best performance belongs to the first configuration (C1) transmitting to UT-4. The MISO mean Rician K factor is greatest (K = 7 dB) explaining the better performance. In contrast the worst performance also belongs to C1 and in this case the mean MISO K factor (to UT-2) is lowest: K = -0.6 dB. Using the definition of the geometric mean, the mean bit error rate for all measured configurations at SNR = 7.4 dB is $\langle \text{BER} \rangle\, 4.2 \times 10^{-4}$. The worst case BER at this SNR is greater than the geometric mean by a factor of approximately 13.3, while the best case BER is approximately 21.4 times smaller than the geometric mean, showing a large variation in performance.

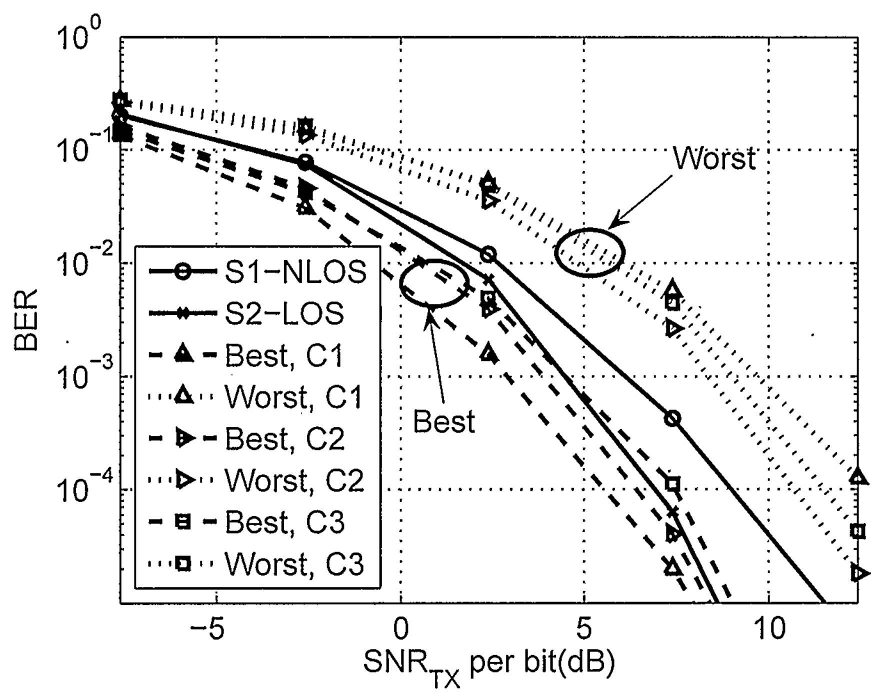

Figure 5.14: Multiple antenna performance for single user environment.

In Figure 5.15 we show the worst case multiuser performance at $SNR_{TX}/bit = 11$ dB while in Figure 5.16 we shown the best case performance at the same SNR. The worst case measured performance is compared with statistical models with colocated users (the users are spatially separated by 5 degrees), while the best case performance is compared with statistical models with separated users (the users are evenly separated over 180 degrees). The curves shown in Figure 5.15 indicate that worst case simulated results generated using channel measurements are worse than using the statistical channel model. In contrast, in Figure 5.16 we see that for the best case simulated results, the performance of the system using measured channels is of the same order as the typical office (S1) channel model. Nonetheless, the large office channel model always outperforms the system with a measured channel. It can be seen that as the user count increases the BER increases. This is because the SDMA MMSE algorithm is responsible not only of orthogonalizing users but also reducing the average noise at the receiver. As the user count increases the degree of freedom for diversity is reduced explaining the loss of performance seen. Another important point that can be extracted is that C1 presents the best measured performance for all user counts. This is easily explained because each user is separated into a different quadrant surrounding the access point and because the channel contains a LOS the access point can easily beamform to a given UT (particularly UT-4 as shown in Table 5.7).

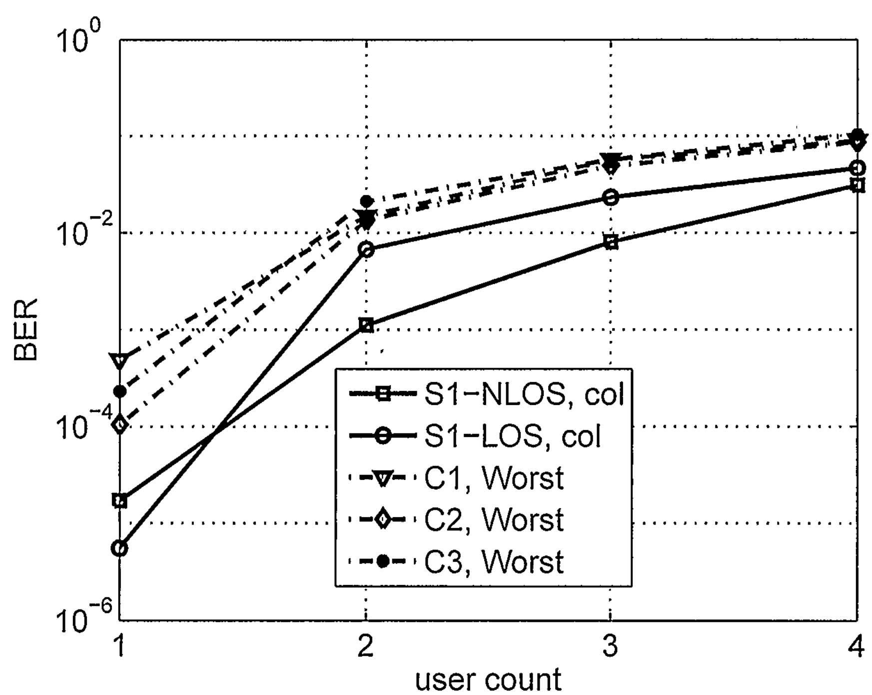

Figure 5.15: Multiple user worst performance (SNR = 11 dB).

Since the results in Figures 5.15 and 5.16 indicate that two user SDMA communication is feasible in a practical environment it is worthwhile to examine the scenario in more detail. Figure 5.17 shows the 2 user BER performance as a function of trans-

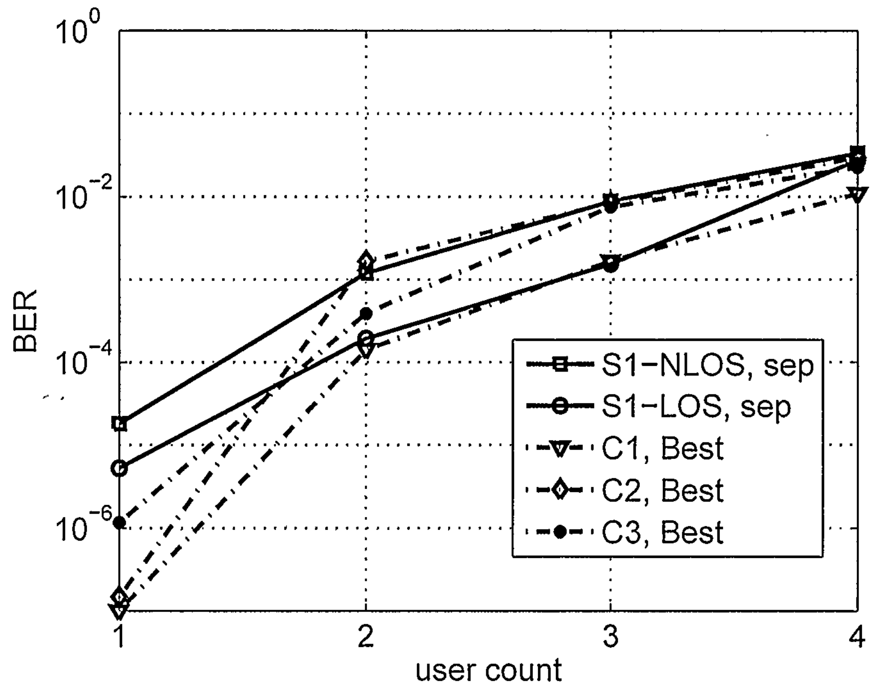

Figure 5.16: Multiple user best performance (SNR = 11 dB).

mit signal-to-noise ratio per bit in measured channels. The performance is shown for $M = 4$ antennas as well as for a single antenna. Evidently the single antenna performance is very bad and this follows multiple access theory (a minimum of 2 uncorrelated channels are necessary to separate two users). We can also see that as SNR increases the performance increases. The trend in the BER curves suggests that increasing SNR beyond the estimated 11 dB would provide further performance improvement. Finally, it can be seen that the best case scenario is for C1 where the desired user is UT-4 while the interferer is UT-1. Examining the configuration in Figure 3.9 we see that these users are at opposing quadrants and this can validate the performance. Additionally the correlation matrix between the eight channels of interest are shown in Table 5.8 and 5.9 for the best and worst scenarios respectively. The 8×8 cross-correlation matrix can be interpreted as a block diagonal matrix where the diagonal elements are the MISO correlation matrix. The off-diagonal elements represent the cross-correlation between MISOs. For example, in Table 5.8, the element at the first row, second column represents the spatial cross-correlation between channels $h_{TX-1,UT-4}$ and $h_{TX-2,UT-4}$ while the element at the first row and fifth column represents the spatial cross-correlation between $h_{TX-1,UT-4}$ and $h_{TX-1,UT-1}$. A MISO with low spatial cross-correlation properties will have a good potential for diversity gain. Alternatively, low off-diagonal cross-correlation values indicate a good potential for interference reduction: the channels between different users have low resemblance. Examining spatial correlation matrices in Tables 5.8 and 5.9 validates this statement: the off-diagonal cross-correlation values between UT-4 and UT-1 for C1 are much lower than the off-diagonal cross-correlation values between UT-3 and UT-4 for C3, indicating that spatial separation is less efficient in the latter case. To apply more weight to this conclusion, C1 is a LOS configuration and the antenna array to UT-4 is characterized with a particularly high Rician K-factor resulting in a very low fading probability, consequently aiding in the performance of the beamformer.

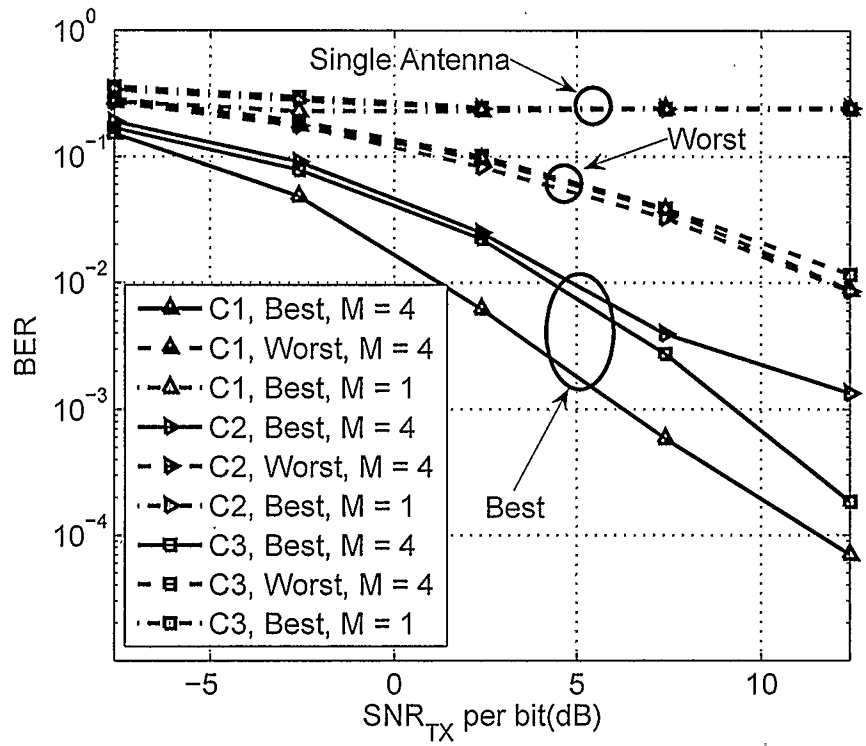

Figure 5.17: Performance for a two user environment.

Table 5.8: Correlation matrix between UT-4 and UT-1 (C1)

1.00	**0.27**	0.00	**0.38**	0.00	0.00	0.00	0.00
0.27	1.00	**0.17**	0.06	0.00	0.00	0.00	0.00
0.00	**0.17**	1.00	0.00	0.06	0.06	0.00	0.05
0.38	0.06	0.00	1.00	0.00	0.00	0.02	0.00
0.00	0.00	0.06	0.00	1.00	0.00	0.00	0.04
0.00	0.00	0.06	0.00	0.00	1.00	**0.30**	**0.10**
0.00	0.00	0.00	0.02	0.00	**0.30**	1.00	0.06
0.00	0.00	0.05	0.00	0.04	**0.10**	0.06	1.00

Table 5.9: Correlation matrix between UT-3 and UT-4 (C3)

1.00	**0.13**	0.08	**0.15**	0.04	0.07	0.09	**0.12**
0.13	1.00	**0.14**	0.09	0.07	**0.13**	**0.15**	**0.13**
0.08	**0.14**	1.00	0.01	0.00	0.01	0.01	**0.12**
0.15	0.09	0.01	1.00	0.08	0.04	0.09	0.08
0.04	0.07	0.00	0.08	1.00	**0.35**	0.03	**0.14**
0.07	**0.13**	0.01	0.04	**0.35**	1.00	**0.13**	**0.21**
0.09	**0.15**	0.01	0.09	0.03	**0.13**	1.00	**0.11**
0.12	**0.13**	**0.12**	0.08	**0.14**	**0.21**	**0.11**	1.00

Chapter 6

Conclusion

In this work we presented a spatial diversity solution to increase multiple access performance. Not only is it shown that a suboptimal space-time algorithm is feasible for the reverse link, the codes found during the reverse link can be reused in the forward link and we can expect the same quality of service in both directions assuming the asynchronous properties depicting the reverse link are accounted for. While we expect the user terminal physical layer baseband processor to fit on a single die using 0.18-μm CMOS technology, the AP functionality can be separated on different chips to reduce the power consumption requirement for each discrete component.

An important contribution of this thesis is the characterization of a spatial channel applied to multiple access scenarios. Actually, channel measurements are taken using a 4-element sectorized circular antenna matched to the RF front-end impedance at the frequency of interest, that is for a range of 20 MHz at a center frequency of 5.6 GHz. The set of observations representing the transmit antenna array with spatially separated users are concatenated to model a fading channel and for different configurations the channel properties are quantified and analyzed. We observe that the indoor channel amplitude must be modeled as Rician distributed: two extreme channel conditions (the first being line of sight (LOS) and the second non line-of-sight (NLOS)) are shown to obtain similar results. In fact, the mean Rician K factor for the LOS situation with separated users is $K = 3.38$ dB while for a NLOS scenario for which the users are situated in a different room it is $K = 2.16$ dB. Additionally, the typical office in which the measurements are taken is characterized with high dispersive properties: particularly in the colocated scenario where the distance with the scatterers is short relative to the traveling distance, the RMS delay spread is of the order of $\tau_{RMS} = 55$ nsec. The spatial correlation statistics is also computed and provides additional understanding in the further evaluation of spatial multiuser algorithms applied to indoor environments. As expected the correlation between the separated user terminals is low, but on the other hand the channel correlation is greater at the AP even with the presence of a metallic wall separating the antennas.

Spatial coding is also analyzed in detail including the reciprocity between the reverse link and forward link. In Section 2.3.3 we show the importance of maintaining an equal gain between a transmit RF front-end branch and its receiver front-end counterpart, and this for the AP as well as for each UT. Additionally it is shown in Section 4.1 that transmitting with a constant transmit power, the MMSE algorithm outperforms the zero-forcing solution. In contrast, it is possible to completely remove fading as seen at the receiver and the zero-forcing algorithm is shown to completely remove interference, but at the cost of an unreasonable increase in transmit power.

In Chapter 5 we apply the space-time theory and develop a multiuser system enhanced with antenna arrays. A grouping scheme is developed to spatially separate the users coded with a common CDMA signature. The complete physical layer transceiver system architecture is detailed and the communication performance is shown particularly for the forward link. In this project the AP implements a sub-optimal space-time coding scheme for dispersive channels, and each UT is expected to implement a CDMA receiver to account for channel multipath. Applied to a flat fading channel, the transceiver can account for a maximum of 32 users in the unique 20-MHz frequency allocation. As the channel dispersion increases the sub-optimality of the system requires a reduction in the amount of users present in the network and for typical office extreme conditions (above $\tau_{RMS} = 40$ nsec), the maximum user count must be limited to 8. In this case a multipath decorrelator structure can be implemented and, as its name implies, is responsible of removing multipath interference. The structure of the receiver is developed in detail and the detector expected power consumption is evaluated using 0.18-μm CMOS technology. While the RAKE receiver is shown to require 0.3 mW, the decorrelator power consumption is evaluated at 2.0 mW and poses no threat to the possibility of implementing the user terminal physical layer baseband processor on a single die.

Finally, in Section 5.2 we evaluate the possibility of adding spatial processing to a WLAN 802.11b access point with minimal changes to the standard. We evaluate the performance of the MMSE spatial algorithm during the forward link applied to the channel measurements taken in Section 3.3 and the results are compared with (high-thruput task group) HTTG statistical channel models. We observe the importance of modeling the spatial channel characteristics unaccounted for in single antenna systems, such as the angle of arrival and spatial correlation. In addition to these parameters obviously the spatial algorithm is affected by the (Rician) distribution of the amplitude for each tap, as well as the coherence bandwidth of each channel. The complete spatial model accounts for a highly varying bit error rate performance in the forward link and a more robust coding scheme should be devised to limit the variation in performance: a universal coding scheme applicable to different channel conditions is the current subject of active research. Nonetheless, the SDMA algorithm seems to provide enough degree of freedom to account for a doubling in multiuser capacity.

Bibliography

[1] Adel S. Sedra and K. C. Smith. *Microelectronic circuits.* Oxford University Press, 2004.

[2] Jan M. Rabaey. *Digital Integrated Circuits, A Design Perspective.* Prentice Hall Electronics and VLSI Series, Upper Saddle River, NJ, USA, 1996.

[3] Ning Zhang. Algorithm/architecture co-design for wireless communications systems. Phd. dissertation, University of California, 1998.

[4] A. P. Paplinski. Multipliers and their vhdl representation, http://www.csse.monash.edu.au/~ app/advdd/cse5312/lnts/ln07.pdf, 2003.

[5] Sunggu Lee. *Advanced Digital Logic Design: Using Vhdl, State Machines, and Synthesis for FPGAs.* Thomson, Toronto, 2006.

[6] *TSMC 0.18um Process 1.8 Volt SAGE-X Standard Cell Library Databook*, release 4.1 edition, 2003.

[7] T.S. Rappaport. *Wireless Communications, Principle and Practices.* Prentice Hall, New Jersey, 2002.

[8] M.C. Teuscher. Low power receiver design for portable RF applications. Ph.D. dissertation, University of California, 1998.

[9] J. Proakis. *Digital Communications.* Kluwer, Boston, 2000.

[10] H. P. Ma, M. L. Liou, and T. D. Chiueh. A 123-mW W-CDMA uplink baseband receiver IC with beamforming capability. *IEEE Journ. of Solid-State Circuits.*, volume 39:pp. 785–794, May 2004.

[11] S. Haykin. *Adaptive Filter Theory, 4th ed.* Prentice-Hall, Upper Saddle River, NJ, 2002.

[12] E. Kreyszig. *Advanced Engineering Mathematics, Seventh Edition.* John Wiley & Sons, New York, 1993.

[13] David Tse and Pramod Viswanath. *Fundamentals of Wireless Communication.* Cambridge University Press, Cambridge, UK, 2005.

[14] J.G Proakis and D. Manolakis. *Digital Signal Processing, Fourth Ed.* Prentice-Hall, Upper Saddle River, NJ, 1993.

[15] A. Intarapanich. Broadband MIMO wireless systems: Channel measurement and modeling. PhD. dissertation, University of Calgary, 2005.

[16] J. Rogers, C. Plett, and F. Dai. *Integrated Circuit Design For High Speed Frequency Synthesis.* Artech House, Norwood, MA, 2006.

[17] Robert H. Walden. Analog-to-digital converter survey and analysis. *IEEE Selected Areas In Communications*, Vol. 17:pp. 539–550, April 1999.

[18] Charles Ung. A space division multiple access transceiver. M.A.Sc. dissertation, University of Calgary, 2001.

[19] David M. Pozar. *Microwave Engineering, 2nd Ed.* John Wiley & Sons, USA, 1998.

[20] H. Samavati, H.R. Rategh, and T.H. Lee. A 5-GHz CMOS wireless LAN receiver front end. *IEEE J. Solid State Circuits*, 35:pp. 765 – 772, May 2000.

[21] T.-P. Liu and E. Westerwick. 5-GHz CMOS radio transceiver front-end chipset. *IEEE J. Solid State Circuits*, Vol. 35:pp. 1927–1933, December 2000.

[22] I. Vassiliou et al. A single-chip digitally calibrated 5.155.825-ghz 0.18-μm CMOS transceiver for 802.11a wireless LAN. *IEEE J. Solid State Circuits*, 38:pp. 2221–2231, December 2003.

[23] A.R.. Behzad et al. A 5-ghz direct conversion CMOS transceiver utilizing automatic frequency cotrol for the IEEE 802.11a wireless LAN standard. *IEEE J. Solid-State Circuits*, Vol. 38:pp. 2209–2220, December 2003.

[24] M. Zargari et al. A single-chip dual-band tri-mode CMOS transceiver for IEEE 802.11a/b/g wireless LAN. *IEEE J. Solid-State Circuits*, Vol. 39:pp. 2239–2249, December 2004.

[25] Perraud et al. A direct conversion CMSO transceiver for the 802.11a/b/g WLAN standard utilizing a cartesian feedback transmitter. *IEEE J. Solid-State Circuits*, volume 39:pp. 2226–2238, December 2004.

[26] Palaskas et al. A 5-GHz 108-mb/s 2x2 MIMO transceiver RFIC with fully integrated 20.5-dbm P1dB power amplifiers in 90-nm CMOS. *IEEE J. Solid-State Circuits*, Volume 41:pp. 2746–2756, December 2006.

[27] D.G. Rahn et al. A fully integrated multiband MIMO WLAN transceiver RFIC. *IEEE J. Solid-State Circuits*, Vol. 40:pp. 1629–1641, August 2005.

[28] Richard C. Johnson. *Antenna Engineering Handbook, Third Ed.* McGraw-Hill, New York, USA, 1993.

[29] Edwin Tung. A multiport antenna for an indoor pcs smart antenna system. M.sc. dissertation, University of Calgary, 1999.

[30] Warren L. Stutzman and Gary A. Thiele. *Antenna Theory And Design, Second Ed.* John Wiley & Sons, USA, 1998.

[31] A. Papoulis and S.U. Pillai. *Probability, Random Variables and Stochastic Processes, 4th ed.* McGraw Hill, Boston, 2002.

[32] V. Erceg et al. TGn channel model. Technical Report IEEE802.11-03/940r4, IEEE 802 Wireless World, www.802wirelessworld.com/index.jsp, May 2004.

[33] A.A.M. Saleh and R.A. Valenzuela. A statistical model for indoor multipath propagation. *IEEE J. Selected Areas in Communication*, Volume SAC-5:pp. 128–137, February 1987.

[34] A.J. Paulraj and C.P. Papadias. Space-time processing for wireless communications. *IEEE Signal Processing Magazine.*, volume 14:pp. 49–83, November 1997.

[35] J. Liberti. *Smart antennas for wireless communications : IS-95 and third generation CDMA applications.* Prentice Hall, 1999.

[36] J.E. Hudson. *Adaptive array principles.* Inspec, 1981.

[37] M. K. Simon and M. S. Alouini. *Digital Communication over Fading Channels.* John Wiley, 2004.

[38] G. Durgin. *Space-Time Wireless Channels.* Prentice Hall, 2002.

[39] A.Paulraj. *Introduction to space-time wireless communications.* Cambridge University Press, Cambridge, UK, 2002.

[40] J. Winters. Optimum combining in digital mobile radio with cochannel interference. *IEEE J. Select. Areas Commun.*, Vol. 2:pp. 528–539, July 1984.

[41] J. Litva and T. K.Y. Lo. *Digital Beamforming in Wireless Communications.* Artech House, Boston, USA, 1996.

[42] J.K Cavers. Single-user and multiuser adaptive maximal ratio transmission for rayleigh channels. In *IEEE Transactions on Vehicular Technology*, pages 2043–2050, November 2000.

[43] J. Choi and S. Perreau. MMSE multiuser downlink multiple antenna transmission for cdma systems. *IEEE Transactions on Signal Processing*, Vol. 52:pp. 1564 – 1573, June 2004.

[44] Huaiyu Dai. Wireless cellular communications with antenna arrays. Phd. dissertation, Princeton University, 2002.

[45] *IEEE Std 802.11: Wireless LAN Medium Access Control (MAC) and Physical Layer (PHY) Specifications.* http://standards.ieee.org/getieee802/, 1999.

[46] S. Verdu. *Multiuser detection.* Cambridge University Press, Cambridge, 1998.

[47] X. Wang and V. Poor. Space-time multiuser detection in multipah fading channels. *IEEE Transaction on Signal Processing*, Vol. 47:pp. 2356–2374, September 1999.

[48] Craig Teuscher. Software simulation of the infopad wireless downlink. M.A.Sc. dissertation, University of California at Berkeley, 1994.

[49] R. Lupas and S. Verdu. Near-far resistance of multi-user detectors in asynchronous channels. *IEEE Transactions in Communications*, Vol. 38:pp. 496–508, April 1990.

[50] R.E Ziemer, W.H. Tranter, and D.R. Fannin. *Signals and Systems: Continuous and Discrete.* MacMillan Publishing Company, New York, USA, third edition, 1993.

[51] S.S.H Wijayasuriya, G.H. Norton, and J.P. McGeehan. A sliding window decorrelating receiver for multiuser DS-CDMA mobile radio networks. *IEEE Transactions on Vehicular Technology*, Vol. 45:pp. 503–521, August 1996.

[52] G.E. Bottomley, T. Ottosson, and Y.P.E Wang. A generalized rake receiver for interference suppression. *IEEE Selected Areas In Communications*, Vol. 18:pp. 1536–1545, August 2000.

[53] P. Van Rooyen, M. Lotter, and D. Van Wyk. *Space-Time Processing for CDMA Mobile Communcations.* Kluwer, Boston, 2000.

[54] Seung-Jun Kim. Space-time synchronization and beamforming for wireless communication. Ph.D. dissertation, University of California at Berkeley, 2005.

[55] S.H. Jung, N.-M. Kim, and H.-J. Suh. Pre-RAKE assisted RAKE receiver for TDD WCDMA system. *Vehicular Technology Conference, 2003. VTC 2003-Spring. The 57th IEEE Semiannual*, Volume 2:pp. 1396 – 1400, April 2003.

[56] R. Esmailzadeh, E. Sourour, and M. Nakagawa. PreRAKE diversity combining in time-division duplex CDMA mobile communications. *IEEE Transactions on Vehicular Technology*, Volume 48:pp. 795 – 801, May 1999.

[57] J.F. Bousquet, Magierowski S., and R. Salmond. Development of the forward link physical layer in a multiuser sdma/cdma low-power transceiver. In *IEEE 2nd Int. Conference on Wireless Communications, Networking and Mobile Computing.*, 2006.